AERODYNAMIC CHARACTERIZATION OF MULTIPLE WING-WING INTERACTIONS FOR DISTRIBUTED LIFT APPLICATIONS

Thesis

Submitted to

The School of Engineering of the

UNIVERSITY OF DAYTON

In Partial Fulfillment of the Requirements for

The Degree of

Master of Science in Aerospace Engineering

By

Nevin Jestus

Dayton, Ohio

August 2023

AERODYNAMIC CHARACTERIZATION OF MULTIPLE WING-WING INTERACTIONS

FOR DISTRIBUTED LIFT APPLICATIONS

Name: Jestus, Nevin

APPROVED BY:

Sidaard Gunasekaran, Ph.D.
Advisory Committee Chairman
Assistant Professor
Mechanical and Aerospace Engineering

Markus Rumpfkeil, Ph.D.
Committee Member
Professor
Mechanical and Aerospace Engineering

Aaron Altman, Ph.D.
Committee Member
Tech Advisor
Aerospace Vehicles Directorate, Air Force Research Laboratory

Michael Mongin
Committee Member
Aerospace Research Engineer
Aerospace Vehicles Directorate, Air Force Research Laboratory

ABSTRACT

AERODYNAMIC CHARACTERIZATION OF MULTIPLE WING-WING INTERACTIONS FOR DISTRIBUTED LIFT APPLICATIONS

Name: Jestus, Nevin
University of Dayton

Advisor: Dr. Sidaard Gunasekaran

There has been a recent surge in the need for unmanned aerial vehicles (UAVs), drones, and air taxis for a variety of commercial, entertainment, and military applications. New aircraft designs put forth by companies have shown to feature multiple lift producing surfaces and rotors acting in proximity to each other. These configuration choices are primarily informed by the "compactness" requirement in the design. For this reason, configurational choices are being considered that would otherwise not receive attention. Multi-wing configurations or distributed lift systems become a compelling choice in conceptual design of future UAVs and private air vehicles (PAVs) that complements the vertical takeoff and landing capabilities of the design.

For multi-wing configurations to be considered in the early conceptual design process, the reliability of traditional lower order aerodynamic methods in predicting these aerodynamic effects must be determined. However, the nature of a highly distributed lift configuration, with 10 or more lifting surfaces in close proximity, does not lend itself to rapid or accurate viscous numerical solution. Moreover, highly distributed lift configurations drive individual lifting surface Reynolds numbers into a range where viscous interactions could have a profound effect on aerodynamic performance. As such, the degree of dependence of wing-wing interactions due to viscous effects could be determined in a first iteration through a reductionist approach. Focusing specifically on the three-dimensional viscous interactions and the aerodynamic forces on the upstream and downstream wings allows for a direct determination of the importance and isolated contribution of these effects.

Proximity effects due to wing-wing interactions were experimentally quantified as a function of gap and stagger across a wide range of different relative angles of attack (décalage). The proximity effects and the zone of influence at different gap and stagger locations were systematically characterized through measurement of the changes in aerodynamic force coefficients of individual wings and the combined wing-wing system. The wing angle of attack combinations that maintain similar aerodynamic efficiency at different gap and stagger locations were determined to allow for optimal placement of wings in a distributed lift system. All experiments were conducted at the University of Dayton Low Speed Wind Tunnel (UD-LSWT) on two, three, and four Clark-Y AR 2 semi-span wings. Numerical investigations were conducted to validate FlightStream, a potential flow solver, with experimental results to use as a tool to extract more information about the flow physics and to simulate further configurations without the need of conducting wind tunnel tests. All the analysis techniques were done on the two, three, and four-wing studies to determine a wide range of beneficial and detrimental combinations of gap, stagger, and décalage along with an overall conclusion about the effect of the number of wings on these configurations.

The publications and presentations involved in the author's thesis work are listed below:

Publications:

[1] Jestus, Nevin, Sidaard Gunasekaran, Michael Mongin and Aaron Altman, "Aerodynamic Characterization of Wing-Wing Interactions for Distributed Lift Application," in *AIAA SciTech Forum*, National Harbor, MD, 2023.

[2] Jestus, Nevin and Sidaard Gunasekaran, "Aerodynamic Interactions among Three Identical Wings in Close Proximity," in *AIAA 2023 Region III Student Conference*, Dayton, OH, 2023.

Presentations:

[1] "Wing-Wing Interactions for Distributed Lift Applications," in *Dayton-Cincinnati Aerospace Sciences Symposium*, Dayton, OH, 8 March 2022.

[2] "Aerodynamic Characterization of Wing-Wing Interactions for Distributed Lift Application," in *AIAA SciTech Forum*, National Harbor, MD, 23 January 2023.

[3] "Aerodynamic Interactions among Three Identical Wings in Close Proximity," in *Dayton-Cincinnati Aerospace Sciences Symposium*, Dayton, OH, 28 February 2023.

[4] "Aerodynamic Interactions among Three Identical Wings in Close Proximity," in *AIAA 2023 Region III Student Conference*, Dayton, OH, 25 March 2023.

Dedicated to my family, friends, and fellow aerospace engineers/researchers.

ACKNOWLEDGEMENTS

I would like to first thank my amazing family for all their love and support during my academic career. To my parents, Jestus and Swapna, for understanding when I would stay in Dayton rather than go home for holidays. To my siblings, Nikitha and Niril, for always providing me with entertainment and laughs. Thank you to my grandparents, cousins, and all my friends who were a huge support system, keeping me motivated and focused on my goals.

Thank you to my fellow University of Dayton Low-Speed Aerodynamics Research Group members, especially Jielong (Jacky) Cai, Ian Tierney, Andrew Killian, and Luke Duncan, for constantly providing valuable feedback and suggestions during our research meetings, while making sure we all have fun even under stress. I appreciate all the long hours Jacky would spend as the Wind Tunnel Technician, helping me with my experimental setups in the wind tunnel.

None of this work would have been possible without the assistance of my advisors. Dr. Sid Gunasekaran gave me a chance when I first started at UD and continued to be patient with me as I began my aerodynamics path, pushing me to be better as an engineer and researcher. His teaching showed me that I should not only be focused on the results, but constantly be asking why, how, and what so that I get a deeper understanding allowing me to be better equipped for any future problems. Michael Mongin helped transition me into my research and allowed me to watch and learn from him. Thank you, Mike, for all your professional tips from having a lab notebook to even what to name my files. I hope to one day acquire the knowledge and expertise of Dr. Aaron Altman. Thank you for giving me this great opportunity collaborating with the U.S. Air Force Research Laboratory (AFRL) and always making sure my work was up to high standards. Lastly, Dr. Markus Rumpfkeil for being a mentor to me and helping me grow as an engineer. He was the first person I met at the University of Dayton before I committed to graduate school and showed me that this was the right place for me.

TABLE OF CONTENTS

LIST OF FIGURES

LIST OF TABLES

LIST OF ABBREVIATIONS AND NOTATIONS

Abbreviations:

AFC	Active Flow Control
AR	Aspect Ratio
Exp	Experiments
FS	FlightStream
ISE	Ideal System Efficiency
LE	Leading Edge
LLT	Lifting Line Theory
MAV	Micro-Air Vehicle
PAV	Private Air Vehicle
PIV	Particle Image Velocimetry
PLA	Polylactic Acid
Re	Reynolds Number
Std Dev	Standard Deviation
TE	Trailing Edge
UAV	Unmanned Aerial Vehicle
UD-LSWT	University of Dayton Low-Speed Wind Tunnel
VLM	Vortex Lattice Method
VSTOL	Vertical/Short Take-Off and Landing

Nomenclature:

α	Angle of Attack
α_i	Induced Angle of Attack
$\alpha_{L=0}$	Zero Lift Angle of Attack
b	Span
c	Chord
C_{D_i}	Induced Drag Coefficient
C_L	Lift Coefficient
C_{L_α}	Lift Curve Slope
C_P	Coefficient of Pressure
Δ	Difference
ε_d	Downwash Angle
G	Gap
L/D	Lift-to-Drag Ratio
S	Wing Area
St	Stagger
U_∞	Freestream Velocity
δ	Décalage

CHAPTER 1

INTRODUCTION AND BACKGROUND

Multi-planes, or aircraft with multiple wings, are not a new concept. These designs often employ smaller, light-weight wings to increase maneuverability. Over time, companies have unveiled designs that feature multiple lift-producing surfaces and rotors working in close proximity to one another. Among these companies, Zerbe, Faradair, and SE Aeronautics have developed fixed wing concepts, as shown in Figure 1-1. The Zerbe Air Sedan [1], built by Jerome S. Zerbe in the 1920s, features four wings with equal stagger and gap between them. The Faradair BEHA [2] is a new hybrid-electric aircraft with a triple box wing design, intended to carry approximately 18 passengers. SE Aeronautics [3] aims to revolutionize the airliner industry with its SE200 design, which is touted as a more efficient aircraft with faster manufacturing time, owing to its unique approach of employing three thin wings.

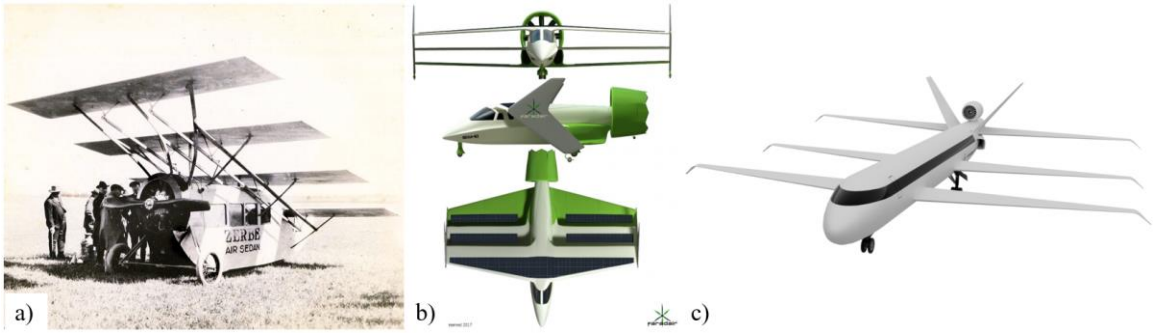

Figure 1-1 Fixed Wing Multi-Planes of the a) Zerbe Air Sedan [1], b) Faradair BEHA [2], and c) SE Aeronautics SE200 [3]

Even designs with multiple rotors often require lifting surfaces in close proximity for structural support. Designs such as the Honda eVTOL [4], Ascendance ATEA [5], and Volocopter VoloConnect [6] shown in Figure 1-2, illustrates how the use of multiple lifting surfaces has become a recurring theme in unmanned aerial vehicles (UAVs) and private air vehicles (PAVs), As such, exploiting wing-wing interactions could have significant impact on increasing efficiency.

Figure 1-2 Multiple rotor and lifting surface designs of a) Honda eVTOL [4], b) Ascendance ATEA [5], and c) Volocopter VoloConnect [6]

Looking back, some of the earliest aircraft were biplanes which featured two wings stacked vertically. Additionally, aircraft can be seen with two wings arranged horizontally in relation to each other, known as canard or tandem wing configurations. The first successful powered flight is credited to the Wright Flyer [7] in 1903, which not only featured a biplane configuration but also featured a canard. Before diving into the concept of distributed lift and its applications, it is imperative to understand these two fundamental wing configurations.

Understanding the wing-wing interactions between lifting surfaces expands beyond just biplanes, tandems, and distributed lift aircraft designs. Numerous other applications exist from different multi-plane concepts to multi-element airfoils, wind turbines, compressor blades, and many more that will be discussed in this chapter.

1.1 Biplane Aerodynamics

As mentioned previously, biplanes are generally classified as aircraft with two wings aligned vertically relative to each other. Dimensional nomenclature is defined in Figure 1-3, which depicts a cross-section of a biplane perpendicular to the span. The vertical spacing is referred to as the gap (G) and the horizontal spacing is known as the stagger (St), both of which are typically measured relative to the quarter-chord of the airfoil/wing. The décalage angle (δ) is the angle between the two chord lines.

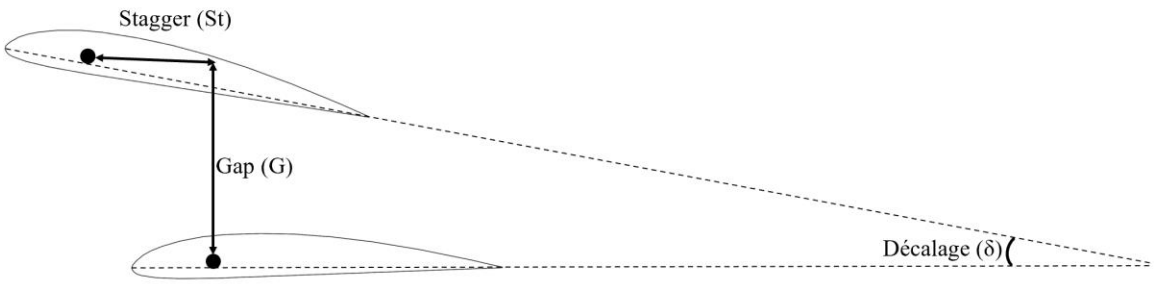

Figure 1-3 Biplane nomenclature of stagger, gap, and décalage

While biplanes are not as common as they once were, they offer several advantages over a monoplane. A structural, aerodynamics, and performance comparison between biplanes and monoplanes was presented by Chatfield [8] in 1928. From a structural standpoint, biplanes require lighter bracing due to their smaller size and lower bending moments. In terms of aerodynamics, Chatfield notes that a monoplane has better aerodynamic characteristics due to reduced parasite drag, absence of interplane-bracing, and lack of negative interference between wings. The major advantage of biplanes lies in their maneuverability, as a result of small span wings and thin airfoils. This could be why many modern aerobatic aircraft are modified biplanes.

Quantifying the interactions of lifting bodies was attempted by Thwaites [9], who described the aerodynamics of two-dimensional biplanes and infinite arrays of lifting airfoils. Notable early contributions using the exact method of conformal transformation are attributed to Garrick [10]. While Söhngen inversion integrals offer an analytical way to determine the pressure distribution of a single-element airfoil in flow, the method becomes increasingly challenging to for airfoils operating at numerous operating points with significant geometric and aerodynamic constraints and multiple degrees of freedom. As such, the quantification of interactions among lifting surfaces has predominantly been conducted using experimental and computational methods.

In 1929, Munk [11] published General Biplane Theory, providing fundamental knowledge about biplanes with stagger and decalage, supported by theoretical and experimental data. A formula was derived to determine the additional lift coefficient of biplanes (ΔC_L), as expressed in

Equation (1), where S is the total area, b is the span, k is the equivalent monoplane span factor, and R is a distance used for calculating the induced downwash. The term $\left(\frac{1}{k^2} - 0.5\right)$ is known as the Munk factor, which is a function of the gap to span ratio. According to Munk, as the gap increases, Munk's factor decreases, leading to a decrease in C_L. Munk also provides an equation for the induced drag coefficient (C_{D_i}) in Equation (2), where k is 1.0 for a monoplane and gets increases slightly as more gap is introduced.

$$\Delta C_L = \pm 2 C_L \frac{S}{b^2}\left(\frac{1}{k^2} - 0.5\right)\frac{b}{R}\frac{st}{b} \quad \textbf{(1)}$$

$$C_{D_i} = \frac{C_L^2}{\pi}\frac{S}{b^2 k^2} \quad \textbf{(2)}$$

Prandtl [12] also developed an approximation for the total induced drag on biplanes and triplanes. Prandtl used an influence coefficient, σ, as a function of gap (G) and span (b) in Equation (3) to calculate the induced drag of a triplane. Here, σ_1 represents the mutual influence on the top or bottom wing with the middle wing, σ_2 is the influence on the top and bottom wing, and x is the coefficient of distribution of wing loads. The variables σ and x are mathematically expressed in Equation (4) and Equation (5) respectively. The theory assumes equal span and gap spacing between the three wings and that the upper and lower wing generate the same amount of lift at the minimum drag condition.

$$D = \frac{L^2}{2\pi q b^2}[1 + \sigma_2 - 2x(1 + \sigma_2 - 2\sigma_1) + x^2(3 + \sigma_2 - 4\sigma_1)] \quad \textbf{(3)}$$

$$\sigma = f(G, b) \quad \textbf{(4)}$$

$$x = \frac{L_2}{(L_1 + L_2 + L_3)} \quad \textbf{(5)}$$

Biplanes were revisited through experimental investigations by Kang et al. [13, 14] on the effects of gap and stagger on biplanes with endplates. In a biplane configuration, the gap and stagger had a significant influence on performance, with the upper wing producing more lift in all cases. Additionally, it was found that the configuration was capable of increasing the efficiency of the

lower wing through the effects of downwash. Using Particle Image Velocimetry (PIV), it was observed that decreasing the gap between the two wings resulted in a smaller downwash angle off the trailing edge, which in turn resulted in lower lift. PIV also disproved the hypothesis of a jet of increased velocity being created between the two wings due to a reduction in area both geometrically and aerodynamically with larger downwash angles produced by the upper wing as seen in Figure 1-4.

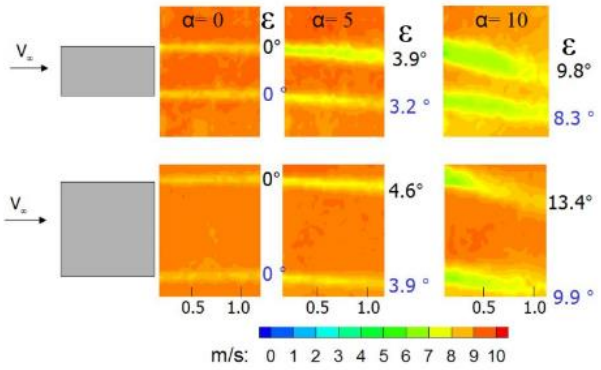

Figure 1-4 Streamwise PIV velocity contour to observe effects of changing gap [13]

The study observed that beyond a 1-chord gap and stagger, the benefits of further wing-wing separation rapidly diminished. Figure 1-5 visually supports this statement, as minimal difference in lift coefficient is recorded beyond the 1c St point on the x-axis and the 1c G line at a 5° angle of attack, which is around the maximum lift to drag ratio angle.

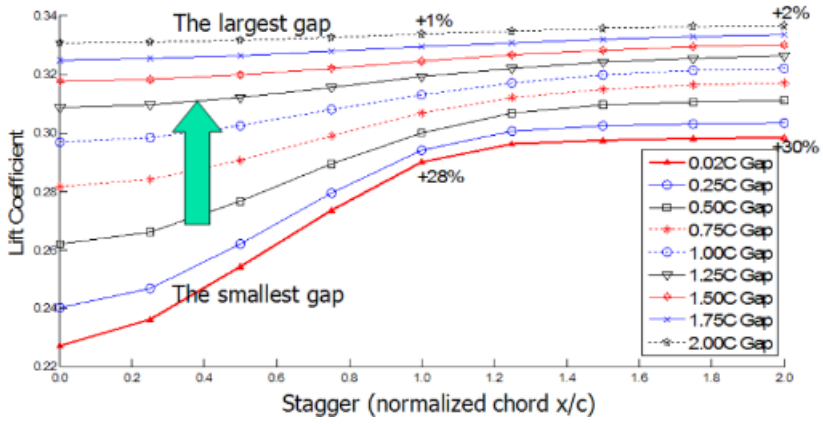

Figure 1-5 Effect of Stagger and Gap on lift coefficient of biplane with endplates at 5° angle of attack [13]

Furthermore, using the experimental data collected, Kang et al. [15] empirically derived Equation (6) to predict lift of biplanes with endplates lift as a function of stagger, gap, angle of attack in degrees, and Aspect Ratio (AR). The equation was developed through linear regression analysis and validated with experimental data from various configurations tested at different facilities. This new method better accounts for the differences in lift-curve slope that arise from the direction of stagger.

$$C_L = [(-0.0072 * St + 0.0145) * G + (0.018 * St + 0.0499)] * \alpha * \left(0.75 + \frac{1.5}{AR}\right) \quad \textbf{(6)}$$

1.2 Tandem Aerodynamics

On the opposite end of the spectrum in wing placement is the tandem wing design, where the wings are aligned horizontally. While canards are also arranged similarly, the key distinction between classifying an aircraft as a tandem or canard lies in the wing area. In a tandem configuration, the two wings must have approximately the same wing area, whereas a canard has a significantly smaller front wing. Figure 1-6 shows a visual example of the difference between the Scaled Composites Proteus [16], a tandem wing testbed aircraft designed for high altitude and long endurance, and the Piaggio P.180 Avanti EVO [17], an Italian canard general aviation aircraft.

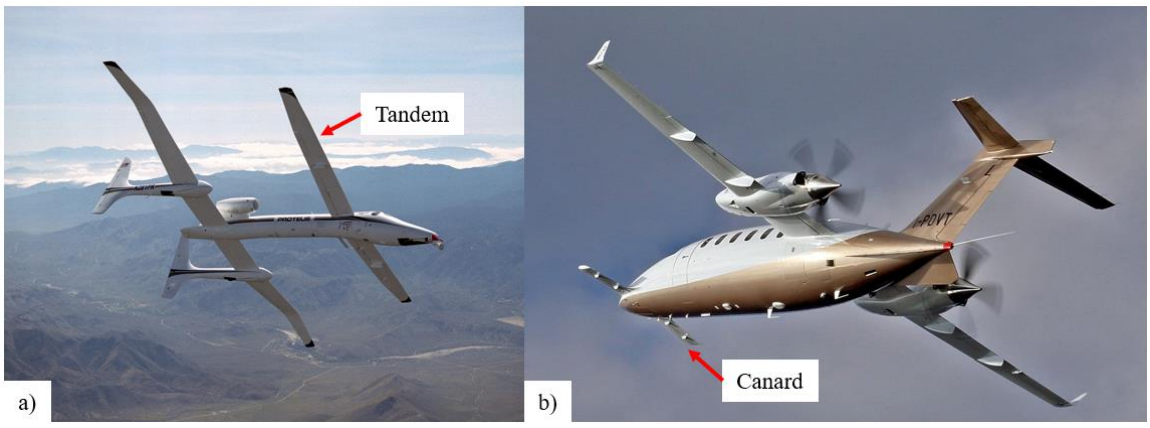

Figure 1-6 Difference between tandem and canard configurations of the a) Scaled Composites Proteus [16] and b) Piaggio P.180 Avanti EVO [17]

Minardo [18] provides an overview of the history of tandem configuration aircraft and enumerates the perceived advantages and drawbacks of tandem designs in general. The advantages of tandem wings include a reduction in wingspan, enhanced maneuverability, increased stability, and often the elimination of the need for a tail, thereby reducing parasitic drag. The disadvantages stem from the unconventional nature of the design, accompanied by challenges in achieving longitudinal stability and a lower maximum lift coefficient.

Kryvokhatko [19] authored a book on the aerodynamics of tandem wing aircraft, in which highlighted were the three major aerodynamic features to be considered in tandem aircraft: flow deceleration, flow turbulence, and downwash/upwash. Flow deceleration and turbulence can cause lower lift and higher drag on the rear wings when they are placed in the aerodynamic trace of the front wing due to lower flow speed and turbulent boundary layer development. Furthermore, pitch oscillations from lift changes would result in poor longitudinal stability. Tip vortices are primarily responsible for downwash/upwash and cause different induced angle of attack on the rear wing when interacting with the shedding from the front wing. These three aspects are primarily responsible for the performance decrements of any downstream wing, but could be mitigated with strategic placement of these horizontally arranged wings.

The upwash and downwash generated by tandem wing configurations was studied by Glauert [20]. The interaction between the two wings was mostly in the form of downwash effects on the rear wing from circulation caused by the front wing's lift generation. In subsonic flows, a much smaller upwash effect from the rear wing back onto the front wing is also evident. The findings suggested that the two wings should not be of equal size, and that the rear wing should be placed at a reduced incidence angle to generate less lift, thereby benefiting static stability. Some predictions and calculations of downwash effects were published, but the general theory was addressed more in latter work.

Scharpf and Mueller [21] quantified the 2-D effects on tandem Wortmann FX63-137 cambered airfoils, focusing on the separation bubble and pressure distribution, to understand the

performance of tandem wings in the absence of 3D wingtip vortices. While the rear wing suffered in the presence of the front wing, experiments showed that changes in décalage could result in improvements up to 77% in total efficiency compared to a single airfoil. All positive décalage led to an increase in aerodynamic efficiency. The downwash from the front wing showed potential to maintain attached flow and delay stall on the rear wing.

Jones et a. [22] investigated biplane and tandem configurations at low Reynolds numbers for micro-air vehicle (MAVs) applications. It was observed that while there were no significant improvements in performance, stall was delayed in many of the configurations. PIV results showed the dependency of the overall performance on separated shear layer interactions from the leading and trailing wings, as well as the presence of highly unsteady flow and fluctuations from their wakes.

While Prandtl and Munk made significant contributions to multi-plane aerodynamics, their theories did not account specifically for the effect of wing stagger. Although their theories were experimentally verified for moderate stagger, true tandem configurations have a substantial stagger component compared to the gap component, creating a knowledge gap in multi-plane theory. Wolkovitch [23] attempted to compare the theory with the experimental data on the performance of tandem wings for subsonic vertical/short take-off and landing (V/STOL) aircraft and found that the Prandtl-Munk theory overestimated the induced drag around the maximum L/D regime. The study also observed that interference effects on parasite drag were small, a reasonable elevon deflection range was needed to trim, and in stall conditions, the tandem exhibited a pitch-down tendency with relatively minimal buffeting. Lastly, there were no significant issues with directional stability.

1.3 Multi-Element Systems

Multi-element airfoils are another application where interactions between airfoils are essential for high performance. Modern wings on large aircraft commonly feature leading-edge (LE) devices, such as slats, and trailing-edge (TE) devices like flaps. These devices, exemplified

in Figure 1-7 [24], often work by increasing the overall wing area when deployed. They enhance lift during takeoff and landing, thereby decreasing the takeoff and landing distances. These high-lift devices can be treated as smaller airfoils in close proximity to the main lift-generating airfoil, and therefore provide valuable information for this study.

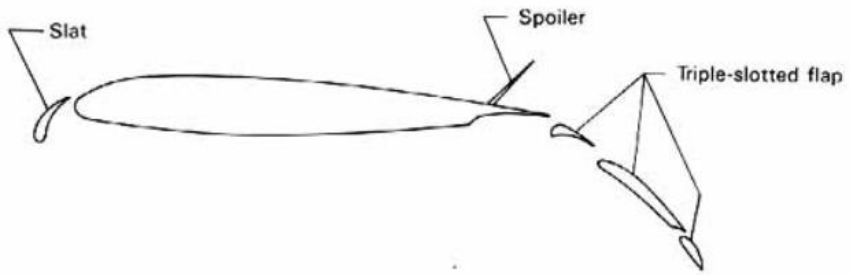

Figure 1-7 High lift system example of airfoil with triple-slotted flap, slat, and spoiler [24]

Van Dam [25] discusses the aerodynamic design process for multi-element systems, focusing on large transport aircraft. He provides an overview of the history of multi-element high-light systems development and identifies issues that need to be addressed for a more efficient design process. He also mentions the need for improved turbulence modeling tailored to the separated unsteady flows and wakes within these systems, as well as more work with separation/transition bubbles.

Smith [26] in a study of multi-element airfoil aerodynamics states five primary effects created by the presence of gaps: slat effect, circulation effect, dumping effect, off-the-surface pressure recovery, and the fresh-boundary-layer effect. The slat effect occurs when the circulation velocities from a forward element run counter to the velocities on the downstream element, creating reduced pressure peaks on the downstream element. The circulation effect refers to the presence of greater circulation and higher velocity on the forward element caused by the downstream element. The dumping effect involves delayed separation and increased lift attributed to higher discharge velocities relieving the pressure rise in the boundary layer. Off-the-surface pressure recovery denotes more efficient pressure recovery caused by the deceleration of the wake with the high-

velocity boundary layer, as compared to deceleration caused by contact with a wall. Finally, the fresh-boundary-layer effect describes how each element starts with a fresh, thin boundary layer, which is better suited to withstand stronger adverse pressure gradients.

Drela [27] developed a multi-point optimization method (MSES) for multi-element airfoils to be used for transonic cruise and landing. The code used streamline-based discretization of the Euler equations to compute the inviscid flow and multi-equation integral formulation for the shear layers. A Newton method is utilized to solve the coupled system of equations involving displacement thickness and edge velocity.

Understanding interactions between airfoils is also important in applications beyond aviation. Wind Turbines, for instance, are a crucial component in the quest for renewable energy to sustain the modern world. These turbines typically consist of three or more blades configured in either a horizontal-axis or vertical-axis arrangement. Ragheb and Selig [28] adopted the optimization technique developed by Drela [27] and applied it to multi-element designs for wind turbine applications, aiming to reduce thick airfoils on blade roots. Computational investigations were performed on seven configurations with different combinations of flaps, slats, and struts. These multi-element geometries resulted in significant increases in lift-to-drag (L/D) ratios of up to 82% and a gradual decrease beyond maximum L/D.

In motorsports, contemporary Formula 1 cars employ complex multi-element front wings to optimize air flow and downforce, for a competitive edge. These multi-element wings operate within similar inter-wing spacing as the multi-element airfoils mentioned above. A computational study was conducted on different airfoils, angles, and spacings by Liu and Chen [29]. The addition of a second wing showed a delay in stall angle, effectively reducing vortices and subsequently generating greater downforce with lower drag. With regard to the distance between the primary wing and the smaller secondary aft wing, downforce was observed to increase with vertical distance, but showed insensitivity to changes in horizontal distance. Configurations involving three

and four wings were examined, revealing no significant deviation in the downforce generated, although the three-wing configuration avoided the higher turbulence seen with four wings.

1.4 Downwash Effects

A common phenomenon experienced by lifting surfaces, which is amplified in the cases of multi-element configurations like biplanes and tandems, is downwash. As described by the National Aeronautics and Space Administration (NASA), the mixing of a wing's low pressure and high-pressure regions at the wingtips create vortices that result in downwash [30]. The downwash changes the freestream velocity direction, thereby tilting the lift vector resulting in an overall decreased lift when compared to the airfoil counterpart. Downwash effects are often attributed with deviations in performances of biplanes and tandems compared to a conventional monoplane. Therefore, understanding it is of upmost importance, whether to mitigate its effect or to harness it as a benefit.

Downwash began to appear in aerodynamics theory after the flow around finite wings was understood. The fundamentally derived equation for calculating downwash for a rectangular planform wing is Equation (7), where the downwash angle (ε_d) in radians is a function of the lift coefficient (C_L) and aspect ratio (AR) of the wing. Prandtl's Lifting Line Theory (LLT) provides insight into how downwash varies in both the spanwise and vertical directions due to the presence of non-uniform lift distribution and tip vortices.

$$\varepsilon_d = \frac{2C_L}{\pi AR} \quad \textbf{(7)}$$

A prediction method of average downwash gradient in canard configurations was studied by Levy [31]. Vortex Lattice Method (VLM) was used to determine correction factors for the nonlinear variation of the downwash gradient generated by a canard onto the main aft wing. The correction factor due to spanwise variation (k_b) is a function of AR, taper ratio (λ), sweep angle (Λ), downwash gradient ($z/(b/2)$), and span ratio. The lift coefficient of a wing and canard ($C_{L_{\alpha_{wc}}}$) is determined with Equation (8) and the correction factor is applied through the average downwash

at the plane of symmetry as seen with Equation (9). Using the correction factor achieves reasonable accuracy under the assumptions of incompressible flow, application within given range of planform parameters and geometric combinations, and that the canard wake does not directly impinge on the main wing.

$$C_{L_{\alpha_{wc}}} = C_{L_{\alpha_w}}\left(1 - \frac{d\varepsilon_w}{d\alpha}\right) + C_{L_{\alpha_c}}\frac{S_c}{S_w}\left(1 - \frac{d\varepsilon_c}{d\alpha}\right) \quad \textbf{(8)}$$

$$\frac{d\varepsilon_w}{d\alpha} = k_b \frac{d\varepsilon_w}{d\alpha}|_{y=0} \quad \textbf{(9)}$$

While horizontal stabilizers are not considered critical lift-generating components on an aircraft, wing-tail interactions share many similarities with wing-wing interactions in tandem wings. The angle of the downwash from the main wing can significantly affect the effectiveness of a horizontal tail in maintaining robust aircraft stability. Philips et al. [32] present a closed-form analytic solution for predicting the downwash generation by the main wing on an aircraft's tail and compares reasonably with an empirical simulation by Hoak [33], an analytic method by McCormick [34], and experimental wind tunnel data. Equation (10) calculates the downwash angle as a function of the wing's lift coefficient (C_{L_w}), aspect ratio (R_{A_w}), and several factors that can be found either analytically or graphically. These factors include the wingtip vortex span factor (K_b), tail position factor (K_p), wing sweep factor (K_s), and wingtip vortex strength factor (K_v). When using the solution of the downwash angle across different spatial coordinates, all methods show a bell-shaped curve when varying in the y-axis (lift axis) from below the wing's TE to above the TE with the strongest in line with the TE. Figure 1-8 shows the downwash distribution at a normalized downstream location from the wing of 0.5 and 1.0. The prediction equation, labeled "Equation (25)", demonstrated a strong correlation along the x-axis (drag axis) particularly close to the TE, where the McCormick method faced challenges.

$$\varepsilon_d = \frac{K_v K_p K_s}{K_b}\frac{C_{L_w}}{R_{A_w}} \quad \textbf{(10)}$$

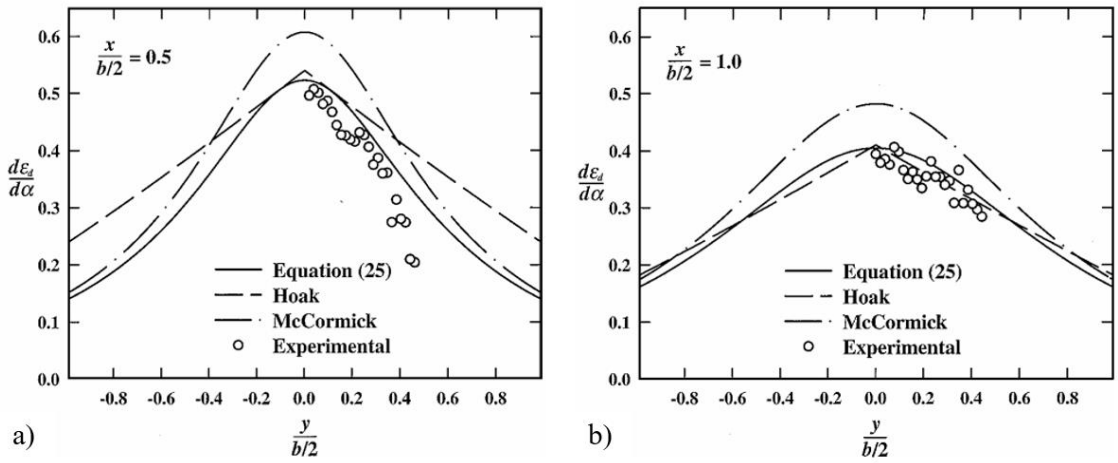

Figure 1-8 Comparison of different downwash prediction methods at different normalized downstream distances of a) 0.5 and b) 1.0 [32]

1.5 Previous Distributed Lift Research

The primary application that was used to motivate this thesis was distributed lift. The aircraft design concept of distributed lift aims to divide the total wing area of a conventional large-span monowing into multiple small-span wings. The initial inspiration was to help mitigate airport congestion caused by aircraft with large wingspans. Other anticipated benefits of this new design, featuring multiple small wings, include:

- Lighter weight and compactness
- Easier manufacturing, transportation, and installation
- Simpler maintenance
- Increased maneuverability with smaller rolling moment from shorter wings
- Higher survivability/damage tolerance due to the presence of multiple wings across the fuselage to share lift

Research on this concept has been conducted at the University of Dayton since around 2015 under several researchers. Memon et al. [35] first presented experimental work on the concept by creating a cylindrical fuselage with 200 “mini-wings” and compared it to a large monowing equivalent, having the same total area as all the “mini-wings” combined. Experimental testing of

this novel design revealed that the multi-wing configuration achieved approximately 45% of the lift of the monowing.

The research continued with Truszkowski et al. [36, 37] testing different multi-wing configurations, that featured significantly fewer wings to be more practical, and examined various spacings between them. Mongin et al. [38] built upon this work by testing various multi-wing configurations through wind tunnel testing with a force balance and numerical investigations using Vortex Lattice Method codes. The wings were positioned at fixed spacings and equal geometric angles of incidence; thus, experiments were conducted without adjusting the angles between wings (décalage). The results from this study showed that the multi-wing configurations could achieve around 50% of the aerodynamic efficiency of the monowing, even reaching up to 61% in the case of the 6 Wing (3c Gap, 5c Stagger). Comparing the experiments to the VSPAERO potential flow code showed similar trends, but absolute values differed. The authors hypothesized that this discrepancy be due to the lack of modeling of the laminar separation bubble behavior and the method of wake resolution in the vortex method.

Recent testing on multi-wing configurations attached to the fuselage of a military cargo transport was conducted by Mongin et al. [39]. Semispan tests were conducted at the University of Dayton Low-Speed Wind Tunnel (UD-LSWT) and full-span tests were conducted at the U.S. Air Force Research Laboratory Vertical Wind Tunnel (AFRL-VT). Four different wing sets were tested across various angles of attack, sideslip angles (β), and Reynolds numbers (Re), as shown in Figure 1-9. The specifications of those configurations are listed in Table 1-1. In each set, the total area of the combined wings was roughly equivalent to the monowing configuration to follow the distributed lift concept.

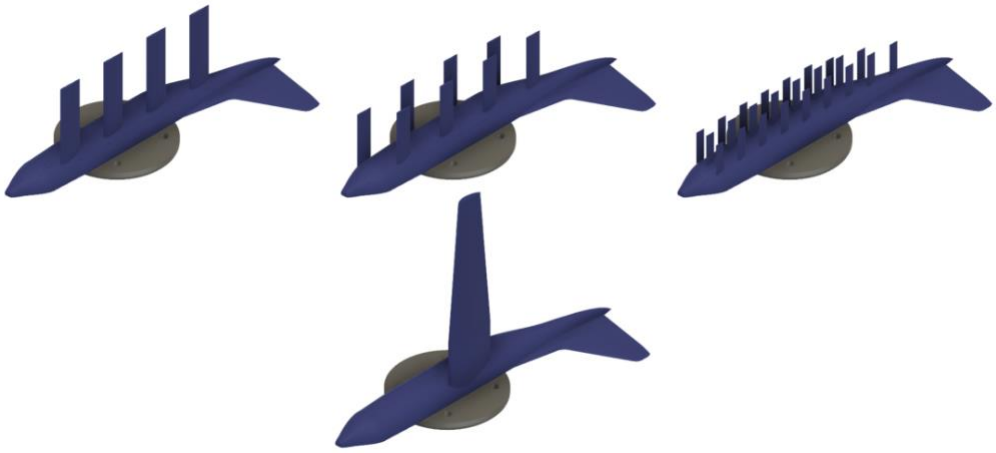

Figure 1-9 Semispan Multi-Wing configurations and Monowing baseline [39]

Table 1-1 UD-LSWT and AFRL-VT Multi-Wing configuration specifications

Configuration	Aspect Ratio	Gap (c)	Stagger (c)	Offset (c)
Monowing	4.6	----------	----------	----------
8-Wing	3.2	0	1.2	0
16-Wing	3.2	1.4	2.2	1.4
48-Wing	3.2	1.1	1.7	0

The results showed that the lift performance of the multi-wing configurations was insensitive to sideslip angle and Reynolds number. Both the low Reynolds number semispan tests and the high Reynolds number full span tests exhibited similar lift curve slopes among the different wing sets. The insensitivity to sideslip angle alleviated any concerns about fuselage blanketing reducing flow experienced by the reduced span wings. Although gap, stagger, and offset were not held constant across the different conditions, there was a general trend of a decreasing lift curve slope as the number of wings increased, as annotated in the lift coefficient plot of the high Re results in Figure 1-10. This decrease in slope correlated to lower tip to tip Aspect Ratio of the configurations from a reduction in span. Moreover, it was observed that the multi-wing configurations did not experience a drastic stall up to 60°, whereas the monowing stalled at around 15°.

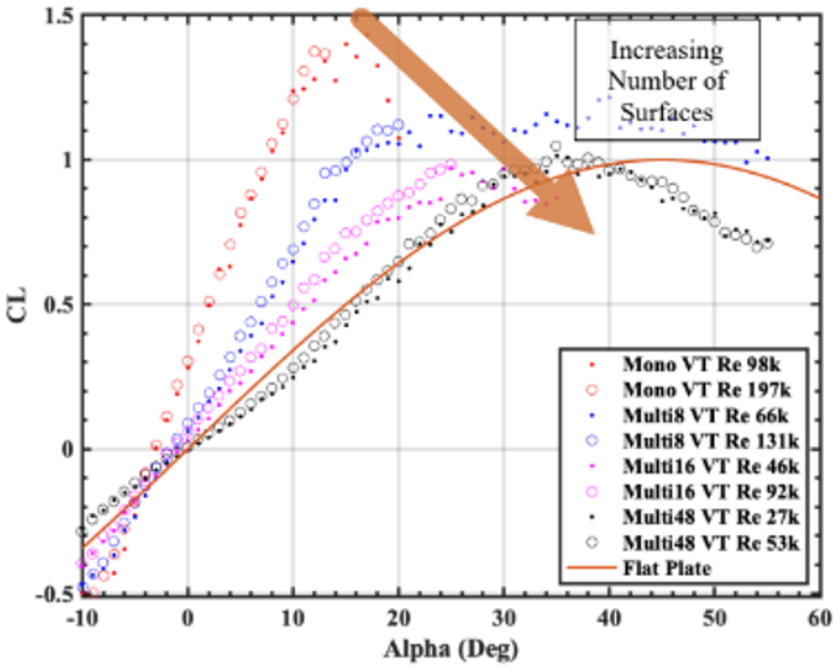

Figure 1-10 AFRL-VT high Reynolds number experimental lift coefficient across angle of attack sweep [39]

The emergence of multi-element designs along with prior studies concluding that there is potential in the distributed lift concept, leads to inter-wing optimization being a rational next step in exploring these configurations further. Understanding the wing-wing interactions allows evolved optimization of the configurations through strategic placement and relative angles of individual wings on the aircraft to achieve the desired customizable performance. Force and moment measurements are obtained to observe the performance of individual wings in a local reference frame which can then be related to the system in a global reference frame. Numerical simulations accompany experimental work for better understanding of the flow physics responsible for those changes in forces and moments.

CHAPTER 2

EXPERIMENTAL AND NUMERICAL SETUP

2.1 University of Dayton Low-Speed Wind Tunnel

All experiments were conducted in the University of Dayton Low-Speed Wind Tunnel (UD-LSWT) in the open-jet configuration. The suck-down tunnel has a 16:1 contraction ratio with 6 anti-turbulence screens and a test section size of 76.2 cm by 76.2 cm by 137 cm, with airspeeds ranging from 6.7 m/s to 36.7 m/s. The maximum turbulence intensity was measured to be 0.1% at 15 m/s by hot-wire. The fan is a 60 HP (45 KW) fan by Hartzell. The tunnel is also equipped with three interchangeable closed-jet test sections. It also houses a shuttering system capable of generating streamwise gusts up to a frequency of 5 Hz for performing unsteady aerodynamics research. The schematic of the tunnel is shown below in Figure 2-1.

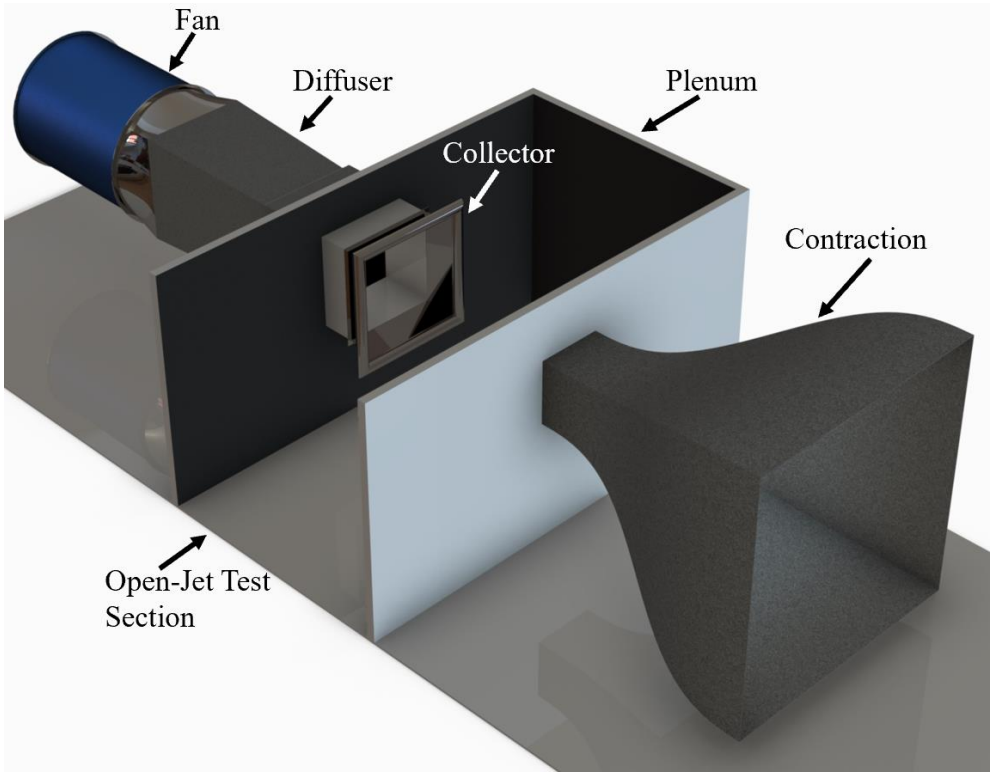

Figure 2-1 CAD schematic of the University of Dayton Low-Speed Wind Tunnel

The experimental testing campaign was conducted with up to four identical Clark Y AR 2 semispan wings, positioned at various gap and stagger locations, as well as relative angles of attack (décalage). The wings with a 0.127 m chord and 0.254 m span were 3D-printed using black polylactic acid (PLA) filament. They were printed with a 0.5 mm extrusion width, 2 mm wall thickness, 0.24 mm layer height, and 15% infill. Post-treatment was done on the wings with slight sanding for surface smoothing, followed by the application of a layer of black primer and one layer of black enamel paint. One of the 3D-printed Clark Y wings used for the experimental testing is shown in Figure 2-2.

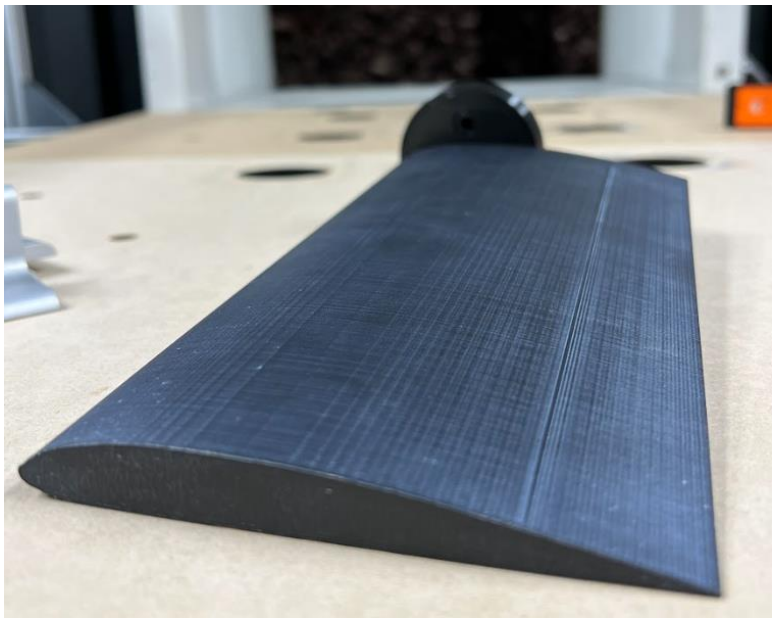

Figure 2-2 3D-Printed Clark Y AR 2 Semispan Wing

Each individual wing was attached to its own force balance and rotary stage, allowing for specific forces and torques across a variety of angle of attack combinations. Wing 1 was attached to a 6 component Analog ATI Gamma Net F/T sensor [40] which was mounted on top of a PDV PT-GD201 rotary stage [41] to adjust the angle of attack. Similarly Wing 2 was connected to a 6 component Digital ATI Gamma Net F/T sensor [40] on top of a PDV PT-GD201 rotary stage [41]. Wing 3's forces and torques were measured using a 6 component ATI Mini40-E [42], combined with a PDV PT-GD201 rotary stage [41] for angle of attack adjustment. Lastly, Wing 4 was also

equipped with an ATI Mini40-E [42] and another PDV PT-GD201 rotary stage [41] for the measurement of forces and torques during angle of attack rotation. Figure 2-3 shows a schematic of the experimental setup for the four-wing study in the UD-LSWT. Table 2-1 provides a summary of each wing and the associated sensors.

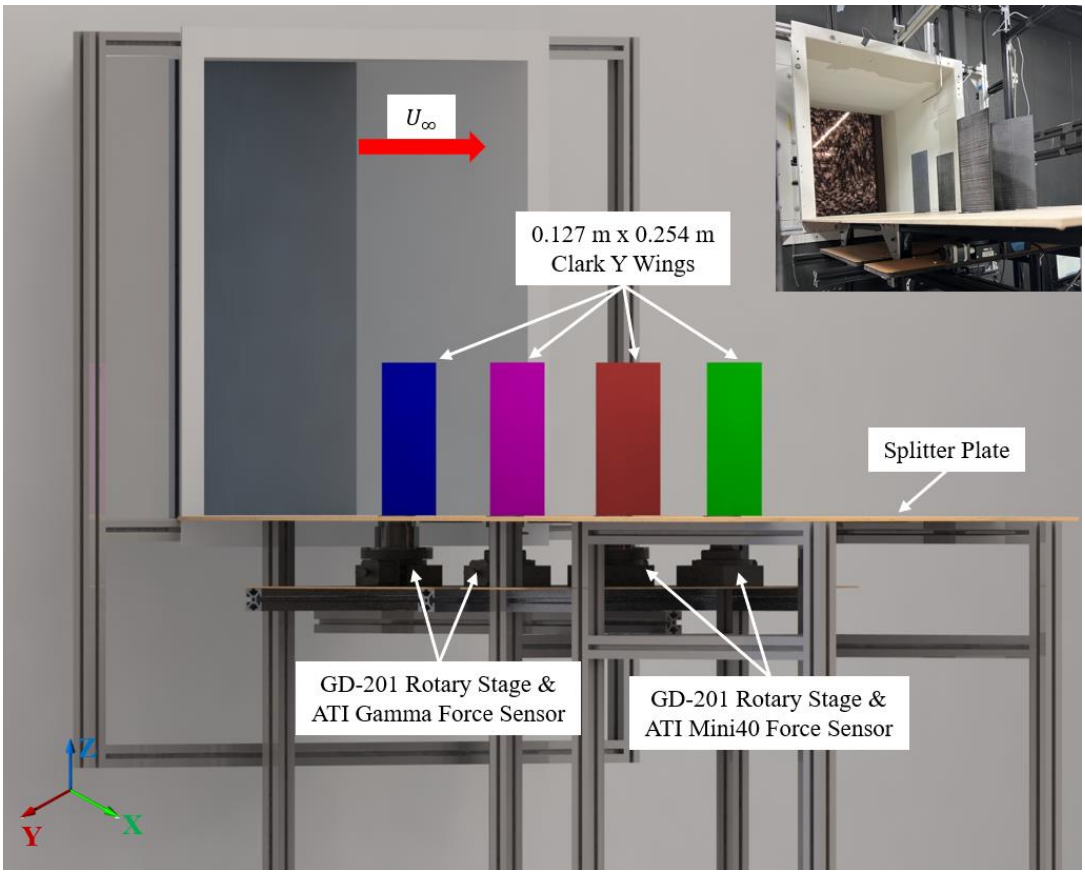

Figure 2-3 CAD schematic of experimental setup in University of Dayton Low-Speed Wind Tunnel along with real image in top right corner

Table 2-1 Individual wings with associated sensors and rotary stages

Wing	Force Balance	Rotary Stage
Wing 1 (Sweeping)	Analog ATI Gamma Net F/T	PDV PT-GD201
Wing 2 (Neighbor)	Digital ATI Gamma Net F/T	PDV PT-GD201
Wing 3 (Neighbor)	ATI Mini40-E	PDV PT-GD201
Wing 4 (Neighbor)	ATI Mini40-E	PDV PT-GD201

The ATI Gamma Net F/T sensor was orientated so that the normal and axial forces were measured through the X and Y axes. The sensing ranges of the Gamma, in the SI-65-5 Calibration

are 65 N for both X and Y axes, with uncertainties of 0.75% and 1.00% respectively. The sensor also has a torque range of 5 Nm, with an uncertainty ranging from 1.00% to 1.50%, depending on the axis. Similarly, the ATI Mini40-E Net F/T sensor was orientated to measure the normal and axial forces through the X and Y axes. In the SI-40-2 Calibration, the sensing ranges of the Mini40 are 40 N for both X and Y axes, with an uncertainty of 1.25%. The torque range is 2 Nm, with uncertainty of 1.25% to 1.50%. A sampling rate of 1000 Hz was used during data acquisition. The PDV GD-201 rotary stage had an instrument uncertainty in angle of attack of 0.01°. The sensor information is tabulated in Table 2-2.

Table 2-2 Experimental sensor calibration range and uncertainties

Sensor	Sensing Range	Uncertainty
ATI Gamma	Fx, Fy: 32 N Fz: 100 N Tx, Ty, Tz: 2.5 Nm	Fx, Fy: 0.75% and 1.00% Fx: 0.75% Tx, Ty, Tz: 1.00%-1.50%
ATI Mini40-E	Fx, Fy: 40 N Fz: 120 N Tx, Ty, Tz: 2 Nm	Fx, Fy: 1.25% Fx: 0.75% Tx, Ty, Tz: 1.00%-1.50%
PDV GD-201	0.01°	0.01°

The initial experimental testing campaign involved two Clark Y AR 2 semispan wings. The center wing was fixed in the XY plane throughout the testing as it swept through a range of angle of attack statically. Therefore, this wing will hereafter be referred to as the Sweeping Wing. Adjacent to the Sweeping Wing in the XY plane, a secondary wing, henceforth known as the Neighbor Wing, was positioned at 24 locations, representing varying gap and stagger spacing relative to the Sweeping Wing. The coordinate system was centered on the leading edge of the Sweeping Wing. The naming convention for the locations indicates that the x-coordinate represents the stagger distance (measured in chords) between the leading edges and trailing edges of the two

wings, and the y-coordinate represents the gap distance (also measured in chords). This is illustrated on the simplified dot grid in Figure 2-4 and is consistent with the biplane and prior Distributed Lift nomenclature. Disclaimer, the following spacings of the wing examples are not to scale and simply used as a visual representation.

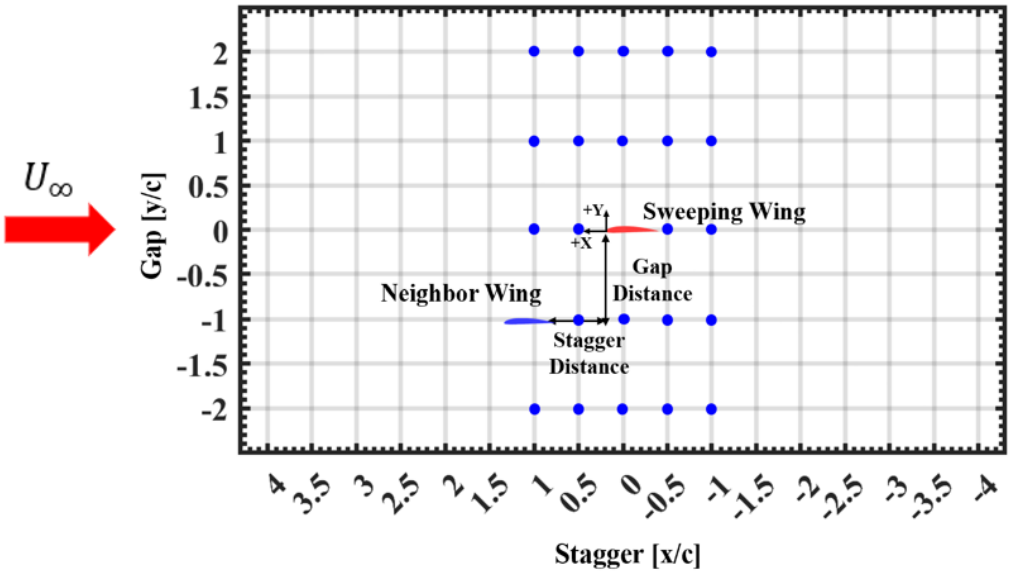

Figure 2-4 Experimental nomenclature and grid locations for Two-Wing Study

In the three-wing study, the Sweeping Wing was again fixed in the center of the XY plane, while two Neighbor Wings were arranged in groups, either in a pure 1 chord gap biplane configuration or in a 1 chord stagger tandem wing configuration. These groups were then moved around the Sweeping Wing in varying stagger and gap positions. The coordinate system was centered on the leading edge of the Sweeping Wing. The naming convention for the locations indicates that the x-coordinate represents the stagger distance, and the y-coordinate represents the gap distance, both measured in chords, between the Sweeping Wing and the centroid of the Biplane/Tandem Group as displayed on Figure 2-5.

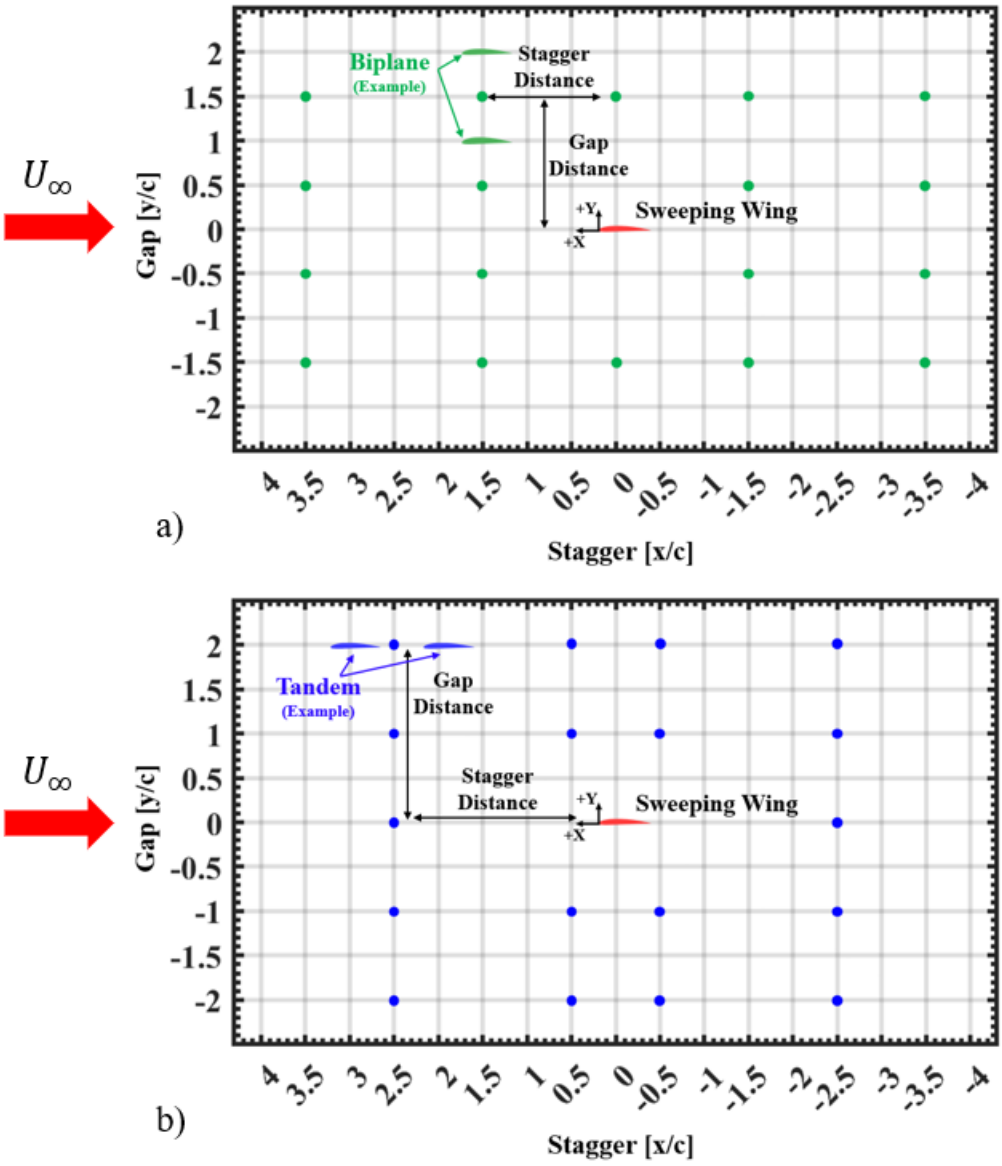

Figure 2-5 Experimental nomenclature and grid locations for Three-Wing Study with a) Biplane and b) Tandem Grouping

In the four-wing study, the Sweeping Wing was positioned at the center of the XY plane, accompanied by a Neighbor Wing in either a pure 1 chord gap biplane configuration or in a 1 chord stagger tandem wing configuration to the Sweeping Wing. Additionally, two more Neighbor Wings were grouped in either a pure 1 chord gap biplane or 1 chord stagger tandem wing configuration, and these groups were moved around the central Sweeping Wing in varying stagger and gap

positions. The stagger and gap distances were measured with respect to the centroid between both two-wing groups, as shown in Figure 2-6.

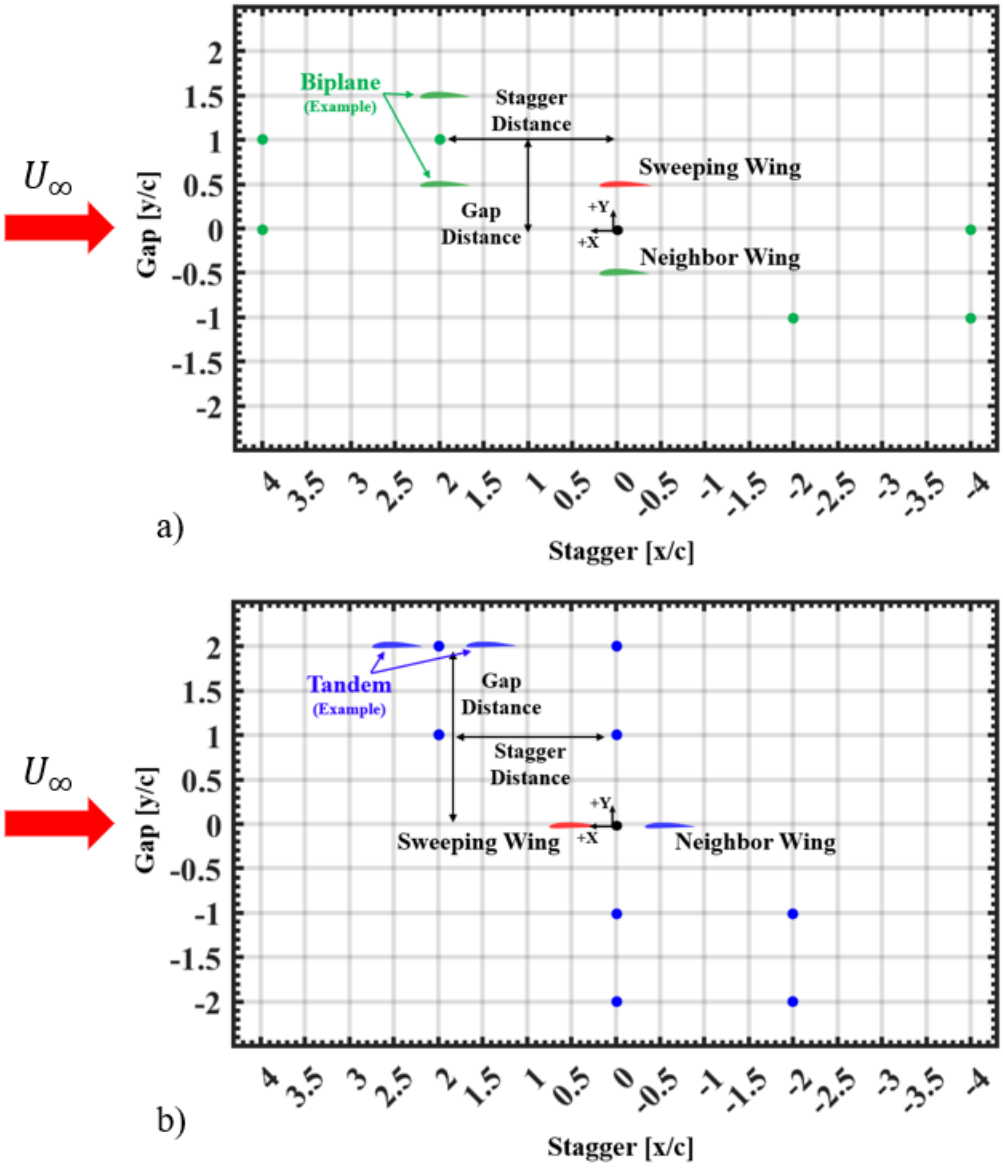

Figure 2-6 Experimental nomenclature and grid locations for Four-Wing Study with a) Biplane and b) Tandem Grouping

Table 2-3 shows a summary of the full test matrix. The baseline individual wing Reynolds number tested was 250,400 achieved by a freestream velocity of 30 m/s. The stagger and gap distances are normalized by an individual wing chord length of 0.127 m. A -20° to 20° angle of

attack sweep was always conducted on the Sweeping Wing with the other proximity wings fixed at one of the respective Neighbor Wing angle of attacks.

Table 2-3 Experimental test matrix for two, three, and four wing studies

Two-Wing					
Two Wing Group	Reynolds Number	Stagger Distances [x/c]	Gap Distances [y/c]	Sweeping Wing Alpha Range [°]	Neighbor Wing Alpha Range [°]
----------	250,400	1, 0.5, 0, -0.5, -1	2, 1, 0, -1, -2	-20 to 20	-10, -3, 8, 13, 20
Three-Wing					
Two Wing Group	Reynolds Number	Stagger Distances [x/c]	Gap Distances [y/c]	Sweeping Wing Alpha Range [°]	Neighbor Wings Alpha Range [°]
(0c St, 1c G) Biplane	250,400	3.5, 1.5, 0, -1.5, -3.5	1.5, 0.5, -0.5, -1.5	-20 to 20	-3, 3, 8
(1c St, 0c G) Tandem	250,400	2.5, 0.5, -0.5, -2.5	2, 1, 0, -1, -2	-20 to 20	-3, 3, 8
Four-Wing					
Two Wing Group	Reynolds Number	Stagger Distances [x/c]	Gap Distances [y/c]	Sweeping Wing Alpha Range [°]	Neighbor Wings Alpha Range [°]
(0c St, 1c G) Biplane	250,400	4, 2, -2, -4	1, 0, -1	-20 to 20	-3, 3, 8
(1c St, 0c G) Tandem	250,400	2, 0, -2	2, 1, -1, -2	-20 to 20	-3, 3, 8

It is important to note that not all four quadrants from the different testing grids were physically positioned. Changing the reference frame regarding which wing is sweeping allows one physical location to simulate two different configurations. Figure 2-7 provides a visual representation of this advantageous experimental setup manipulation. When the red wing is designated as the Sweeping Wing and the blue wing becomes the Neighbor Wing at a fixed angle of attack, the corresponding test location is (1c St, 1c G). If the roles are reversed, with the blue wing sweeping and the red wing fixed, the resulting test location is (-1c St, -1c G), even though the physical position of the wings have not changed.

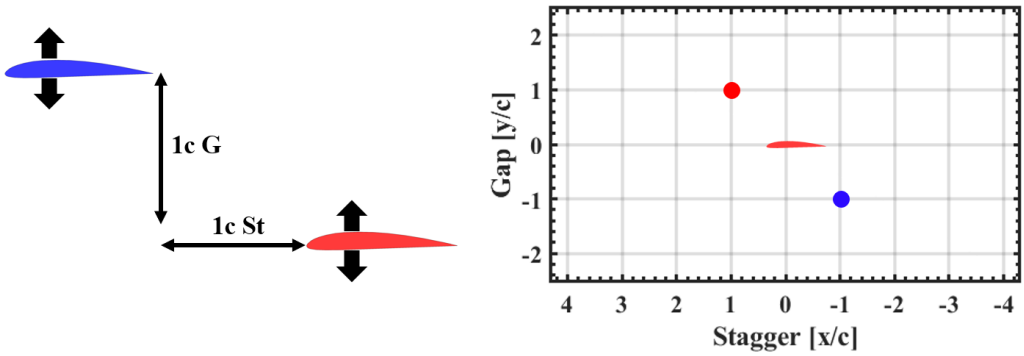

Figure 2-7 Reference Frame manipulation to simulate two testing locations with one physical configuration

2.2 FlightStream

FlightStream [43] is a potential flow solver with two main types: pressure-based and vorticity-based. This study utilized the pressure-based solver due to its closer agreement with prior UD-LSWT experimental results. The solver calculates the pressure fields on the model geometry to determine the aerodynamic loads. The use of source and sink panels, along with doublet panels on the trailing edges of the wings, facilitates the pressure-based potential flow solver.

Figure 2-8 represents the surface mesh for the simulations with one of the four-wing configurations as an example. Each individual wing has a structured mesh with 60 node points chordwise and 161 node points spanwise, generated in an OpenVSP [44] model and imported to FlightStream as a Pittsburgh Three Dimensional (.p3d) file. A dual side growth rate of 1.08 was applied to resolve the chordwise mesh on the LE and TE. A splitter plate was added with the same dimensions as the one used in the experimental study, measuring 0.9144 m by 1.524 m, to closely match all conditions. FlightStream generated a “sheet” to represent the splitter plate with a mesh of 40 node points by 80 node points. A trailing edge line was marked, and a wake termination node placed on the node connecting the TE and splitter plate for each wing.

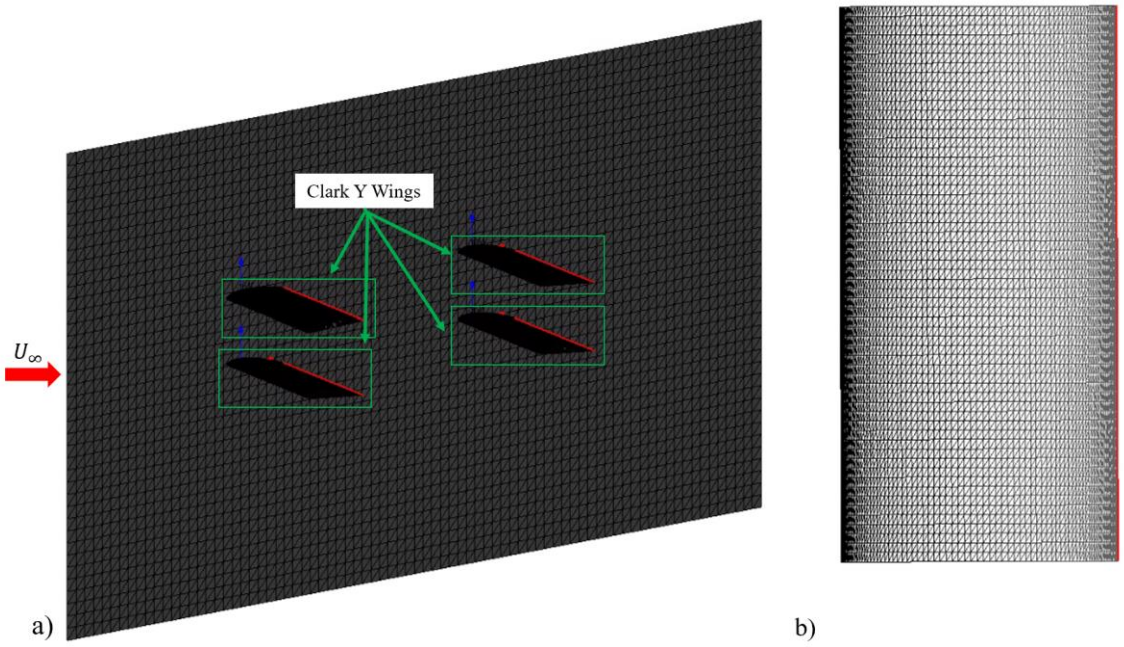

Figure 2-8 FlightStream surface mesh of a) isometric view of four wings and splitter plate and b) top view of isolated wing

Mesh sensitivity study was performed on three different wing surface meshes displayed in Figure 2-9: the course (20 chordwise nodes by 81 spanwise nodes), medium (60 chordwise nodes by 161 spanwise nodes), and fine (120 chordwise nodes by 321 spanwise nodes) meshes. The tandem configuration was chosen to perform the mesh sensitivity due to the complex wake dominated flow field. FlightStream simulations were performed on these three meshes and the error from the experimental value was calculated and plotted below in Figure 2-10. The percent error, calculated with Equation (11), decreases with the increase in the number of mesh size. However, the computational time for the fine mesh increased by 400% when compared to the medium mesh. Therefore, the medium mesh design was chosen for all the analysis.

$$Err = \frac{|FlightStream - Experiment|}{Experiment} \quad \textbf{(11)}$$

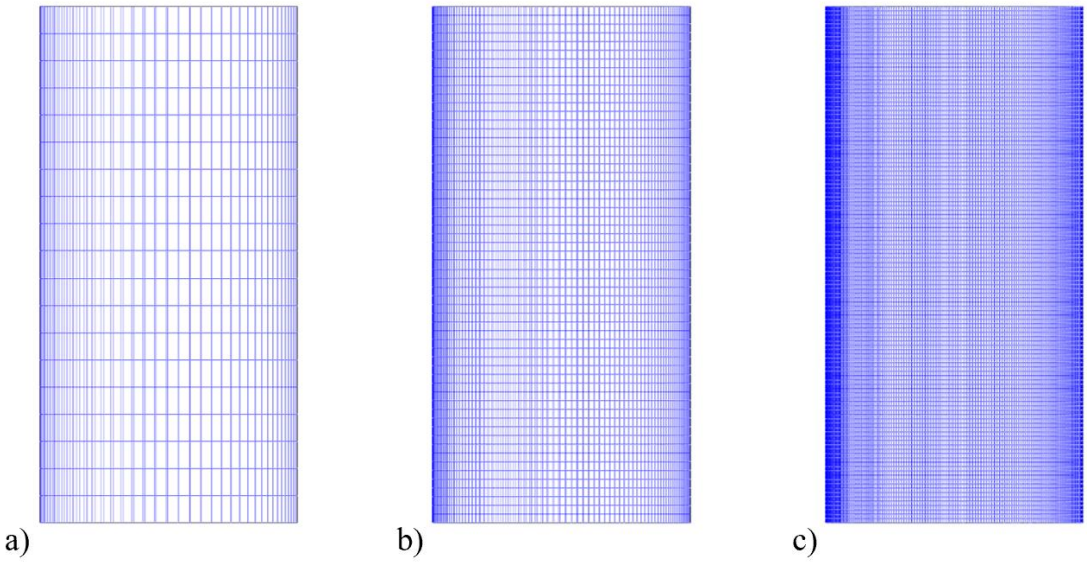

Figure 2-9 OpenVSP wing with a) course, b) medium, and c) fine surface meshes

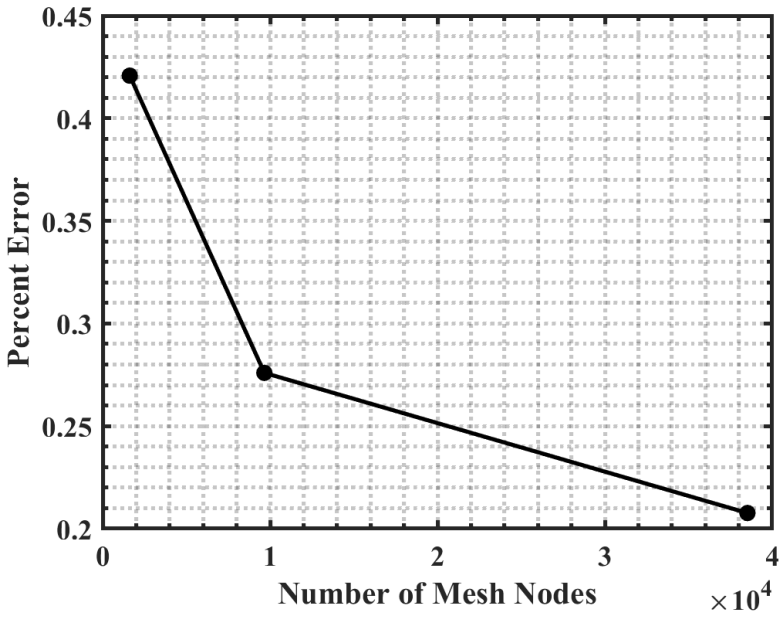

Figure 2-10 FlightStream mesh sensitivity

Sensitivity analyses were previously conducted for many of the individual solver parameters but will not be included in this work. The relevant solver parameters that were chosen for all simulations presented are summarized in Table 2-4 for reference. The atmospheric properties were

matched with the average values recorded during testing in the UD-LSWT. In the solver initialization, the wake is calculated 5 meters downstream of the wings with surface proximity avoidance enabled. The steady solver was run until convergence tolerance was met for the velocity and pressure residuals. A transitional turbulent viscous boundary layer was simulated with viscous coupling enabled. The axial model was used for flow separation.

Table 2-4 FlightStream Solver Parameters

Fluid Properties	
Density	1.189 kg/m^3
Viscosity	$1.78\times10^{-5}\ Pa-sec$
Pressure	$1.0132402\times10^{5}\ Pa$
Steady Solver Parameters	
Viscous Boundary Layer	Transitional Turbulent
Viscous Coupling	Enabled
Flow Separation	Axial Model
Convergence Threshold	1.00×10^{-5}

CHAPTER 3

ESTABLISHING BASELINES

Due to the various approaches that will be employed in the analysis of the data collected in this study, it is essential to establish and understand the multiple baselines that will be used for comparison. In the recent distributed lift study by Mongin et al. [39], all multi-wing configurations were compared to a baseline of a monowing. The monowing had a wing area equal to the sum of all the individual wings in each multi-wing configuration, as visually represented in Figure 1-9. In this study, a slightly different approach is taken, where instead of decreasing individual wing size as more wings are added to maintain a similar total combined wing area, the individual wing size is kept constant as more wings are added. This effectively increases the total combined wing area between studies.

3.1 Single Wing Baseline

In this study, the primary baseline is the performance of a single standalone wing not in close proximity to any other wings. This Single-Wing Baseline has an area equal to one of the wings used in the multiple wing studies. In other words, the baseline is a Clark Y wing with a 0.127m chord by 0.254m span. To attain the comparable single wing baseline, one of the Clark Y wings was tested separately at different positions in the spanwise direction and downstream of the wind tunnel inlet to ensure repeatability at various spatial locations in the test section. Figure 3-1 shows the averaged lift curve of the single wing from all the different tests, with dashed lines representing error bars. The baseline cases see negative stall around 10° and positive stall around 18°, with a $C_{L_{Max}}$ of 1.1. The lift curve slope (C_{L_α}) in the linear region of the averaged curve is calculated to be 0.057 deg^{-1}, which is around $C_{L_\alpha} = \pi\alpha$. This is consistent with low AR wing behavior. Using Helmbold's low aspect ratio equation [45] in Equation (12), the aspect ratio corrected lift curve slope of the averaged baseline is calculated with C_{l_α} as 2π for thin airfoils and an effective AR of

2.8. The corrected lift curve slope was determined to be 0.0564 deg^{-1} and is also plotted in Figure 3-1 for comparison.

$$C_{L_\alpha} = C_{l_\alpha} \frac{AR}{\left(\frac{C_{l_\alpha}}{\pi}\right) + \sqrt{\left(\frac{C_{l_\alpha}}{\pi}\right)^2 + AR^2}} \quad (12)$$

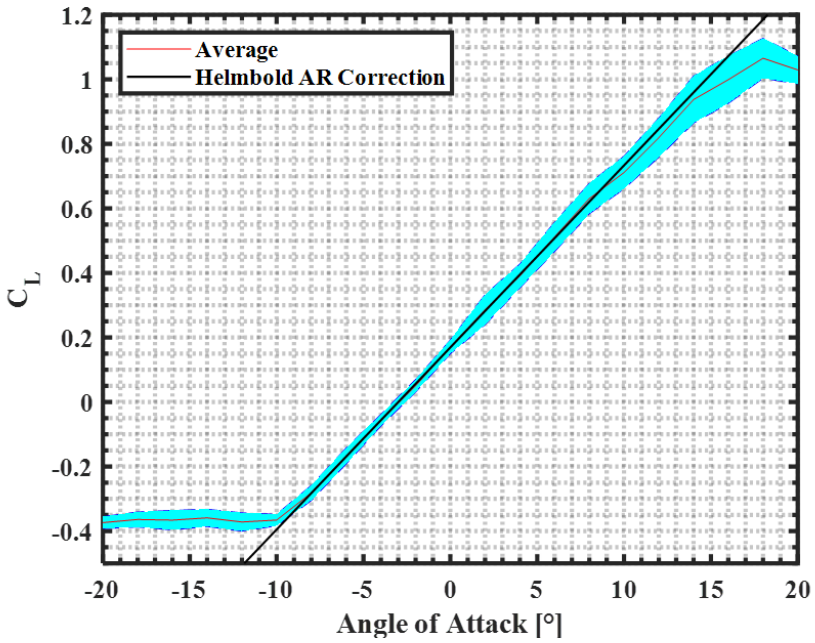

Figure 3-1 Baseline AR 2 Clark Y Lift Curve

3.2 Two-Wing Group Baselines

As described in Chapter 2 under the Experimental Setup, in the three and four wing studies, two-wing groups of biplanes or tandem are used. From the two-wing study, an experimental baseline can be established that takes into consideration the aerodynamic biplane/tandem interaction in an isolated environment without increased interactions from the addition of a third or fourth wing. With both the Sweeping Wing and Neighbor Wing at various independent angles of attack, several instances exist when both wings are at the same angle of attack. In the two-wing groups, those Neighbor Wings will always remain in a biplane or tandem configuration at the same angle of attack, and therefore, in order to achieve a baseline measurement that accounts for the

wing-wing interactions, the C_L of the biplane and tandem system can be experimentally collected at angles of attack of -10°, -3°, 8°, 13°, and 20°. Linear interpolation can then be performed to obtain the C_L of the biplane or the tandem as single system at 3° angle of attack. Figure 3-2 shows this linear trend for both the system C_L of the biplane and tandem configurations. Both configurations display a deviation in the lift curve slope from the standalone wing, with the tandem exhibiting behavior similar to an AR reduction compared to the biplane.

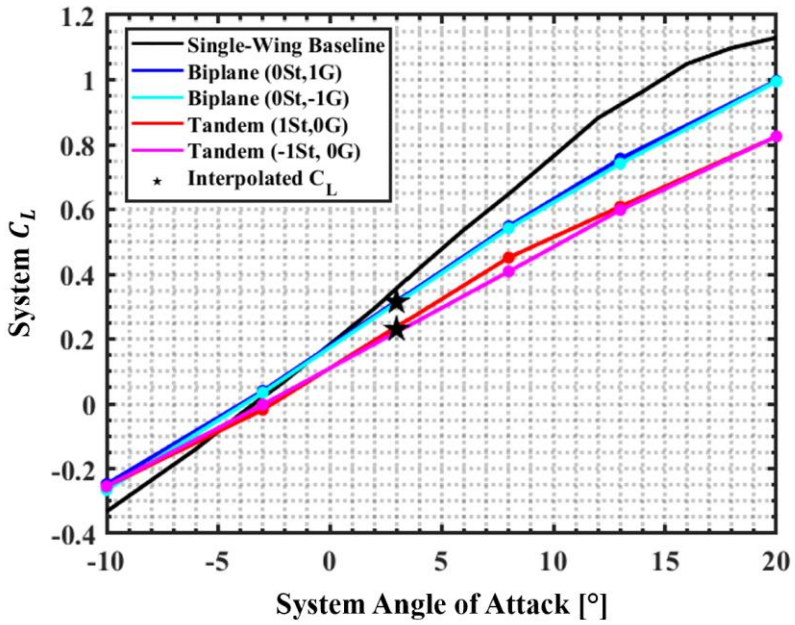

Figure 3-2 Baseline Biplane and Tandem Combined Lift Coefficient

It is important to note that while this will be referred to as a biplane/tandem angle of attack, these two-wing groups are not being rotated from the centroid between two wings, but at the quarter-chord of both individual wings. Figure 3-3 depicts the difference between these two pivot points. On the right, two wings are both individually rotated at their quarter chord and a vertical reference line can be drawn from trailing edge tip to tip. Meanwhile on the left, the same 0° angle of attack spaced configuration is rotated along the centroid between the two wings and now there is no longer a straight vertical line that can connect the two tips. There will be minimal differences within the tested angle of attack range of -3°, 3°, and 8° in terms of the physical gap /stagger

remaining as 1 chord for the respect configuration with the quarter-chord rotation, but this should still be taken into consideration.

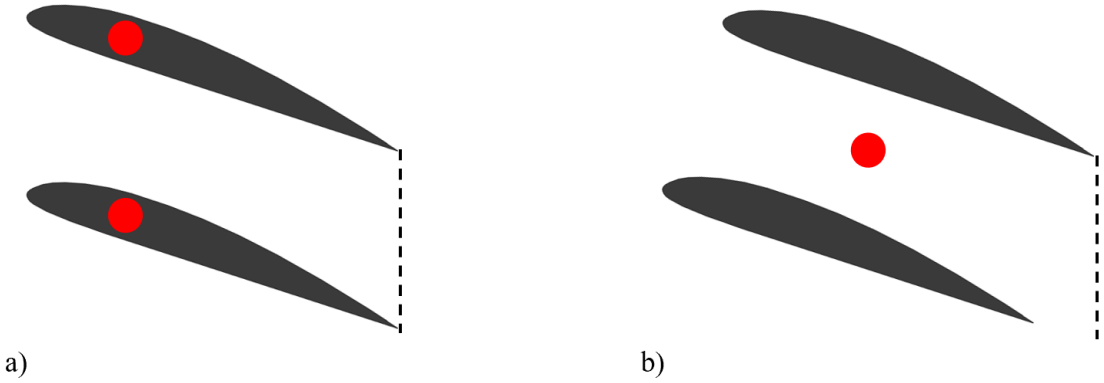

Figure 3-3 Difference between chosen pivot point for two-wing groups

3.3 Multi-Wing System Baselines

With the ultimate goal being to determine beneficial and detrimental configurations for distributed lift aircraft wing placement, a system analysis is required. When looking at the system analysis of all wings combined to simulate an aircraft, the aerodynamic efficiency, also known as the L/D mathematically expressed in Equation (13), is used as the metric. In air vehicle design, the L/D as a strong effect on range and endurance performance as quantified in the Bréguet Range (distance) and Endurance (time) equations in Equation (14) and Equation (15) [46]. Therefore, knowing the L/D of a distributed lift configuration can provide valuable insight into the possible mission profiles available to observe where distributed lift may fill current gaps in aircraft performance.

$$L/D_{sys} = \frac{\sum L_n}{\sum D_n} \quad \textbf{(13)}$$

$$Range = \int_{W_i}^{W_f} \frac{U_\infty}{c} \frac{C_L}{C_D} \frac{1}{W} dW \quad \textbf{(14)}$$

$$Endurance = \int_{W_i}^{W_f} \frac{1}{c} \frac{C_L}{C_D} \frac{1}{W} dW \quad \textbf{(15)}$$

For this system analysis another comparison curve, termed Ideal System Efficiency (ISE), is introduced to account for the varying number of wings (n). ISE, as defined by Equation (16), is used to compare the extent of aerodynamic interactions relative to the linear superposition of the lift and the drag forces. Efficiencies higher than the linearly superimposed ratio of the forces represents positive aerodynamic interference and vice-versa.

$$Ideal\ System\ Efficiency = \frac{L_{Baseline\ at\ \alpha_{Sweeping}} + n * L_{Baseline\ at\ \alpha_{Neighbor}}}{D_{Baseline\ at\ \alpha_{Sweeping}} + n * D_{Baseline\ at\ \alpha_{Neighbor}}} \quad \textbf{(16)}$$

Figure 3-4 visually demonstrates how the ISE is calculated. The Single-Wing Baseline is used to extract the "ideal" lift and drag coefficient for each wing at their specific angle of attack. These determined lift and drag coefficients are then added and divided to get an ideal total L/D, without any positive or negative wing-wing interactions, known as the ISE. The example below is of a four-wing configuration. For instance, when the Sweeping Wing is at 14° and the three Neighbor Wings are at 8°, the ISE is calculated by taking the sum of the Single-Wing Baseline lift at 14° and thrice the Single-Wing Baseline lift at 8°, and then dividing it by the sum of the Single-Wing Baseline drag at 14° and thrice the Single-Wing Baseline drag at 8°. Doing this same process across all Sweeping Wing angles of attack results in the green dashed line which is plotted along with the standard Single-Wing Baseline L/D curve and shows clear differences. The assumption is that the multi-wing configurations studied should follow the basic trends of the ISE closer than of the Single-Wing Baseline.

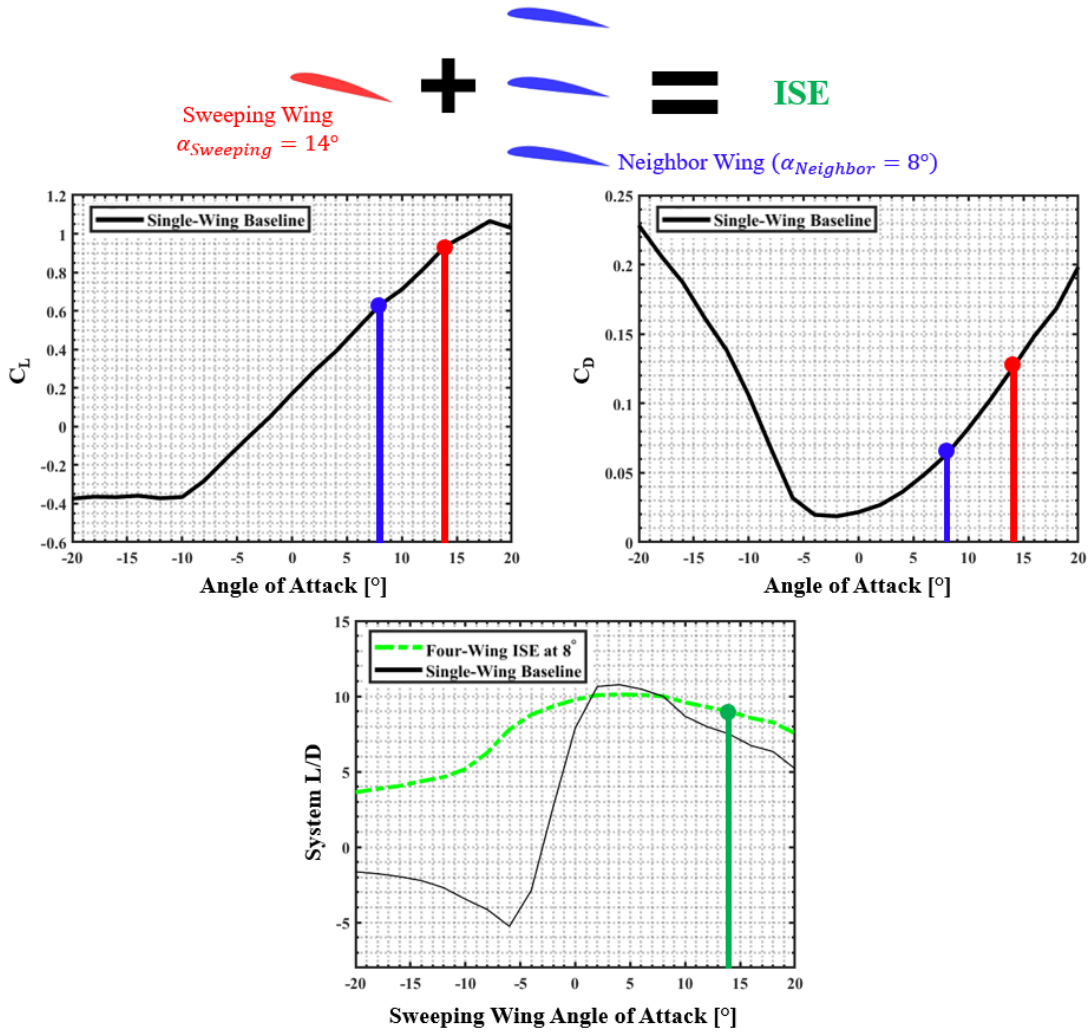

Figure 3-4 Visual representation of calculating ISE for four-wing configuration with $\alpha_{Sweeping} = 14°$ and three Neighbor Wings at $\alpha_{Neighbor} = 8°$

Figure 3-5 displays the ISE for the two, three, and four-wing systems at three different α_{Group} values, allowing for comparison between the effect of angle of attack and the number of wings relative to a baseline. When the wings are at $\propto_{L=0}$, there is a large difference between the two, three, and four wing systems. However, as the fixed wing angle of attack increases, these differences diminish. Notably, despite an increased number of wings, the maximum L/D never surpasses that of the one-wing baseline. Once α_{Group} rotates beyond 3°, the ISE becomes entirely positive as the lift generated by the fixed wings counteract any negative lift produced by the

sweeping wing. Each two, three, and four-wing experimental configuration can have its system performance plotted alongside its respective ISE baseline to not only determine which configurations perform the best but also ascertain if any benefit from positive proximity interactions between wings to surpass the ISE.

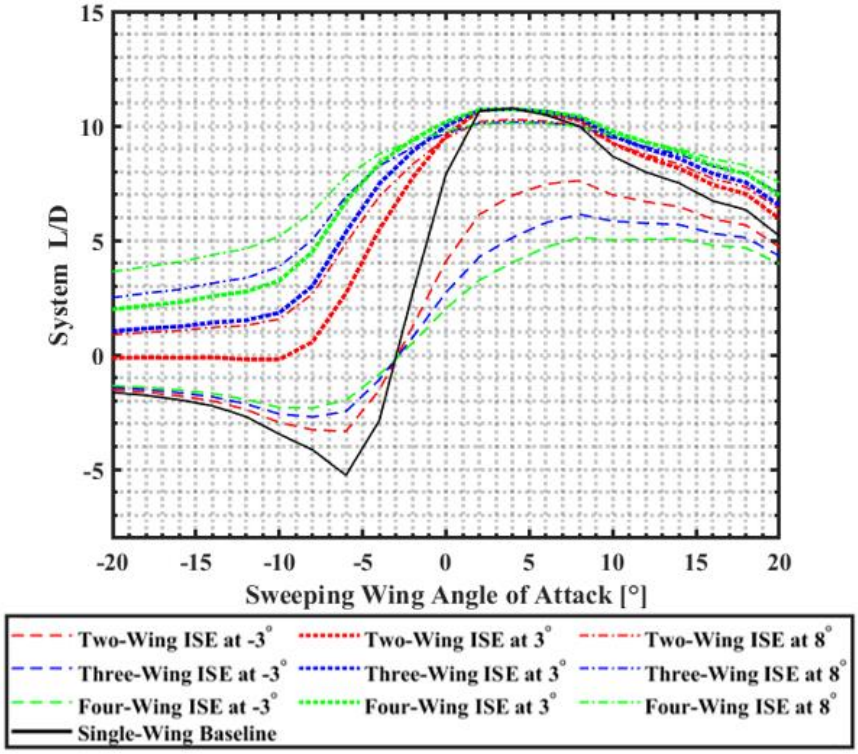

Figure 3-5 Comparison of Ideal System Efficiency baselines for one, two, three, and four wings

CHAPTER 4

TWO-WING INTERACTION RESULTS

While multiple studies have been conducted on two-wing configurations such as biplanes and tandem as described in the literature review, an experimental investigation of two wings is performed with new objectives aimed at laying the groundwork for more configurations with increased number of wings. The data collected is analyzed with both an individual wing perspective along with the total system performance. FlightStream numerical simulations are validated with experimental data for drastically different configurations. Then use of FlightStream is introduced as a trustworthy tool to gather more information about interesting experimental findings.

4.1 Individual Wing Performance

As a benefit of both wings being connected to force balances, the individual force and torque measurements can be analyzed to quantify the interactions between the wings. Spatial contour plots are utilized to provide a comprehensive visualization of how performance varies across the testing grid. Figure 4-1 is an example of one of the contours where the Sweeping Wing, the wing in the center, is at -20° and the Neighbor Wing, which could be placed at any of the grid positions, is at a fixed angle of attack of 20°. In this case, the colors at each point on the contour represent the change in lift coefficient of the Sweeping Wing relative to the single-wing baseline established in Chapter 3 when the Neighbor Wing is positioned at that particular stagger and gap location at a specific fixed angle of attack. Based on the color map, blue indicates an increase in lift coefficient of the Sweeping Wing from the baseline, signifying that the Neighbor Wing has a positive influence, while red indicates a negative influence from the Neighbor Wing on the Sweeping Wing.

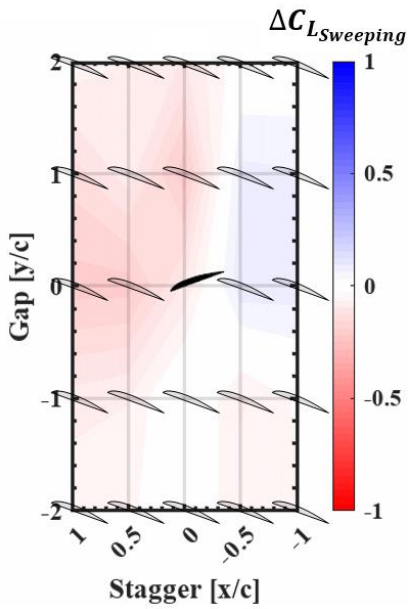

Figure 4-1 Visual breakdown of $\Delta C_{L_{Sweeping}}$ contour when $\alpha_{Sweeping} = -20°$ and $\alpha_{Neighbor} = 20°$

The above contour example is created for several combinations of decalage between the two wings and displayed in a contour array in Figure 4-2. The contours represent the Sweeping Wing ΔC_L determined by subtracting the Single-Wing Baseline C_L from the Sweeping Wing C_L at different gap and stagger locations. Throughout all the different Sweeping Wing and Neighbor Wing angle of attack combinations, the Sweeping Wing mostly experiences a decrement when the Neighbor Wing is placed at any of the 24 positions around it. This decrement becomes increasingly prominent at greater Sweeping Wing and Neighbor Wing angles in the bottom right of the figure array. For the tandem configuration, specifically with the Neighbor Wing upstream, the Sweeping Wing's lift coefficient drops significantly when compared to the baseline. When the Neighbor Wing is at -10°, the opposite is true as the Sweeping Wing experiences a slight increment in C_L. Minimal effect in C_L is observed when the Neighbor Wing is placed downstream as it does not measurably affect the flow experienced by the Sweeping Wing. The Neighbor Wing at it's $\propto_{L=0}$ (-3°) in general causes only small Sweeping Wing C_L variance from the baseline at all positions compared to other $\alpha_{Neighbor}$ values.

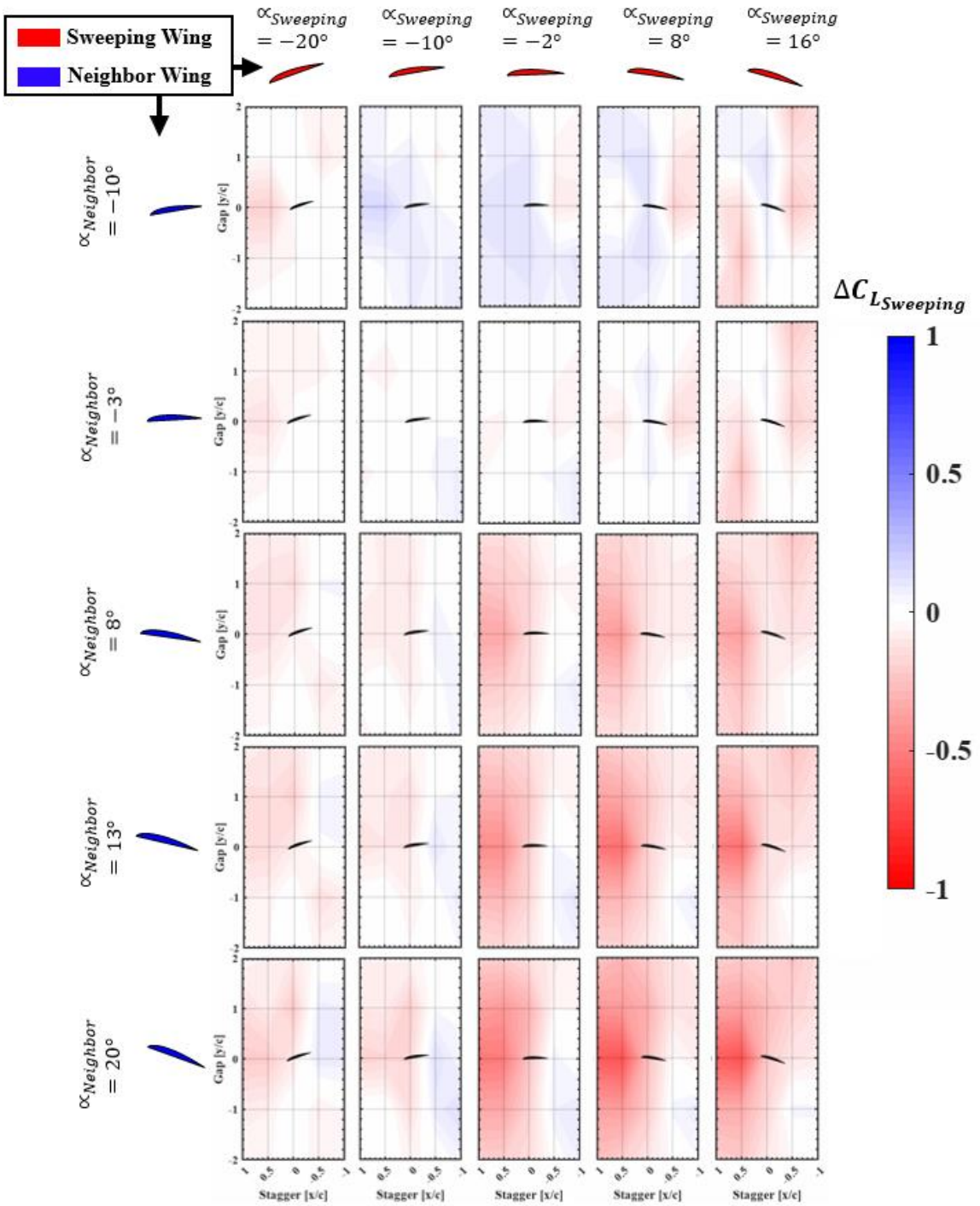

Figure 4-2 Contour array of Sweeping Wing lift coefficient difference from Single-Wing Baseline at different décalage

Now the reference frame can be flipped to observe how the Neighbor Wing's performance changes as a function of its proximity to the Sweeping Wing at all tested locations. In Figure 4-3,

the contour colors at each point represent the change in lift coefficient of the Neighbor Wing placed at that point from the single-wing baseline when the Sweeping Wing is at the center. The color blue means that there is a positive increment in lift coefficient on the Neighbor Wing most likely caused by the presence of the Sweeping Wing, while red means that the Sweeping Wing has a negative influence on the Neighbor Wing.

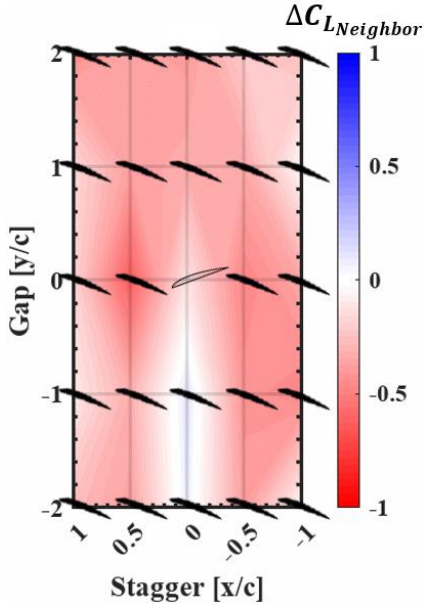

Figure 4-3 Visual breakdown of $\Delta C_{L_{Neighbor}}$ contour when $\alpha_{Sweeping} = -20°$ and $\alpha_{Neighbor} = 20°$

Figure 4-4 is another contour array for a side-by-side comparison for the Neighbor Wing. Just as the Sweeping Wing saw decrements in C_L when the Neighbor Wing was placed upstream, the Neighbor Wing sees decrements when Sweeping Wing is placed upstream with some inconsistencies. Increments are witnessed at low $\alpha_{Sweeping}$ and $\alpha_{Neighbor}$ where $\alpha_{Sweeping}$ = -20° and -10° with $\alpha_{Neighbor}$ = -10°, -3°, and 8°. This occurred for Sweeping Wing but less frequently as it was only observed when $\alpha_{Sweeping}$ = -10°, -2°, and 8° with $\alpha_{Neighbor}$ = -10°. Around the zero lift angle of attack (-2° or -3°), the influence of both wings on each other is at its minimum. Both Figure 4-2 and Figure 4-4 do show that even with both wings close to $\propto_{L=0}$, there are slight

increments and decrements at select locations due to physical localized disruptions in the flow resulting from the presence of the companion wing.

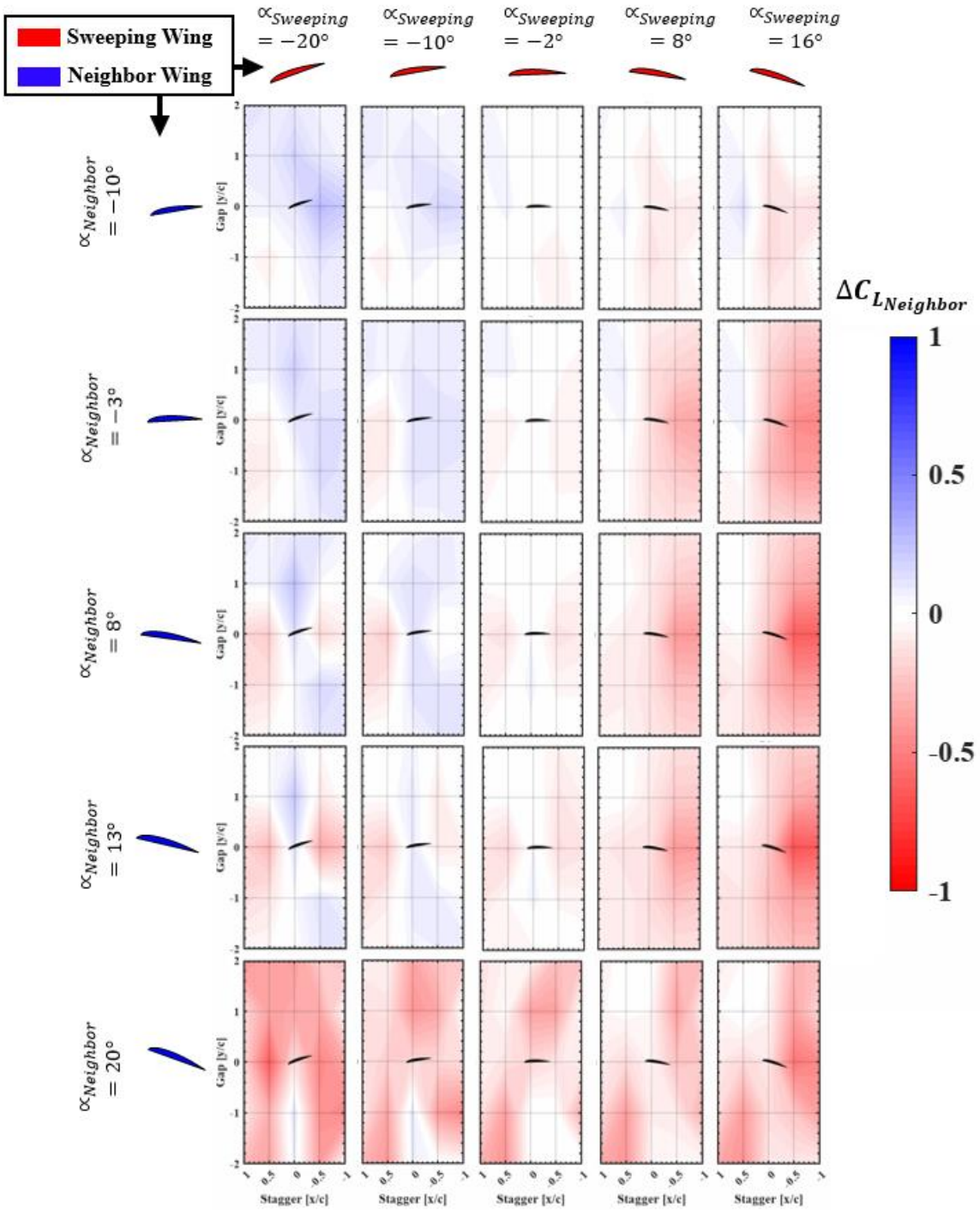

Figure 4-4 Contour array of Neighbor Wing lift coefficient difference from Single-Wing Baseline at different décalage

4.2 System Performance

Combining the performance of the two wings leads to a system performance perspective. This allows analysis of what two wing configurations could be overall beneficial or detrimental for an aircraft.

The system analysis is broken down into the five different Neighbor Wing angle of attack ($\alpha_{Neighbor}$) sets. The three highest and lowest performing configurations in terms of system L/D are plotted and compared to the Single-Baseline and ideal system efficiency (ISE). Spatial contours, just like those used in the individual wing analysis above, are generated at the trough and peaks of the two-wing configuration L/D curves to provide perspective of how the plotted high and low performing locations perform compared to the other Neighbor Wing locations. The Neighbor Wing locations in these high and low performing cases are also marked on the contours for a spatial reference.

Across all of the $\alpha_{Neighbor}$ sets, the best performing combined wing-wing cases can achieve between 30% and 130% of the isolated single-wing maximum L/D. The worst performing cases range from 10% to 70% of the single-wing efficiency. The large ranges of maximum L/D for both the high and low performers emphasize high sensitivity to the Neighbor Wing's angle of attack.

When the Neighbor Wing is placed at -10°, around a Clark Y's negative stall, in Figure 4-5, there is minimal difference between the three highest performing and lowest performing cases. The minimum L/D occurs around -4° and maximum around 16° compared to the Single-Wing Baseline at -6° and 4°. All three high performers are below the single-wing maximum L/D but do surpass the ideal system efficiency curve.

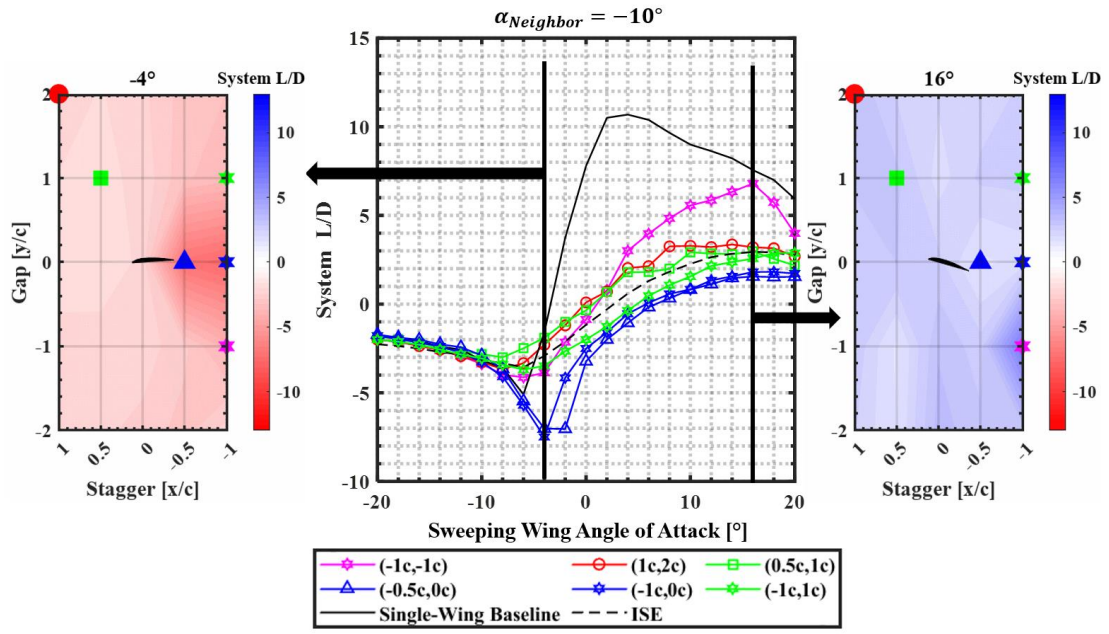

Figure 4-5 System L/D of various two-wing configurations as Sweeping Wing sweeps and Neighbor Wing is fixed at -10°

Figure 4-6 has the Neighbor Wing at -3°, the zero-lift angle of attack for a Clark Y ($\propto_{L=0}$), where the difference between the high and low performing configurations become prominent. Increments in system L/D are visible at high Sweeping Wing angles of attack for the high performing configurations. The three highest system L/D cases happen at a Neighbor Wing location at negative gap and low stagger where they all perform very similarly. The lowest aerodynamic efficiency results from the tandem configurations which was also seen in the above Figure 4-5. The range between the relative trough and peak of the L/D curves drops dramatically compared to the previous figure as the trough occurs around -4° and the peak at around 4°.

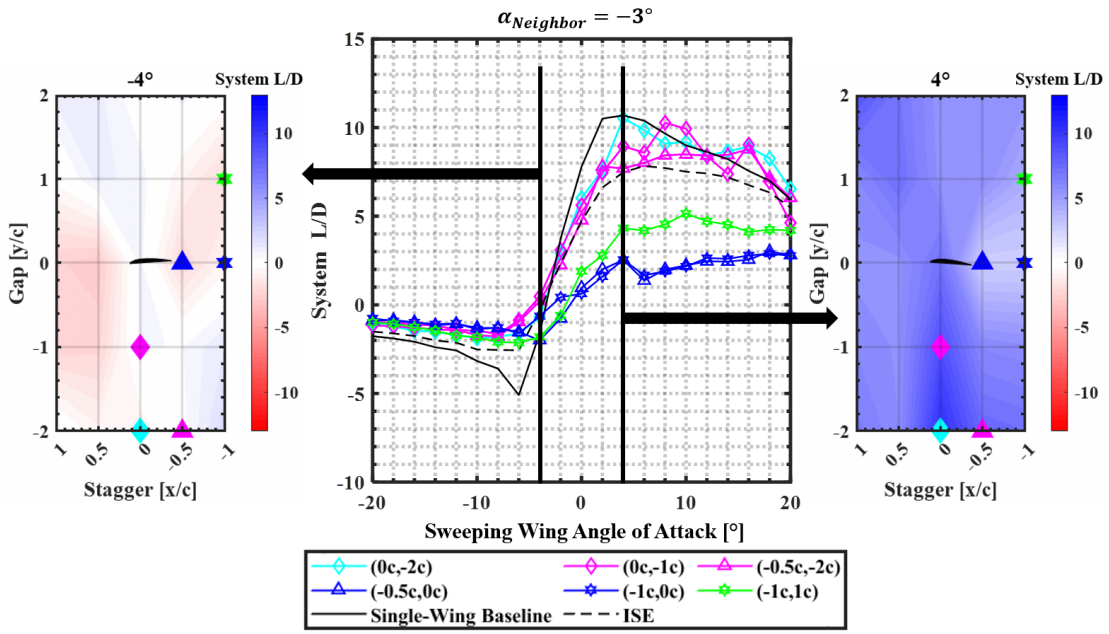

Figure 4-6 System L/D of various two-wing configurations as Sweeping Wing sweeps and Neighbor Wing is fixed at -3°

As $\alpha_{Neighbor}$ increases to 8° in Figure 4-7 and 13° in Figure 4-8, the two-wing configuration's efficiency approaches that of the single-wing and also becomes positive at negative Sweeping Wing angles of attack. This is an artifact of the relatively fixed contribution to lift of the Neighbor Wing (at a fixed angle) at high angles of attack overcoming lift decrements from the Sweeping Wing at negative angles of attack. The isolated baseline Clark Y lift curve produces a minimum C_L of around -0.3 at -20° and surpasses this magnitude of C_L value by 4°. This results in a fully positive system C_L when the Neighbor Wing is above 4°. The ideal system efficiency makes a similar transition at the negative Sweeping Wing angles of attack. The combined wing-wing configurations surpass the maximum efficiency of the single-wing and ideal two-wing system when the Neighbor Wing is at a high positive angle of 8° and 13°. A notable trend is a gradual shift of the maximum lift to drag ratio to lower Sweeping Wing angles of attack with increment in Neighbor Wing angle of attack.

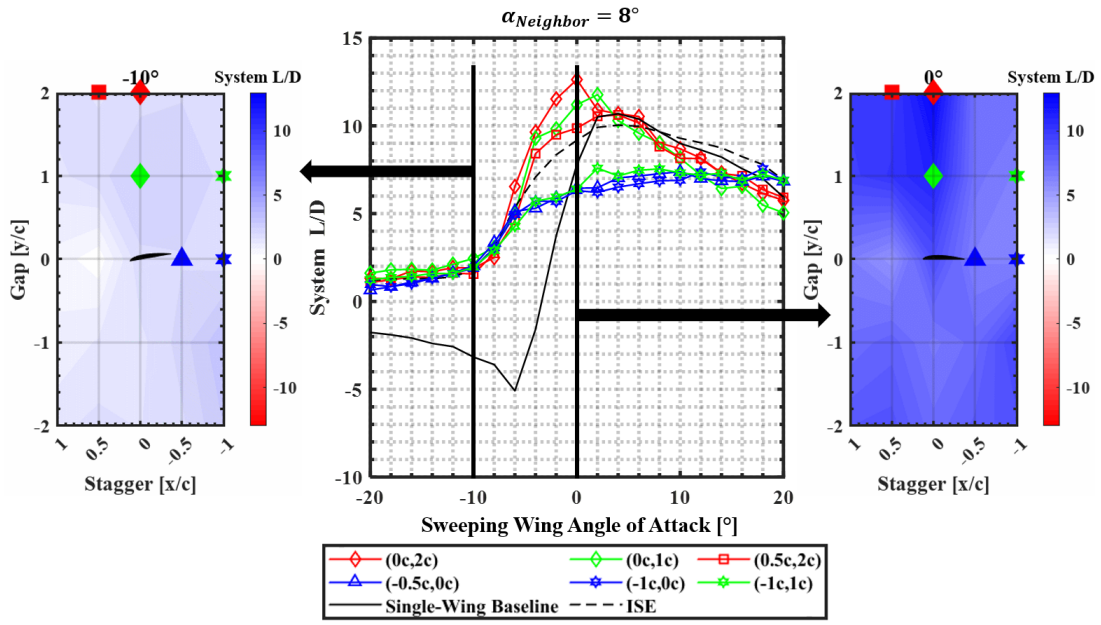

Figure 4-7 System L/D of various two-wing configurations as Sweeping Wing sweeps and Neighbor Wing is fixed at 8°

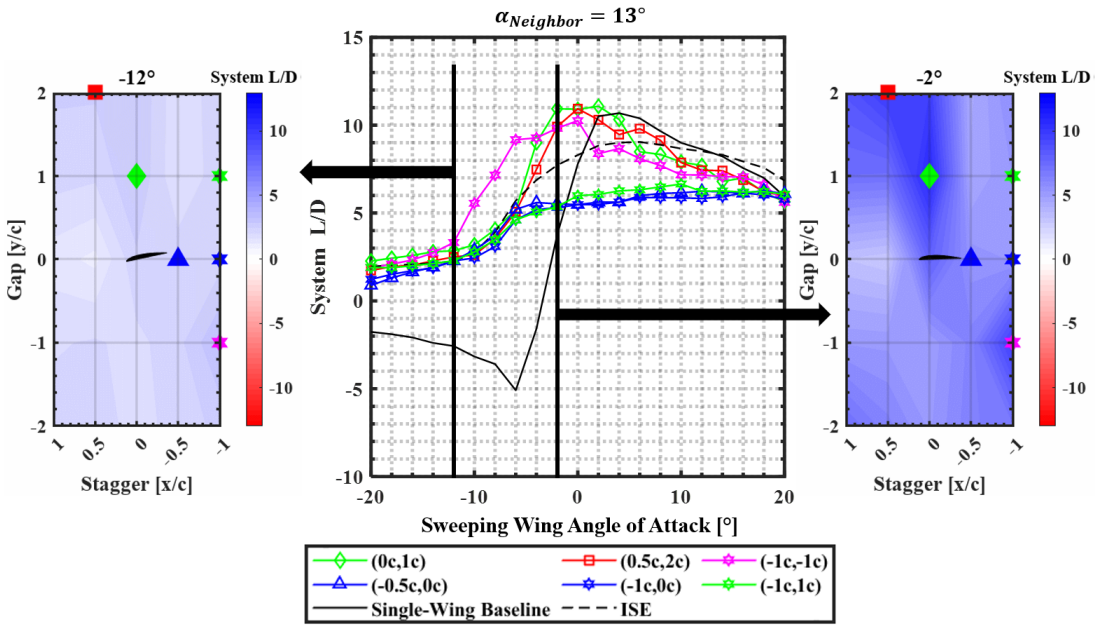

Figure 4-8 System L/D of various two-wing configurations as Sweeping Wing sweeps and Neighbor Wing is fixed at 13°

Increasing $\propto_{Neighbor}$ to 20° in Figure 4-9 causes a decrement of maximum L/D possibly due to the Neighbor Wing approaching stall. The L/D curve begins to plateau with no drastic maximum

L/D angle of attack. The Neighbor Wing at -20° introduces one new high performer along with two new low performance configurations resulting in the biggest change when the high and low performers were fairly constant at the previous Neighbor Wing angles of attack. Overall, low stagger and positive gap locations of the Neighbor Wing seem to result in optimal performance. Three configurations are constant throughout $\alpha_{Neighbor}$ = -10°, -3°, 8°, and 13° as being the poorest performing configurations. Two of those three are tandem wing configurations where the wings are horizontally coplanar.

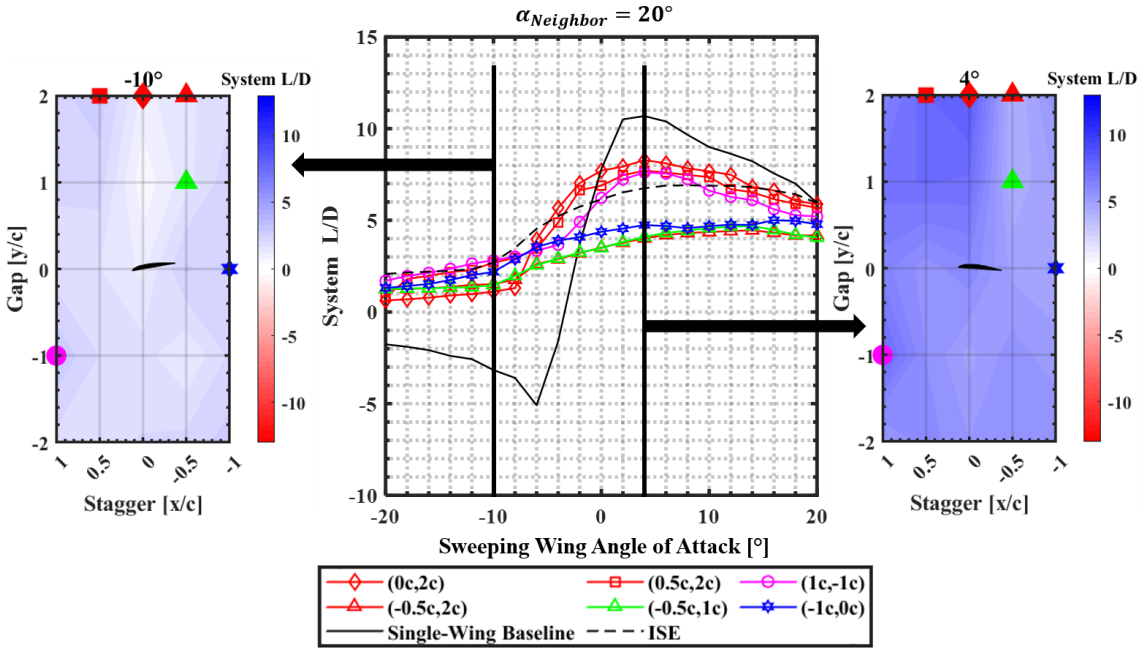

Figure 4-9 System L/D of various two-wing configurations as Sweeping Wing sweeps and Neighbor Wing is fixed at 20°

A major takeaway from the above breakdown of the highest and lowest performing configurations across different décalage is that a specific system L/D can be achieved in multiple different ways. The isosurface plots in Figure 4-10 represent a specific target system L/D selected based on the aircraft designer's requirements. The standalone baseline single wing has an L/D of 10.7 at 4° as shown in Figure 4-5 through Figure 4-9. Attempting to achieve approximately 80% of this efficiency with a system L/D of 8, the possible angle of attack configurations of a two-wing

system are displayed through the plots below. Increasing the target system L/D above 80% significantly diminishes the possible configurations, while decreasing below 80% allows most of the configurations to achieve the target. Therefore 80% is set as the highest target with a large variety of possible designs.

The isosurface plots indicate that 80% of the single-wing efficiency can be obtained at a selected stagger and gap locations but is heavily influenced by the angle of attack of combinations of the two wings. When the Neighbor Wing is at -3°, a system L/D of 8 could only be achieved in negative gap locations at a Sweeping Wing angle of attack range from to 0° to 10°. When the Neighbor Wing is at 8° however, the same efficiency can be achieved across almost the entire stagger and gap landscape, except for the tandem wing configurations.

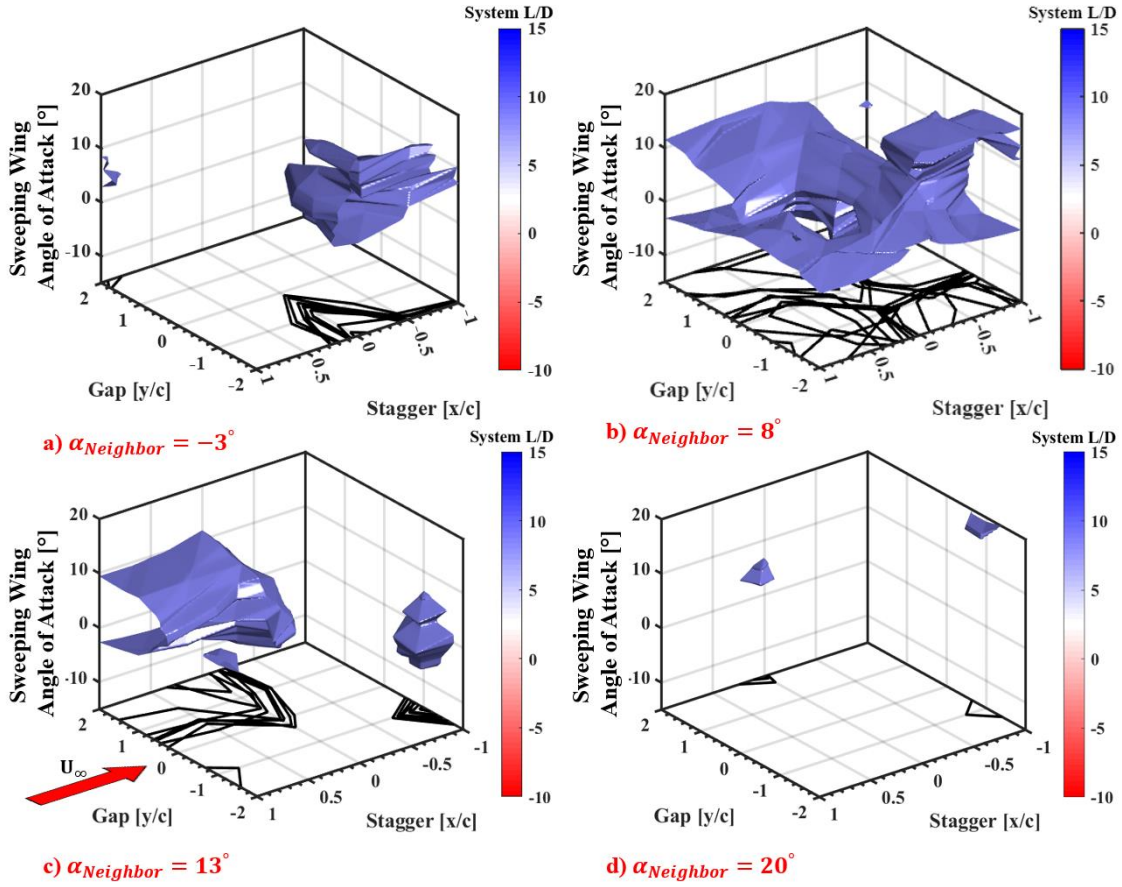

Figure 4-10 Stagger, Gap, and $\alpha_{Sweeping}$ combinations capable of achieving Target L/D of 8 with one Neighbor Wing at a) -3°, b) 8°, c) 13°, and d) 20°

In another effort to reduce all the variables involved in the testing, a mean contour is generated. Accounting for all the interaction effects and the influences of the wings on each other at all angles of attack, the overall mean system L/D was obtained at each stagger and gap distance from the Sweeping Wing as shown in Figure 4-11. As evidenced through the aforementioned figures, the tandem configurations have the lowest mean system L/D obtaining values below the baseline mean L/D of around 3.5. When compared to the mean Ideal System Efficiency that was calculated in Equation (16), there are no two-wing configurations that see a system L/D increment. The lowest decrements in system L/D occur at the top left and bottom right corner where the combined stagger and gap combination are large, and interactions are at a relative minimal. Also noticeable is the slight asymmetry which increases the importance of the direction of stagger and gap of the Neighbor Wing respective to the Sweeping Wing.

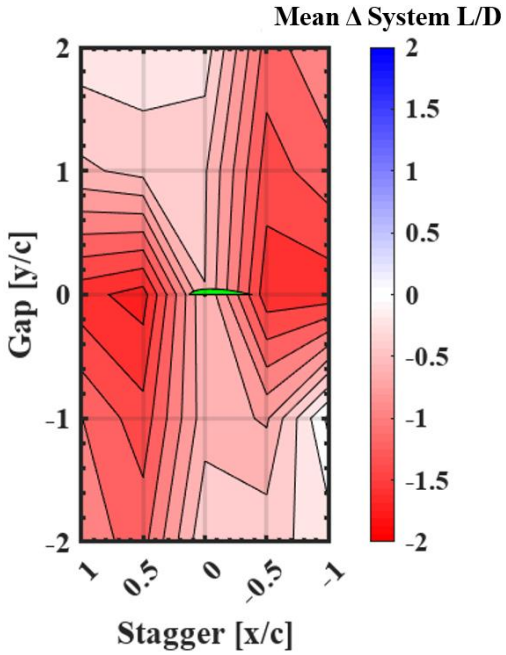

Figure 4-11 Difference in Mean System L/D from Mean ISE across all angles of attack at various stagger and gap locations to find Zone of Influence

4.3 FlightStream Simulation

4.3.1 Numerical Solver Validation

Before analyzing the flow field simulated by FlightStream and exploring any new configurations without wind tunnel data, the forces on each wing calculated by FlightStream is compared to the experiments. For this, the two extremes of two wings in a biplane and tandem configuration are used to validate the solver. Multiple different solver settings and meshes were explored in order to best match the experiments.

Figure 4-12 presents the comparison between the experimentally recorded lift coefficient and the FlightStream calculated lift coefficient on each wing for a 1 chord gap biplane where the bottom wing in red is the Sweeping Wing and the top blue wing is the Neighbor Wing fixed at 8°. FlightStream shows strong agreement with both wings with most of the deviation occurring towards the stall region of the Sweeping Wing as it predicts an early positive stall and no negative stall. To fairly compare the numerical simulations, the standard deviation bounds of the measured experimental lift coefficient are plotted as a grey shade with the experimental curves to represent the natural uncertainties and variations during experiments. For most of the cases, the standard deviation is relatively small with the wider bounds around positive and negative stall. FlightStream appears to be outside of these experimental uncertainties for both wings.

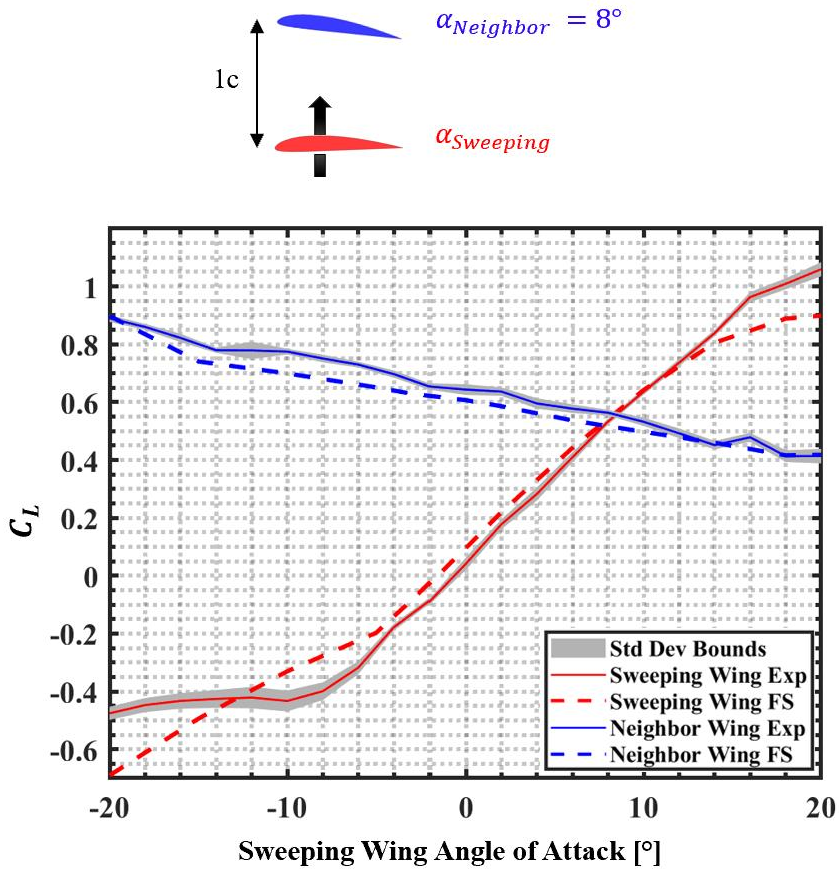

Figure 4-12 FlightStream Two-Wing Biplane validation with experimental results

FlightStream's lift coefficient measurements are compared with experiments in Figure 4-13 for a 1 chord stagger tandem with the front wing sweeping and the aft wing fixed at 8°. With direct disruption of the flow experienced by the downstream fixed wing, the exact values of $C_{L_{Neighbor}}$ are further apart than with the biplane configuration, but still show the same trend of a loss in lift as the Sweeping Wing increases angle of attack. An early positive stall and no negative stall is once more predicted by FlightStream on the Sweeping Wing. Once more the experimental standard deviation bounds are inserted to determine if FlightStream is within the uncertainty. The standard deviation of the measurements for the Neighbor Wing at high negative Sweeping Wing angles of

attack still do not intersect with FlightStream predictions, but this may be insight into turbulent unsteady flow at those specific conditions.

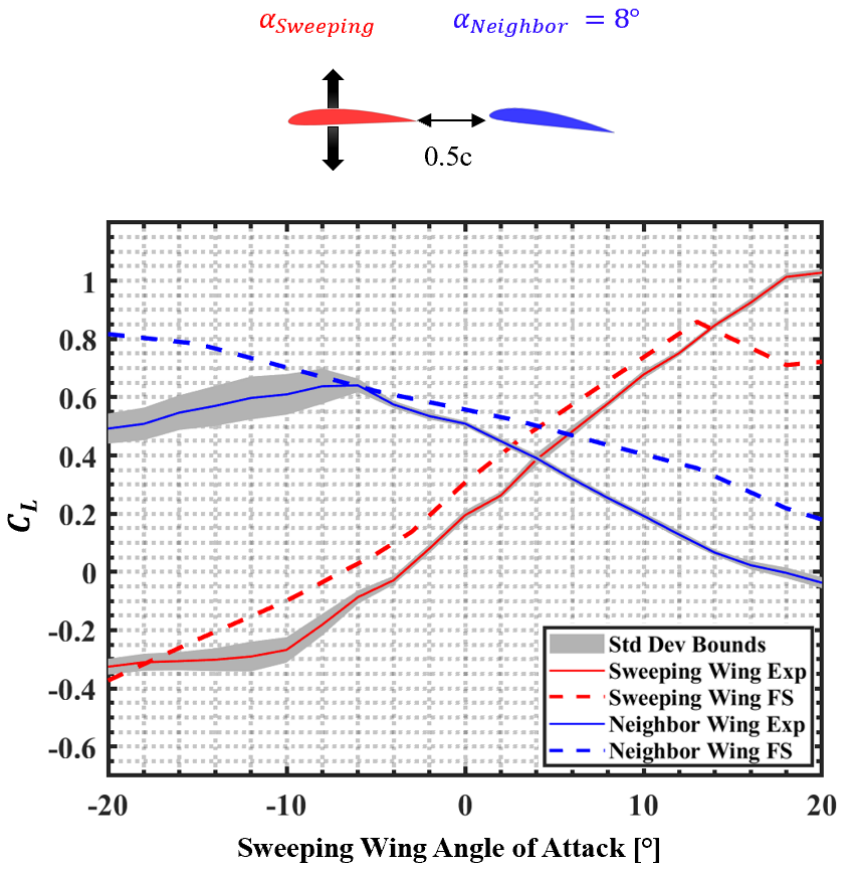

Figure 4-13 FlightStream Two-Wing Tandem validation with experimental results

4.3.2 Simulation Analysis

Overall, the FlightStream simulations exhibit reasonable agreement within the proximities validated, especially in the intermediate attached flow regime. The flow field surrounding the biplane and tandem configurations validated above can be extracted and analyzed. To collect more information about this instance, the coefficient of pressure (C_P) surface contour is extracted from FlightStream and plotted in Figure 4-14 and Figure 4-15, in two different views to observe the upper and lower surfaces. For a typical standalone wing, lift is directly proportional to the

difference in pressure of the upper and lower surface. The upper surface is referred to as the "suction side" and experiences low pressure, meanwhile the lower surface has a high pressure region leading to it being called the "pressure side". Streamlines are shown in one of the subplots to provide context regarding the general direction of the flow.

In Figure 4-12 of the biplane configuration, when both wings are at 8°, they individually converge on the same C_L. Theoretically, for both wings to generate the same C_L, the pressure difference between the upper and lower surfaces of the wing must be identical. However, the pressure contours on the upper surface are predicted by FlightStream differ among the wings as displayed in Figure 4-14a. The top wing shows a deeper blue, indicating a lower pressure compared to the bottom wing. At this gap spacing of 1c G, it is likely that the pressure side on the top wing is affected by the low pressure on the suction side of the bottom wing. This is evident by looking at the C_P on the lower surface of the top wing which is only small magnitude when on the bottom wing it is around a magnitude of 0.2.

In the tandem configuration, there is also a convergence of the same C_L produced by both wings, expect it is at $\alpha_{Sweeping} = 4°$ and $\alpha_{Neighbor} = 8°$. Although it was assumed that the C_P contours would display similar results of the same C_P distribution among the wings when lift coefficient converged, Figure 4-15 instead shows both tandem wings at 8°. This illustration is used to observe why the two wings generate different lift magnitudes at the same angle of attack. The aft wing experiences lower pressure on the upper surface due to the influence of the upstream wing's wake, as indicated by the generated streamlines. In fact, the lower surface of the aft wing produces some low pressure as well decreasing the pressure difference further. This is most likely directly responsible for the decrease in lift as observed in the individual wing force breakdown.

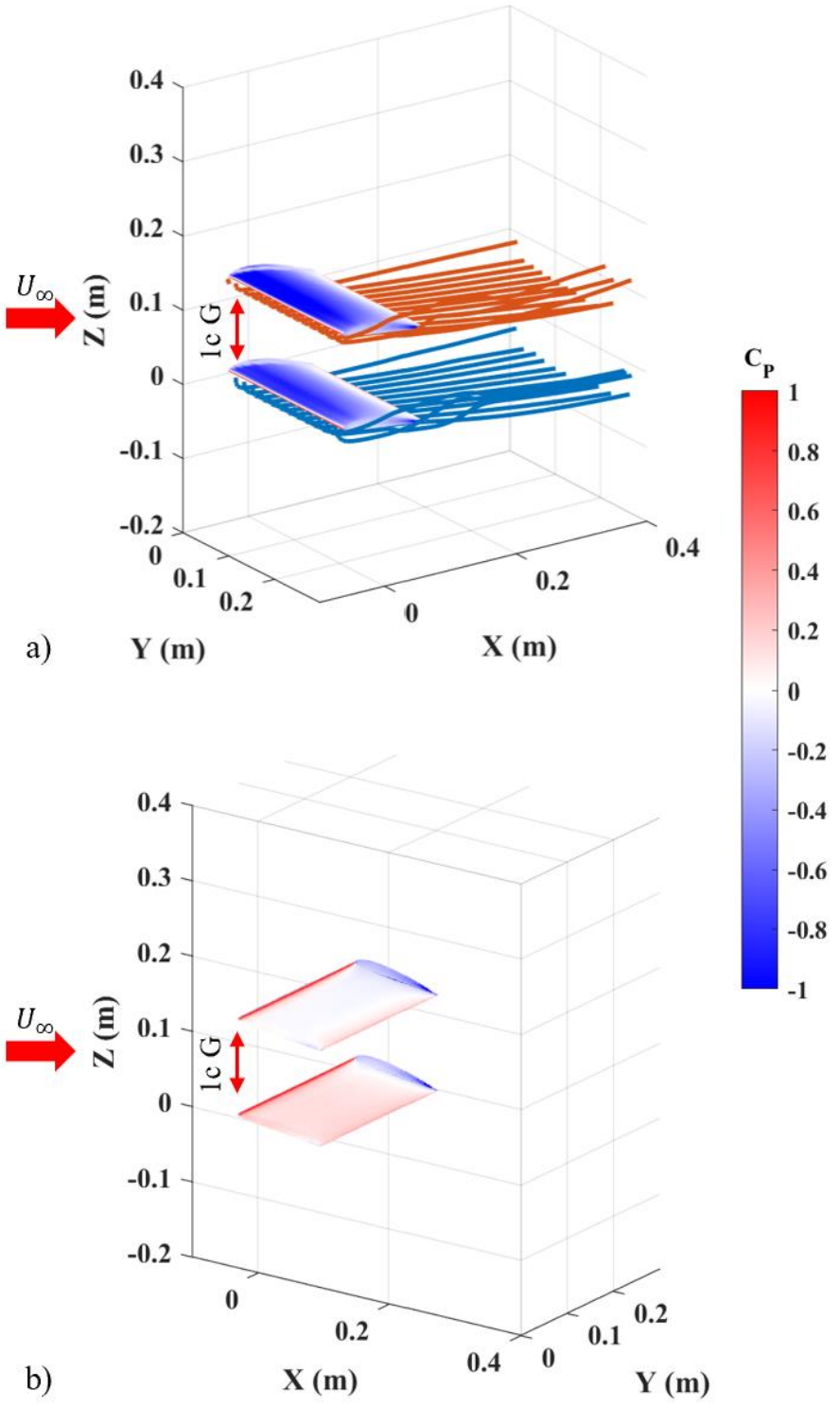

Figure 4-14 C_P surface contour a) Isometric Top with streamlines and b) Isometric Bottom view of two-wing biplane configuration with both wings at 8°

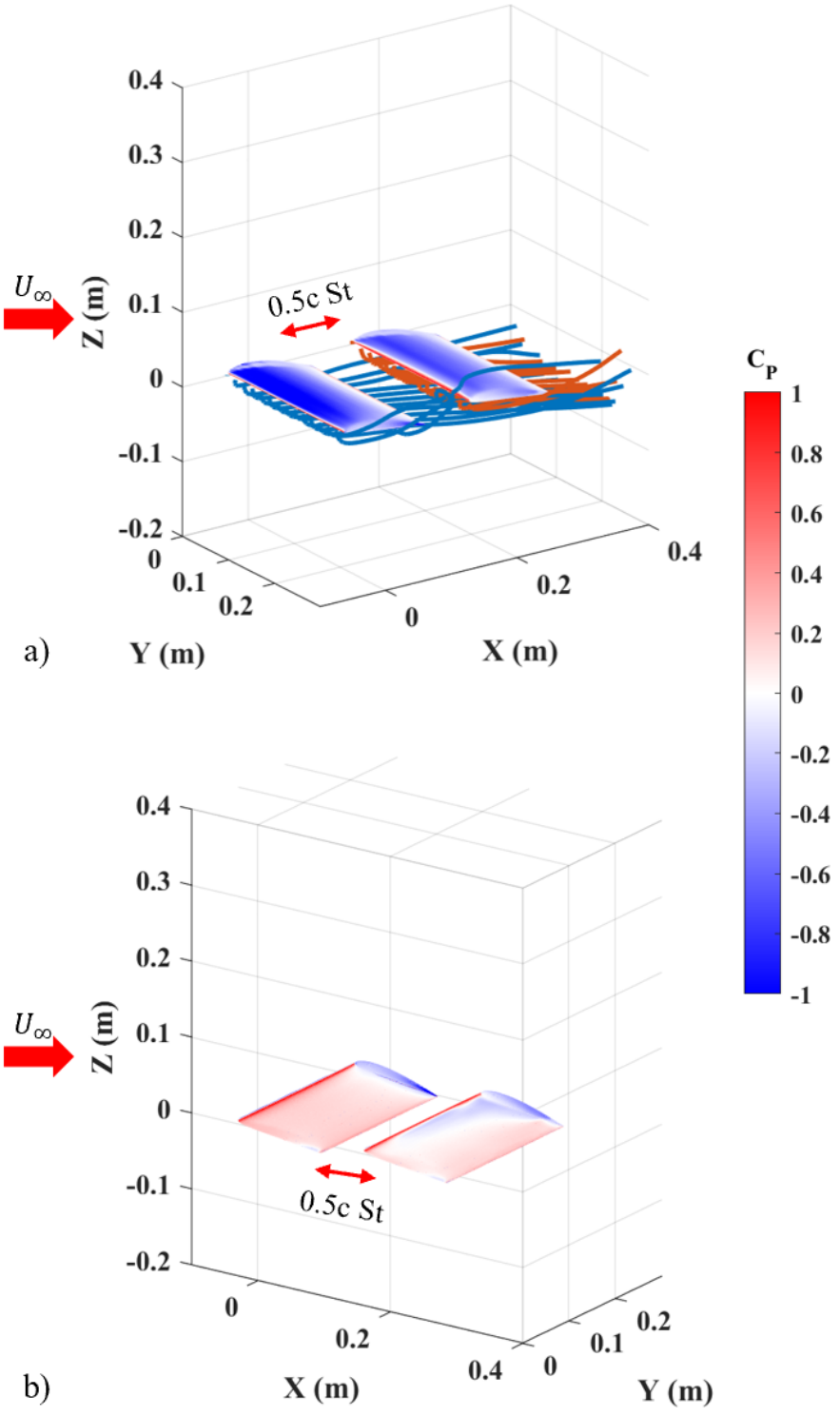

Figure 4-15 C_P surface contour a) Isometric Top with streamlines and b) Isometric Bottom view of two-wing tandem configuration with both wings at 8°

CHAPTER 5

THREE-WING INTERACTION RESULTS

A third identical Clark Y wing is added to the study to observe how the interactions between two wings are affected by the presence of a third wing in close proximity. Instead of a single secondary wing moving around the Sweeping Wing, in this study a two-wing group in either biplane or tandem configuration moves around the Sweeping Wing. The analysis is structured similarly to the two-wing study, where the performance of the individual Sweeping Wing and the Two-Wing Group is analyzed, along with a system analysis of all three wings combined. Additionally, FlightStream validations are included with flow field information of the validation cases extracted for further analysis.

5.1 Individual Wing Performance

In the reference frame of the Sweeping Wing, changes in lift coefficient are studied when a two-wing biplane group is placed in close proximity to it. Figure 5-1 shows the measured lift coefficient of the Sweeping Wing, from which the lift coefficient of the Single-Wing Baseline is subtracted, at different angles of attack. Again, the red color represents decreases relative to the standalone Single-Wing Baseline, while blue indicates an increase. The Sweeping Wing mostly experiences decrements with the introduction of the Biplane Group, especially when the Biplane Group is upstream. The Sweeping Wing is less affected by the Biplane Group when the two biplane wings are downstream of the Sweeping Wing.

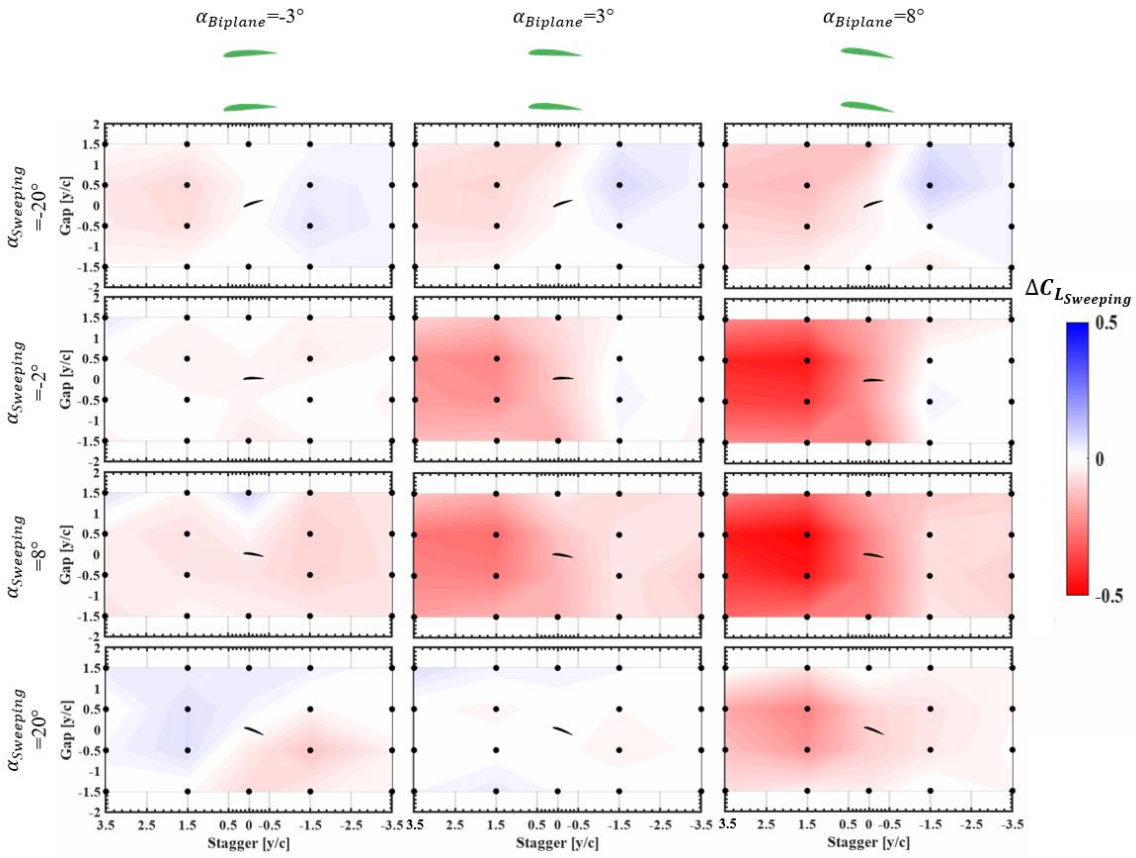

Figure 5-1 Contour array of Sweeping Wing lift coefficient difference from Single-Wing Baseline at different décalage with Biplane Group

Analysis of the deviation in the Biplane Group with the presence of a third Sweeping Wing, relative to an isolated Biplane Group, is plotted in Figure 5-2. As mentioned in Chapter 3, an expected biplane baseline is determined from the two-wing study and used for the three-wing and four-wing studies. Just as in Figure 5-1, the contour array predominantly shows decreases in the Biplane Group, with the most pronounced decreases occurring when the wing(s) under consideration are downstream of another wing. The contours on the top row when $\alpha_{Sweeping} = -20°$ does have locations where the Biplane Group experiences an increment in lift despite being downstream of the Sweeping Wing. The downstream locations overall exhibit the largest increment at low angle of attack and the largest decrements at high angle of attack, possibly emphasizing the effects of downwash on the performance of the aft wings.

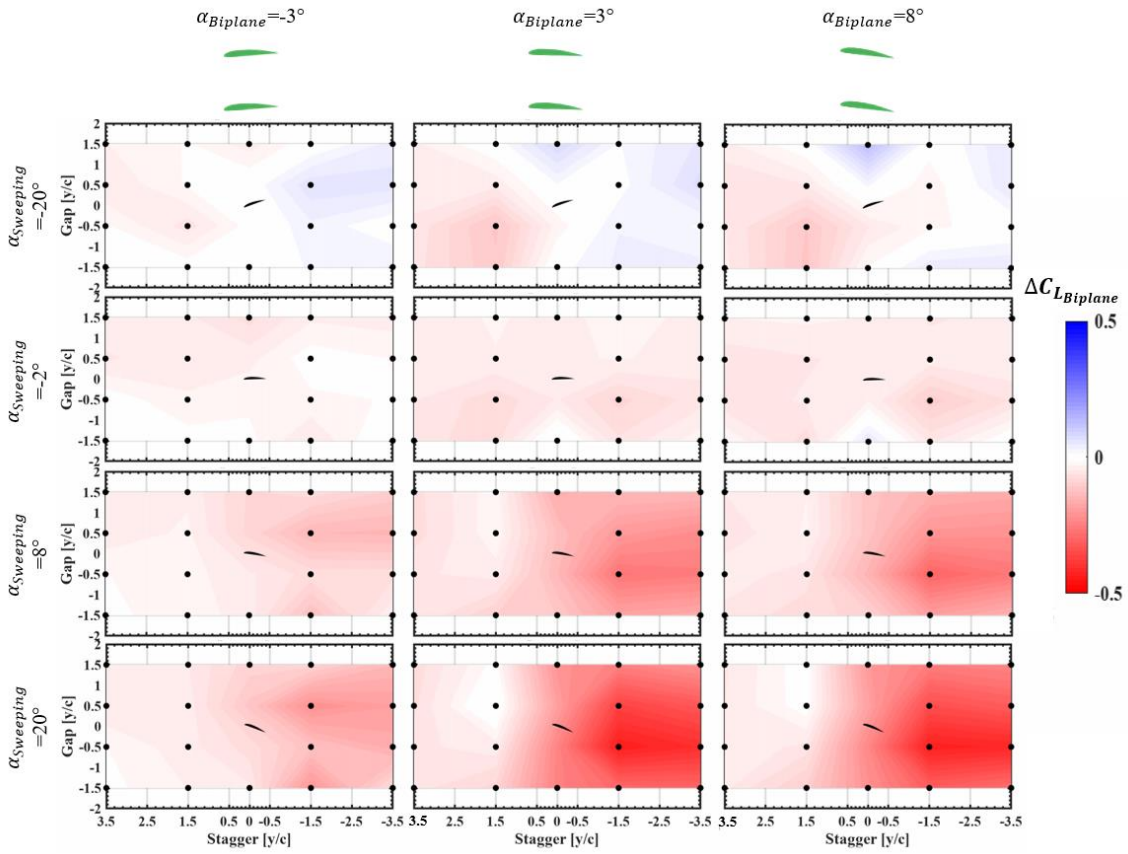

Figure 5-2 Contour array of Biplane Group lift coefficient difference from Biplane Baseline at different décalage with Biplane Group

The wing interaction with the two-wing tandem group can be analyzed in a manner identical to the biplane analysis performed above. The effect of the Tandem Group on the Sweeping Wing's C_L is plotted is depicted through a contour array at different Sweeping Wing and Tandem Group angle of attack combinations in Figure 5-3. When all three wings are in the intermediate attached flow regime, they produce contours that are entirely indicative of a decrease from the baseline, as seen by $\alpha_{Sweeping} = -2°, 8°$ and $\alpha_{Tandem} = 3°, 8°$. However, increments can be observed in the lift coefficient of the Sweeping Wing despite the presence of wings upstream when $\alpha_{Sweeping} = 20°$. This phenomenon is attributed to the "delay" in stall, as induced angle of attack is lower than the assumed $\alpha_{Sweeping}$ because of the Tandem Group's wake.

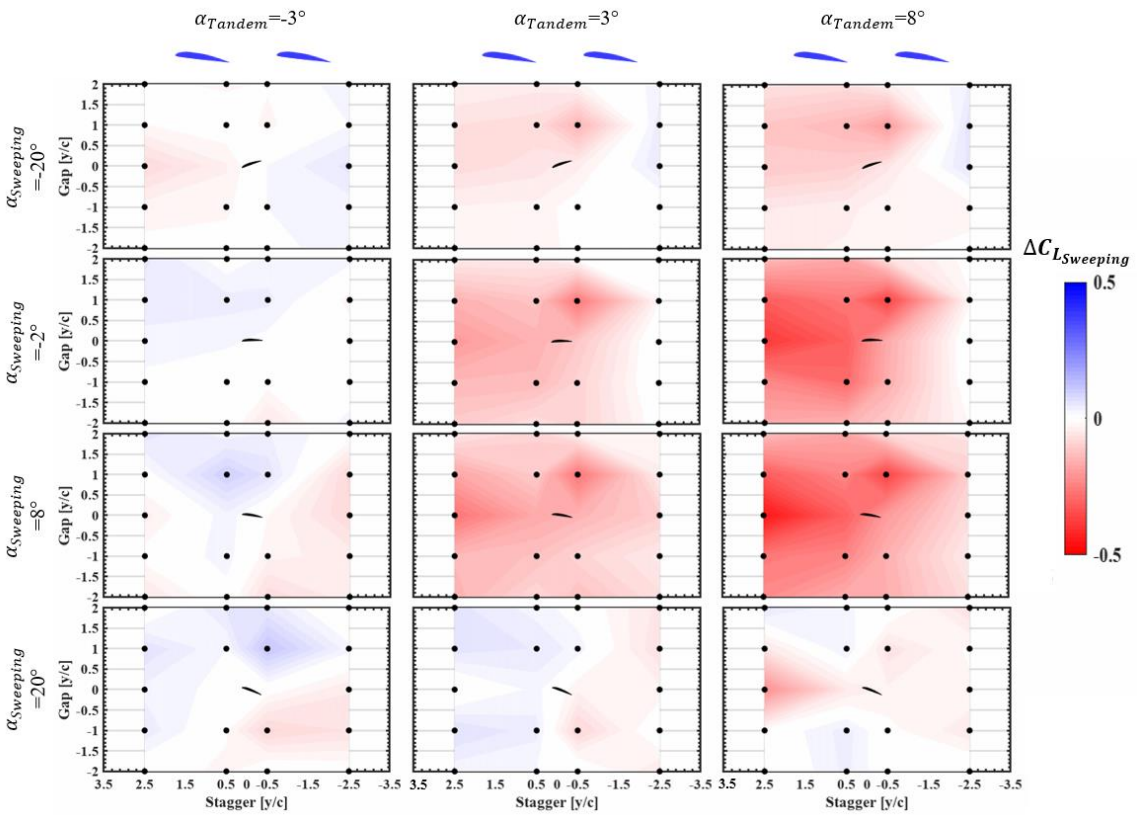

Figure 5-3 Contour array of Sweeping Wing lift coefficient difference from Single-Wing Baseline at different décalage with Tandem Group

The contours in Figure 5-4 quantify the effect that the Sweeping Wing has on the Tandem Group. Again, the performance is normalized by subtracting the baseline of a two-wing tandem system where both wings are at the same angle of attack. In the two wing studies, the Tandem Group appeared to suffer the largest decrements, but the addition of a third wing seems to be beneficial. Instances of increase occur around a stagger of 0.5c, which indicates that one of the wings within the tandem group is in a biplane configuration with the Sweeping Wing. When the two wings are downstream at their $\alpha_{L=0}$ and the Sweeping Wing is in a negative angle of attack stall, this trend of increase is more dominant than a decrease. However, once the Sweeping Wing increases its angle of attack to produce positive lift, the tandem wings experience a decrement when downstream. In Figure 5-1 through Figure 5-3, all three wings at $\alpha_{L=0}$ show the smallest deviation from the baseline, but in the tandem wing case of Figure 5-4, this trend is taken to an extreme where

throughout the entire testing grid there are only a few instances of any visible change in the lift coefficient.

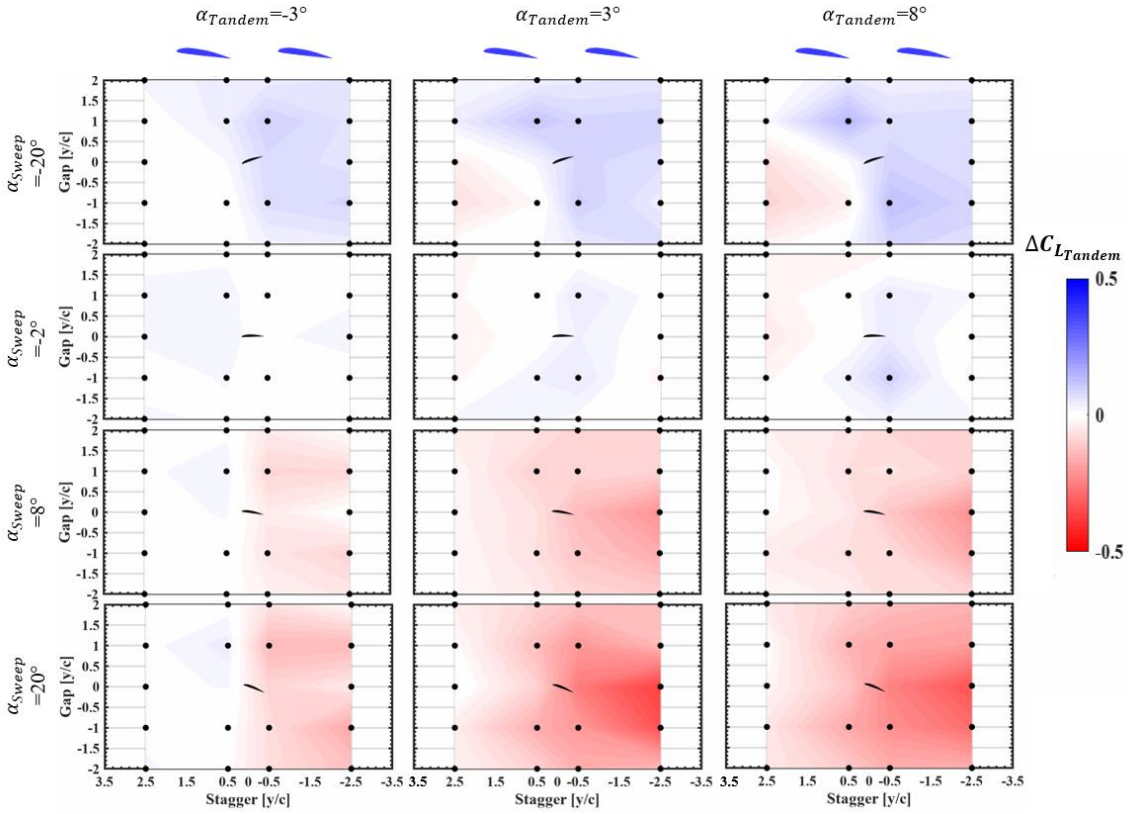

Figure 5-4 Contour array of Tandem Group lift coefficient difference from Tandem Baseline at different décalage with Tandem Group

For a comparison between the biplane and tandem configurations, dimension reduction is performed using the mean C_L contours in Figure 5-5 and Figure 5-6, which accounts for all the interaction effects and the influences of the wings on each other at all Sweeping Wing and Group angles of attack at each specific stagger and gap distance. Figure 5-5 subplots a) and b) compare the Sweeping Wing's performance when the biplane or tandem wing configuration is in close proximity. The impact of having a wing downstream of another is evident regardless of the configuration of the forward wing(s), but it does seem that the biplane configurations span a larger gap width. This is mostly due to the physical configuration having a larger gap footprint compared to the tandems, which are stagger dominant. In Figure 5-6 a) and b), the performance within the

two-wing configuration is evaluated. Again, only decrements from the baseline are present after taking the mean, irrespective of whether the two Neighbor Wings are in a biplane or tandem configuration. The trend of downstream locations suffering decrements is reflected in the mean once more. Comparing the two different two-wing groups reveals that the Biplane Group is slightly more sensitive to the presence of a third wing than the Tandem Group.

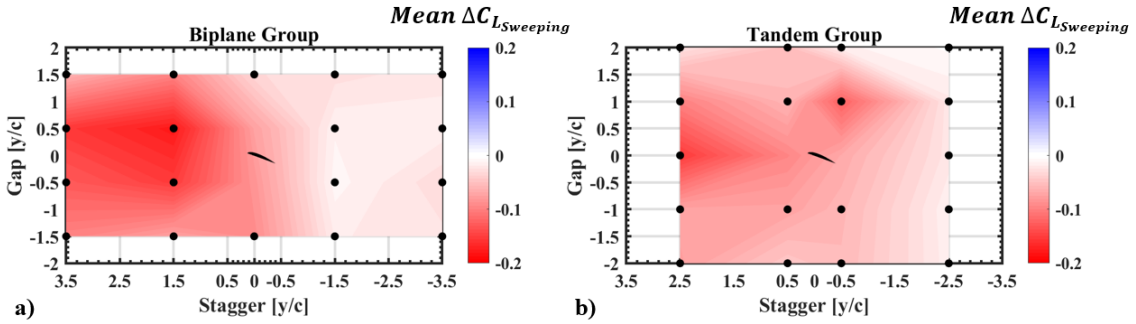

Figure 5-5 Contour of difference in Mean C_L of Sweeping Wing in proximity of a) Biplane Group or b) Tandem Group from Single-Wing Baseline across all angles of attack

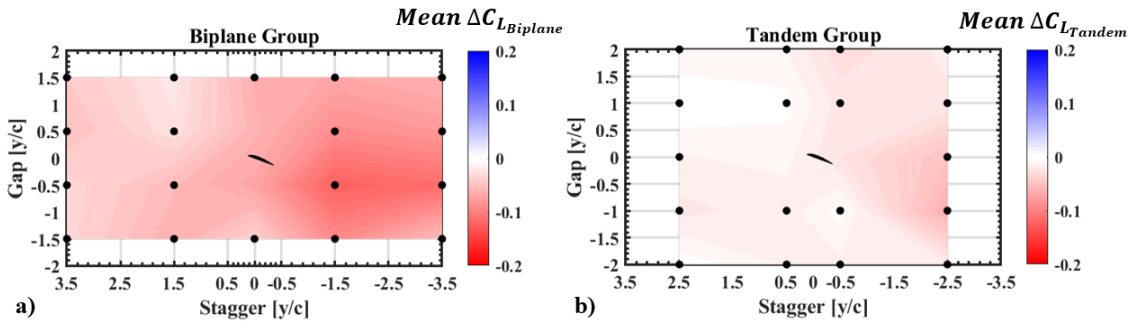

Figure 5-6 Contour of difference in Mean C_L of Two-Wing Group in proximity of a) Biplane Group or b) Tandem Group from Biplane/Tandem Baseline across all angles of attack

5.2 System Performance

The performance of the three wings combined as single system is now analyzed, similar to how the two-wing systems were examined. The figures below highlight the three highest and lowest configurations along with the Single-Wing Baseline and the ideal system efficiency (ISE) for a three-wing configuration at the respective $\alpha_{Neighbor}$. A system L/D contour is added to spatially mark the positions and show how those positions compare to the others.

When the Biplane Group is fixed at -3°, as seen in Figure 5-7, there is an overall increased sensitivity due to the $\alpha_{L=0}$, and as a result many configurations were withheld for this specific case. There seems to be a switch in performance as the Sweeping Wing crosses over the $\alpha_{L=0}$, as the some of the high performing cases at negative $\alpha_{Sweeping}$ become low performers, and the low performers become high performers. The high performing cases at positive $\alpha_{Sweeping}$ show areas of efficiency above the ISE, confirming the presence of some positive influence. A clear divide also appears between the high and low performing configurations at positive $\alpha_{Sweeping}$, whereas no such divide existed at negative angles.

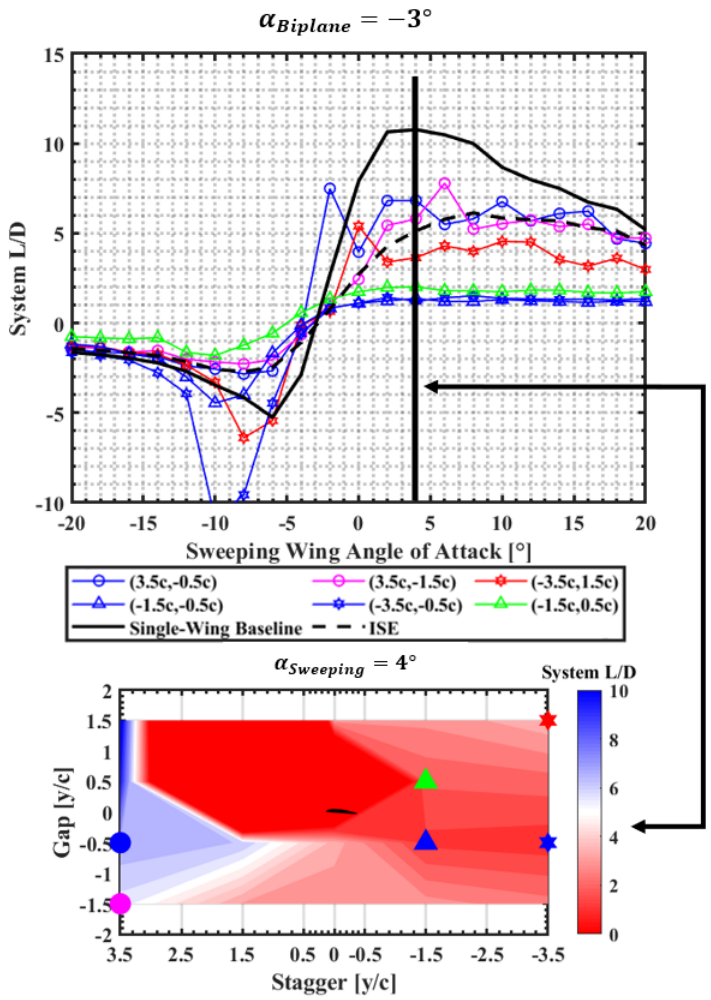

Figure 5-7 System L/D of various three-wing configurations as Sweeping Wing sweeps and Biplane Group is fixed at -3°

As the Biplane Group increases to a positive lift angle of attack of 3° different trends are observed. Immediately in Figure 5-8, the divide between high and low performing configurations is no longer visible. All the configurations stay close to the ISE at extreme negative and positive angles of attack, but do not achieve close to the maximum L/D of the single-wing or ISE.

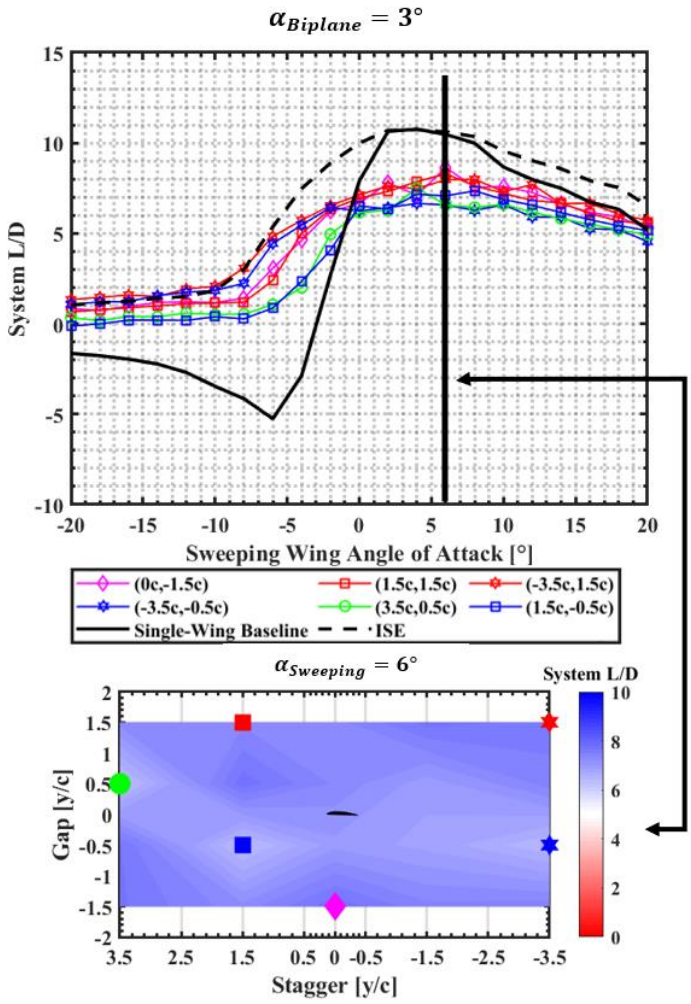

Figure 5-8 System L/D of various three-wing configurations as Sweeping Wing sweeps and Biplane Group is fixed at 3°

Figure 5-9 presents the results at the highest $\alpha_{Biplane}$ of 8°. As with the previous plot, at $\alpha_{Biplane} = 8°$ there is not a clear distinguish between the high performing cases and the lowest outside of a large gap around when the Sweeping Wing is at $\alpha_{L=0}$.

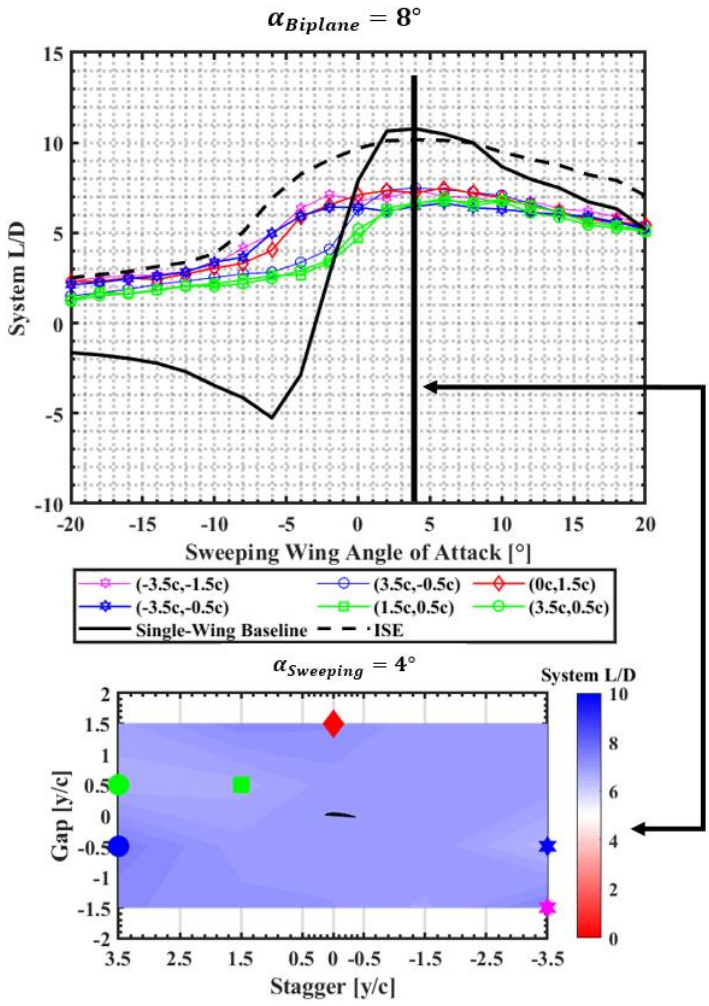

Figure 5-9 System L/D of various three-wing configurations as Sweeping Wing sweeps and Biplane Group is fixed at 8°

The Tandem Group contribution to the system is analyzed now. Beginning with Figure 5-10, where $\alpha_{Tandem} = -3°$, the high and low performing configurations follow each other and the ISE relatively closely until there is a divergence in the low performing cases as they experience a large decrement from the ISE. The highest system performing case is a direct three wing tandem where the Sweeping Wing is downstream of the other two wings at a fixed -3°. The two other high performing cases have the Tandem Group along a diagonal of 2.5c stagger, either 1c above or below the Sweeping Wing, creating a diagonal.

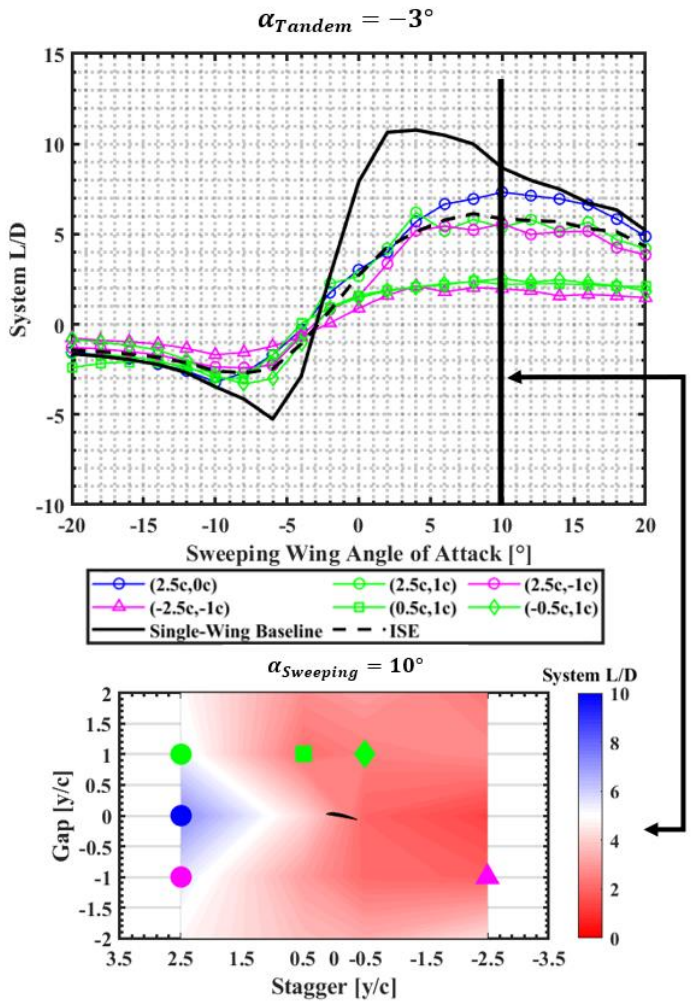

Figure 5-10 System L/D of various three-wing configurations as Sweeping Wing sweeps and Tandem Group is fixed at -3°

The Tandem Group is rotated to an angle of attack of 3° in Figure 5-11. As with the Biplane Group plots, once the group angle of attack is increased, the gap between the high and low performing configurations drastically decreases. However, there is a distinguishable spacing between all the individual lines. The high performer three wing tandem configuration from Figure 5-10 now becomes one of the low performers, as three wing tandem orientations struggle. The trend of a transition to mostly positive L/D recurs when the fixed wings move to a positive angle of attack.

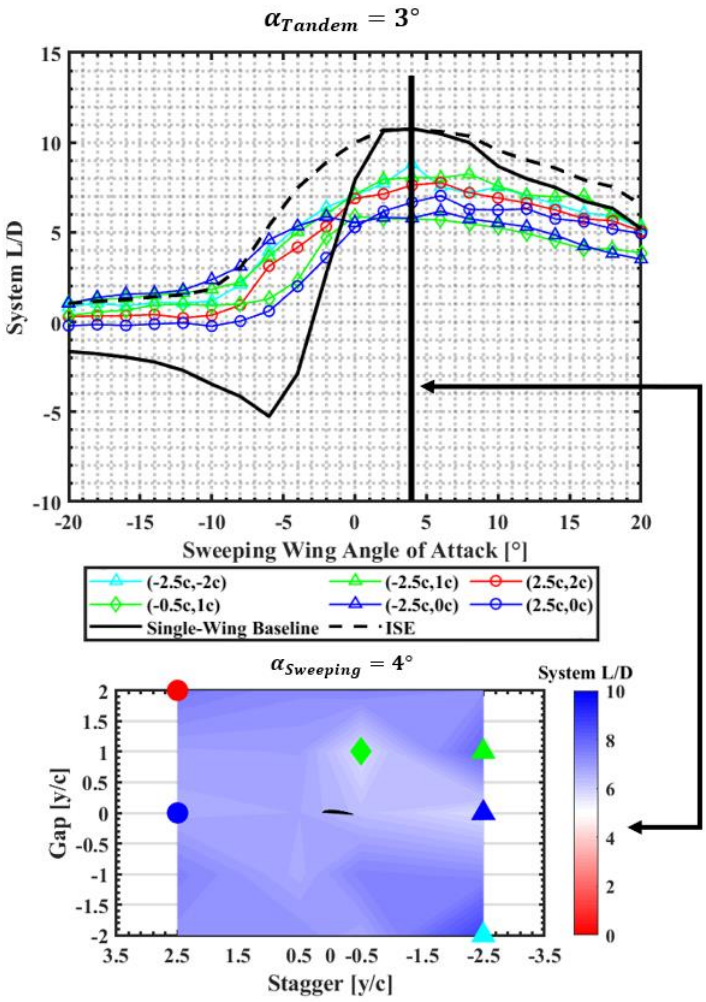

Figure 5-11 System L/D of various three-wing configurations as Sweeping Wing sweeps and Tandem Group is fixed at 3°

The highest Tandem Group angle of attack analysis is shown in Figure 5-12. The two complete three wings in tandem configurations continue as low performers. At this α_{Tandem}, all the configurations collapse further with minimal differences in L/D. A drop in the maximum L/Ds achieved by the configurations occurs when compared to the previous $\alpha_{Neighbor}$ set along with slightly more of a plateau effect on the curve across the angle of attack sweep.

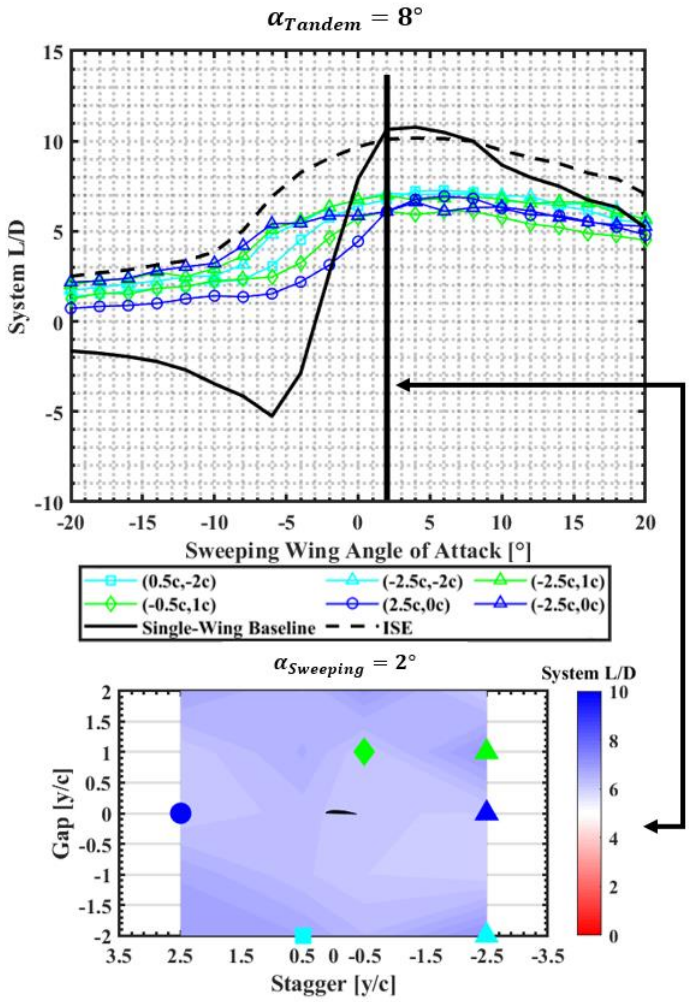

Figure 5-12 System L/D of various three-wing configurations as Sweeping Wing sweeps and Tandem Group is fixed at 8°

Isosurface plots return as a tool to effectively determine all experimentally possible combinations of gap, stagger, $\alpha_{Sweeping}$, and $\alpha_{Neighbor}$. A target L/D was set to 7 in the case of three wing due to almost no configurations being able to achieve a target L/D of 8 that was set for the two-wing isosurface plots in Figure 4-10. Unlike the two-wing isosurface plots, for the three-wing the largest number of capable configurations occur when the two Neighbor Wings are fixed at an angle of attack of 3° with a reduction of the landscape at 8°. As the number of wings increase from two to three, the magnitude of the system L/D reduces, but a feasible target can be achieved at a lower $\alpha_{Neighbor}$ with still a significant number of different ways to achieve that target.

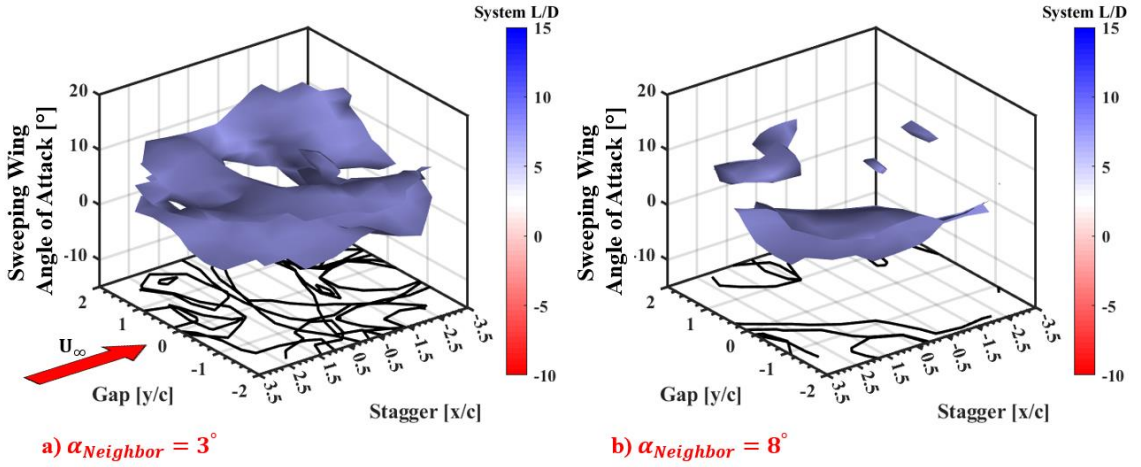

Figure 5-13 Stagger, Gap, and $\alpha_{Sweeping}$ combinations capable of achieving Target L/D of 7 with two Neighbor Wing at a) 3° and b) 8°

5.3 FlightStream Simulation

5.3.1 Numerical Solver Validation

The FlightStream simulations are once again validated with experimental data to confirm their accuracy when a third wing is added. The two extremes of three wings stacked vertically like a triplane, and then horizontally like a three-wing tandem, are used as the comparison cases. Figure 5-14 compares the three-wing vertical stacked with the top two wings fixed at an angle of attack and the bottom wing sweeping. FlightStream matches the trends observed in experiments acceptably. The struggle in predicting stalls on the Sweeping Wing persists, as seen with the two-wing FlightStream results. Surprisingly, there is good agreement between experimental and numerical results for the middle wing, while the top fixed wing is off by a constant value 0.1 to 0.2 C_L across the entire sweep. As done previously, the standard deviation of the experimental lift coefficient is displayed through the grey shading. For the most part, the standard deviation is small with the largest bounds appearing on the top Neighbor Wing's lift coefficient, which also is where FlightStream sees the largest disagreement.

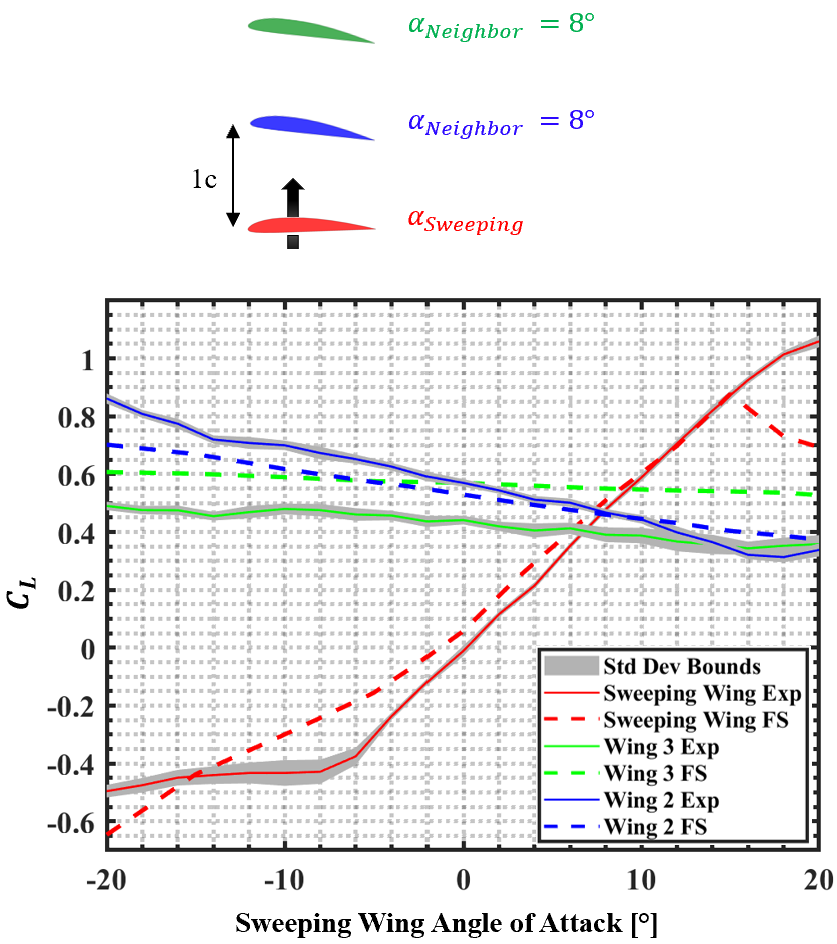

Figure 5-14 FlightStream Three-Wing vertical stacked validation with experimental results

One of the three-wing tandem has the front two wings fixed at an angle of attack with the rear wing sweeping. FlightStream shows a constant offset on all wings of around a C_L of 0.1 from the experimental data as displayed in Figure 5-15. Interestingly, FlightStream does not predict an early stall on the Sweeping Wing for the tandem configuration and matches with experimental as both show no signs of stall even at 20°. The standard deviation analysis continues to show this FlightStream offset from experiments is not within the experimental uncertainty bounds and may require further improvement on the simulation accuracy for these complex wake dominated configurations.

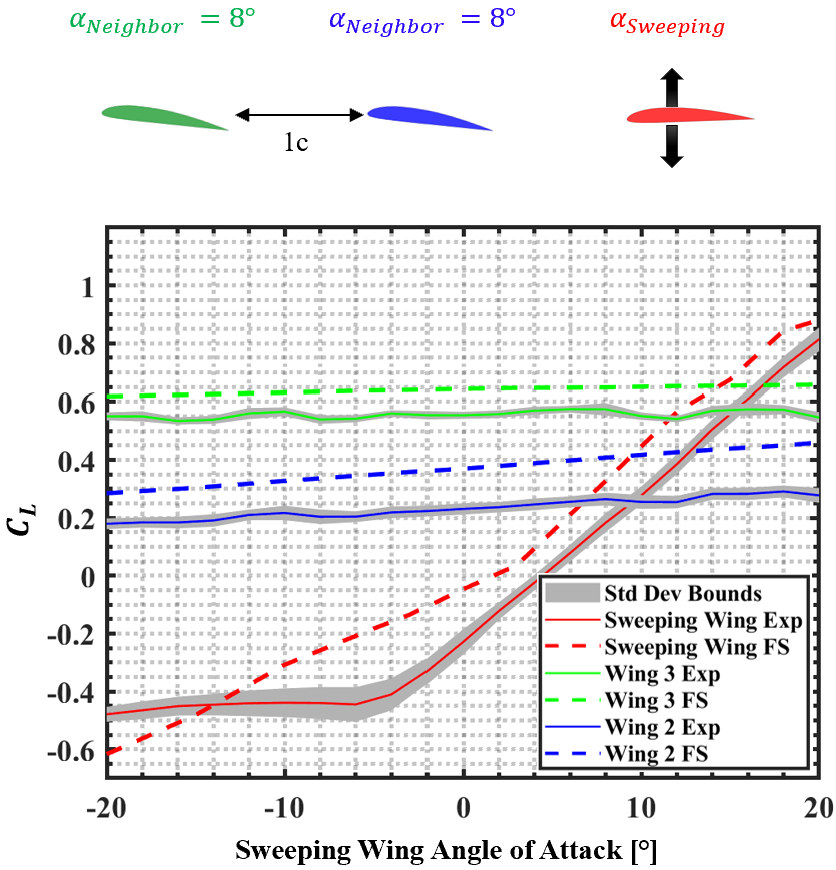

Figure 5-15 FlightStream Three-Wing Tandem validation with experimental results

5.3.2 Simulation Analysis

The validation cases will be used as cases to further analysis through coefficient of pressure surface contours and streamlines due to their opposite arrangements and performance as high or low configurations. The same two base configurations analyzed in the two-wing study are selected to observe any changes caused by the addition of a third wing to the biplane or tandem configuration.

The case where all three vertically stacked wings are at an 8° angle has been chosen for investigation, owing to the similarity in the lift coefficient (C_L) exhibited by the bottom and middle wings, as depicted in Figure 5-14. However, there exists a disagreement between experimental

findings and FlightStream predictions concerning the top wing's performance. The experimental data suggest a slightly lower lift for the top wing compared to the other two, while FlightStream predicts the top wing to generate marginally more lift. As evidenced in Figure 5-16, the intermingling of one wing's low-pressure region with another's high-pressure region persists as a trend. This natural inclination towards achieving pressure equilibrium results in the top wing having the highest low-pressure magnitude and the bottom wing having the highest high-pressure magnitude.

For three wings in tandem set at 8°, each wing generates a different lift force. In both experiments and FlightStream, the general trend observed is a progressive decrease in lift generation from the front wing to the aft wing. The streamlines depicted in Figure 5-17a illustrate how the streamlines from each wing intermingle and expand as the wakes extend downstream. As the wakes become more dominant, they exert a strong effect on the lower surfaces of the downstream wings, leading to a decrease in their high pressure. This, in turn, reduces the overall pressure difference across the wings.

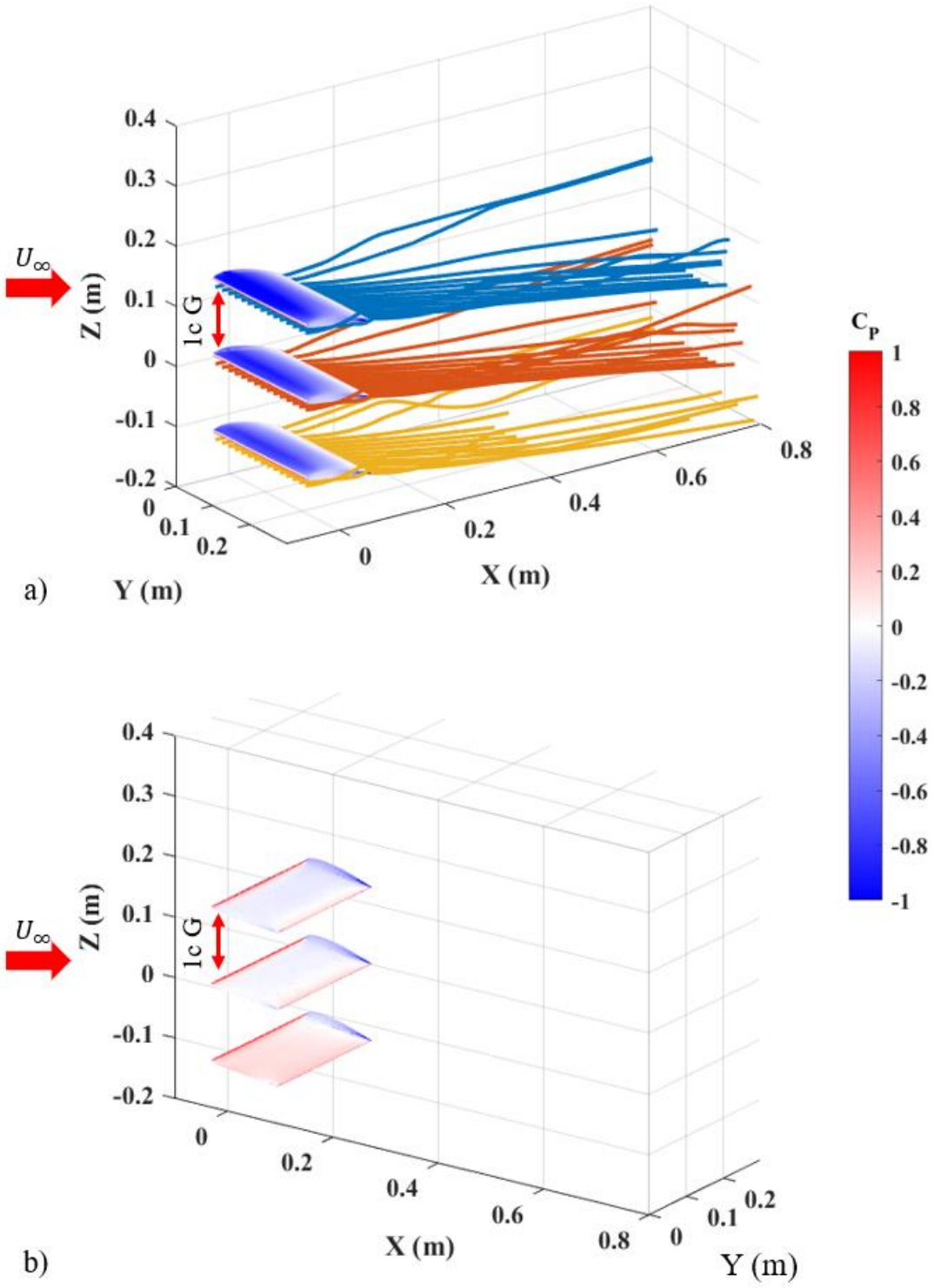

Figure 5-16 C_P surface contour a) Isometric and b) Top angled view of three-wing 1c G vertical stacked configuration with all wings at 8°

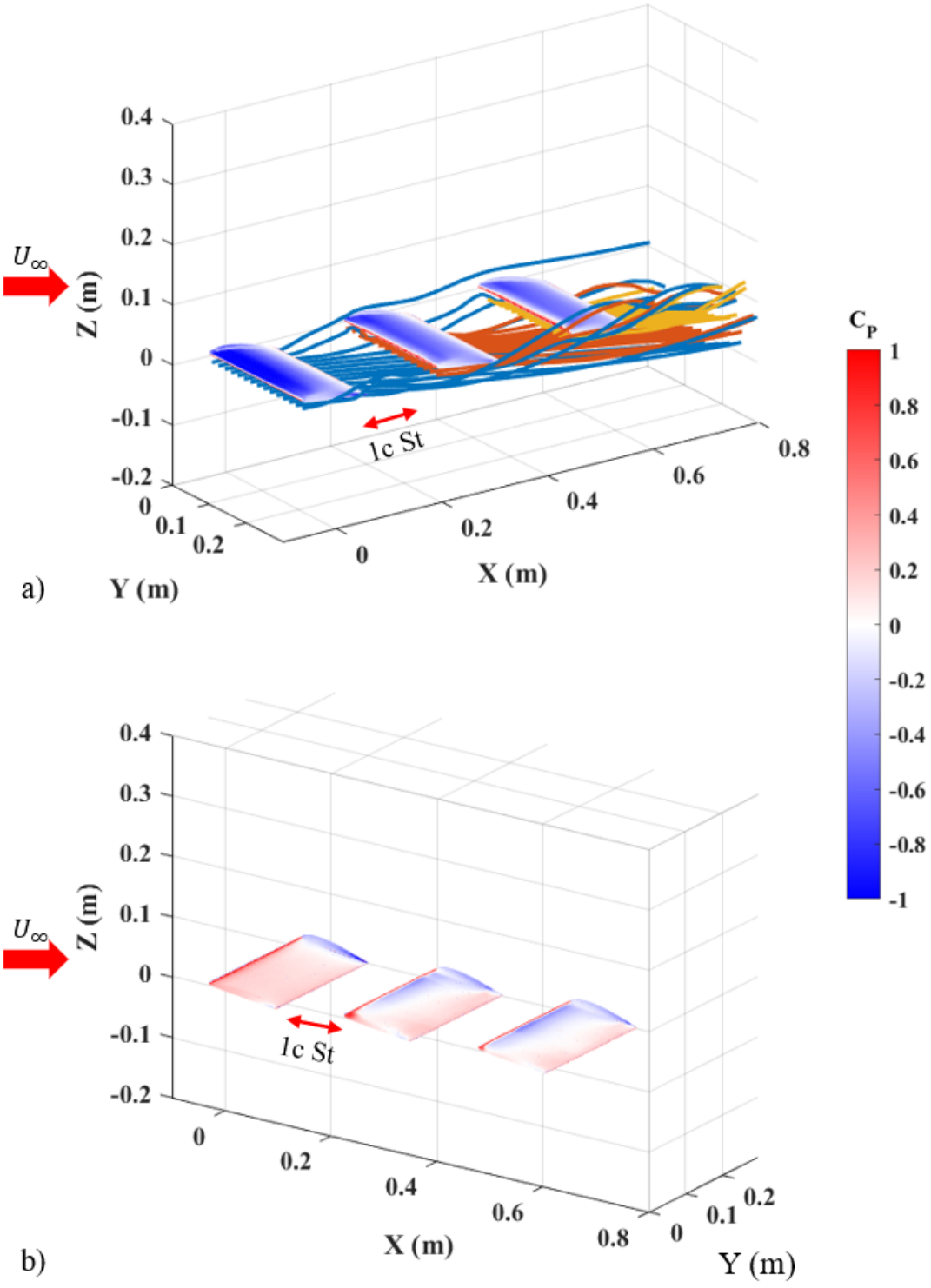

Figure 5-17 C_P surface contour a) Isometric and b) Top angled view of three-wing 1c St tandem configuration with all wings at 8°

CHAPTER 6

FOUR-WING INTERACTION RESULTS

With the improved reliability of FlightStream simulations, a reduced experimental test matrix was conducted with four identical wings in close proximity. The results from this study are presented in the following sections, using an analytical approach similar to those employed in the two-wing and three-wing studies. Furthermore, new four-wing configurations will be introduced as the study expands its scope to explore different arrangements without the need for wind tunnel experiments. FlightStream will be utilized to conduct system angle of attack sweeps, and information pertaining to total system forces and flow field will be extracted for deeper analysis. These configurations inch closer to the goal of the larger wing numbers targeted in a concept like distributed lift—a concept relatively unexplored in existing literature within the aircraft design space.

6.1 Individual Wing Performance

Due to the fewer testing points for the four-wing study, instead of contour plots, different wing positions will be referred to as four-wing biplane and tandem configurations rather than grid points are briefly described in the experimental setup chapter. The four-wing biplane configurations are when two Biplane Groups are placed within close proximity of each other, where one of the Biplane Groups includes the Sweeping Wing and will be referred to as the Sweeping Wing Group. The four-wing tandem configurations are in a similar manner, but there will be two Tandem Groups instead. A focused analysis is possible for the Sweeping Wing and the two-wing groups with comparisons to a Single-Wing Baseline and isolated biplane/tandem baseline to understand how these wings are affecting each other with the addition of a fourth fixed angle of attack Neighbor Wing.

Figure 6-1 displays the impact on the lift coefficient of the Sweeping Wing when it is placed in a biplane configuration with a Neighbor Wing, and the Biplane Group is at varying proximities. In other words, these four-wing configurations essentially consist of two Biplane Groups at

different proximity to each other. It is evident that when the Biplane Group is upstream of the Sweeping Wing, there is a change in the effective angle of attack, as the whole lift curve shifts to the right as $\alpha_{Biplane}$ is increased. When the Biplane Group is downstream of the Sweeping Wing, some deviation from the Single-Wing Baseline still occurs, which is attributed to the Neighbor Wing beneath it or may possibly be upwash from the Biplane Group back on to the upstream Sweeping Wing.

Shifting the reference frame to the Biplane Group in Figure 6-2, the impact of the Sweeping Wing and Neighbor Wing on the Biplane Group is illustrated. The distinct black lines portray the performance of an isolated Biplane Group at a fixed angle of attack obtained from the two-wing study. There is minimal deviation from their respective isolated biplane baselines when the group is positioned upstream from the Sweeping Wing. However, as the group is relocated downstream, there is an immediate decrease in lift generation, which remains relatively constant across a Sweeping Wing angle of attack range of -20° to approximately 5°. Once the Sweeping Wing begins to generate positive lift, a consistent decline in the Biplane Group's lift coefficient can be observed, likely due to flow separation.

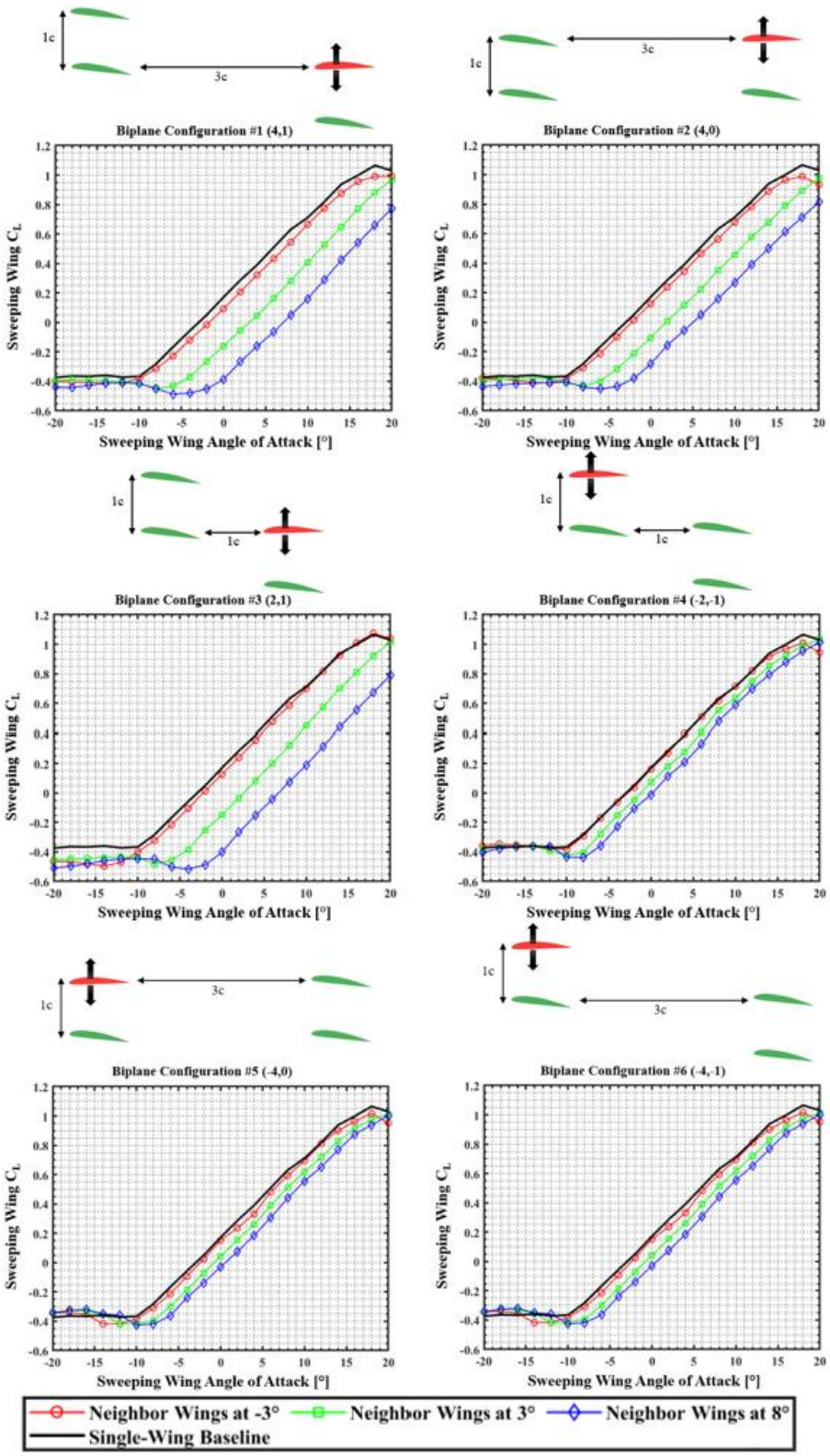

Figure 6-1 Sweeping Wing lift coefficient in various four-wing biplane configurations

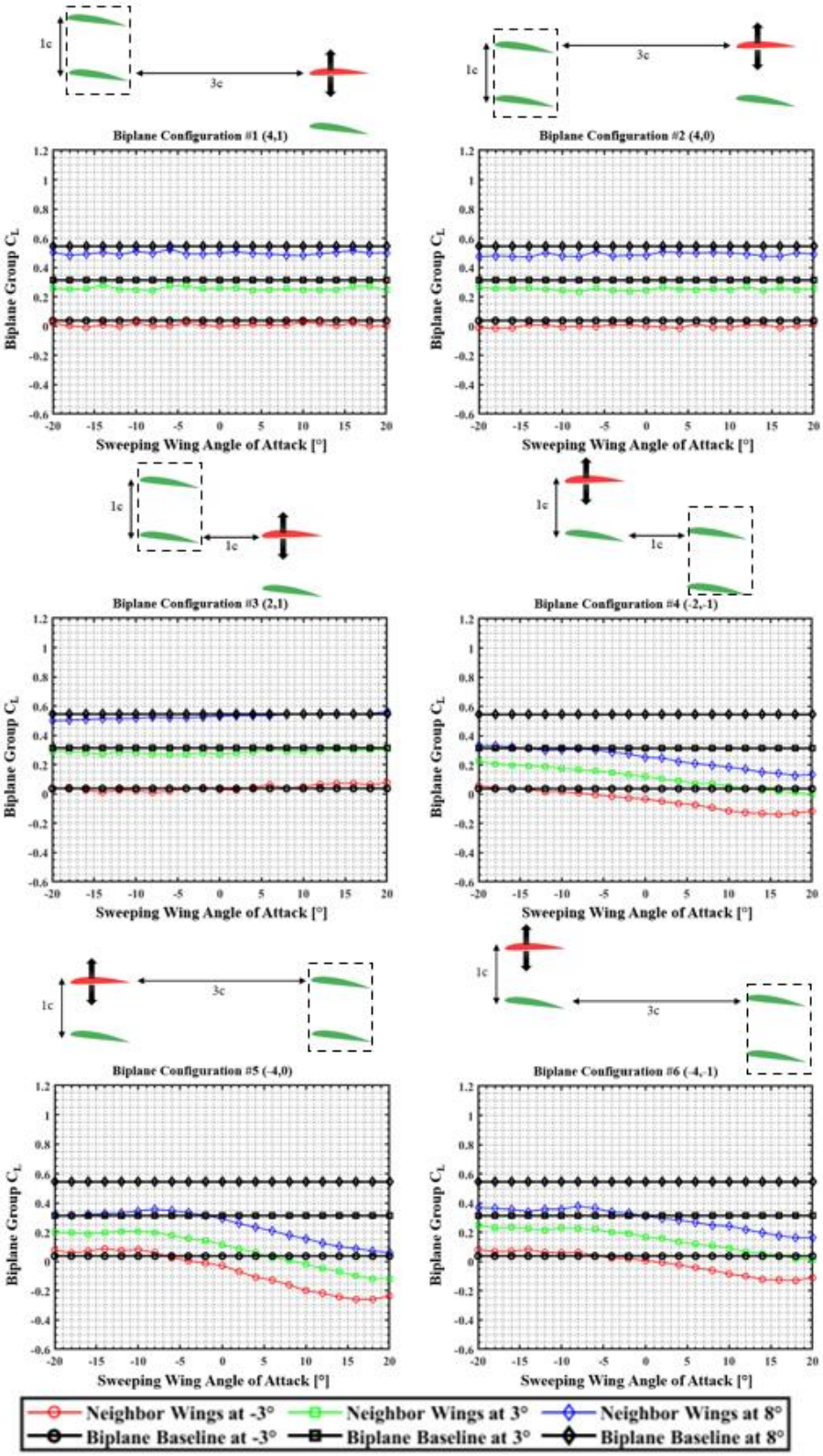

Figure 6-2 Biplane Group lift coefficient in various four-wing biplane configurations

Similar analysis is conducted for the four-wing configurations consisting of two Tandem Groups. Figure 6-3 displays the four configurations where the Tandem Group within the four-wing configuration is positioned above the Sweeping Wing. Figure 6-4 displays four configurations in which the Tandem Group is positioned below the Sweeping Wing. As observed in the four-wing biplane configurations, as soon as the fixed two-wing group transitions to downstream locations, the Sweeping Wing's performance aligns with that of the Single-Wing Baseline. The influence of gap distancing proves to be slightly more pronounced in these configurations. For instance, in Tandem Configurations #3 through #6, which are oriented with 0c St, the variation in gap (1c G or 2c G) does exhibit differences. A smaller gap induces a more significant change in the Sweeping Wing as α_{Tandem} varies.

The performance of the fixed Tandem Group is the focus of Figure 6-5 and Figure 6-6. The Tandem Group invariably experiences some deviation from the respective tandem baseline, but this deviation is magnified when the group is positioned below the Sweeping Wing, as shown in Figure 6-6. When $\alpha_{Sweeping}$ is positive, there is an overall decreasing trend in the Tandem Group lift coefficient. This decrease is more significant at lower gaps as seen in Tandem Configurations #5 and #7.

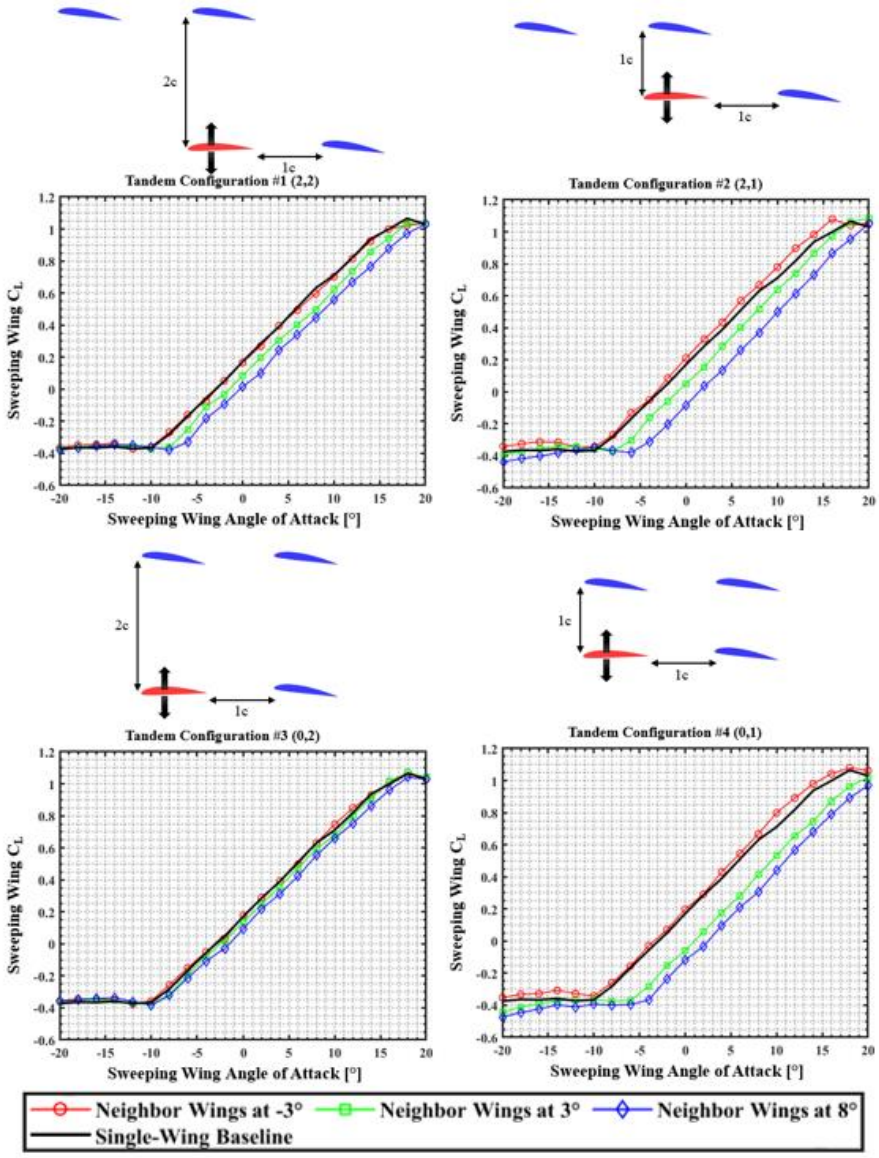

Figure 6-3 Sweeping Wing lift coefficient in various four-wing tandem configurations

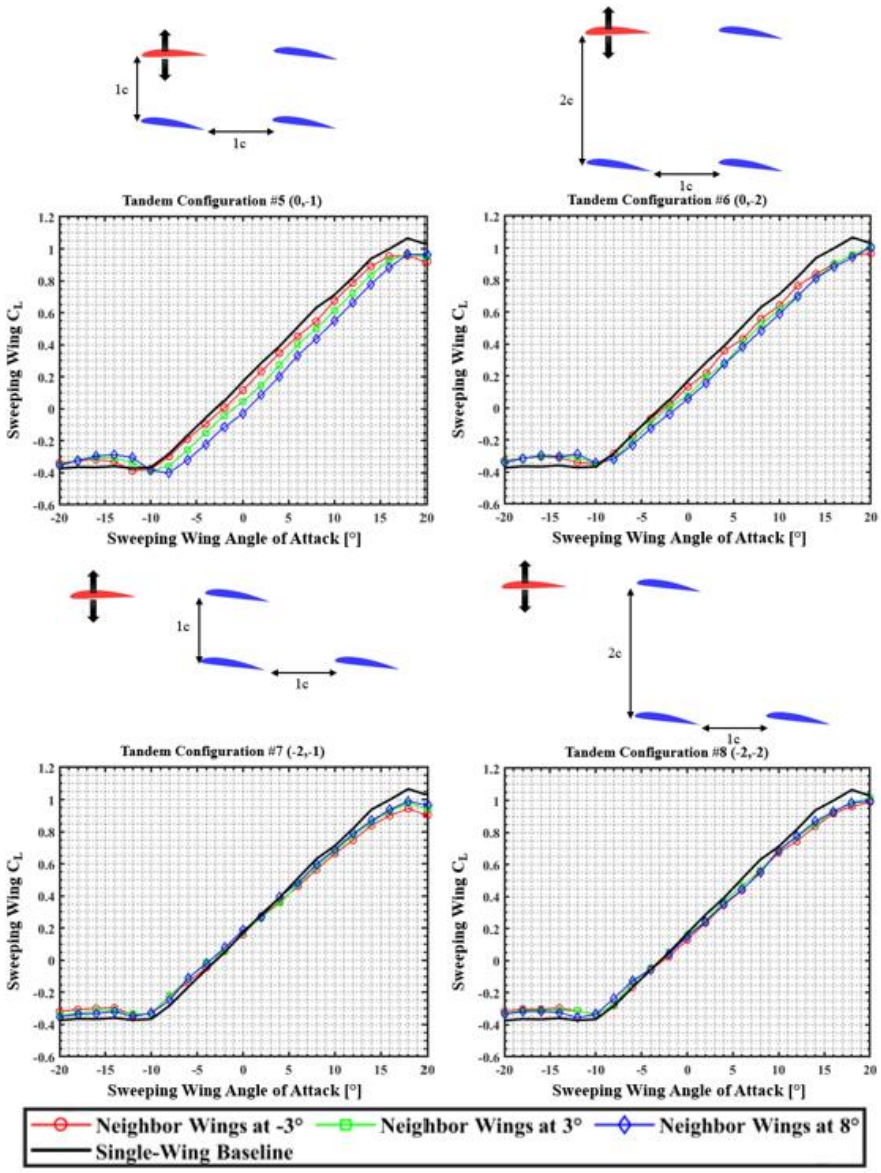

Figure 6-4 Sweeping Wing lift coefficient in various four-wing biplane configurations Cont.

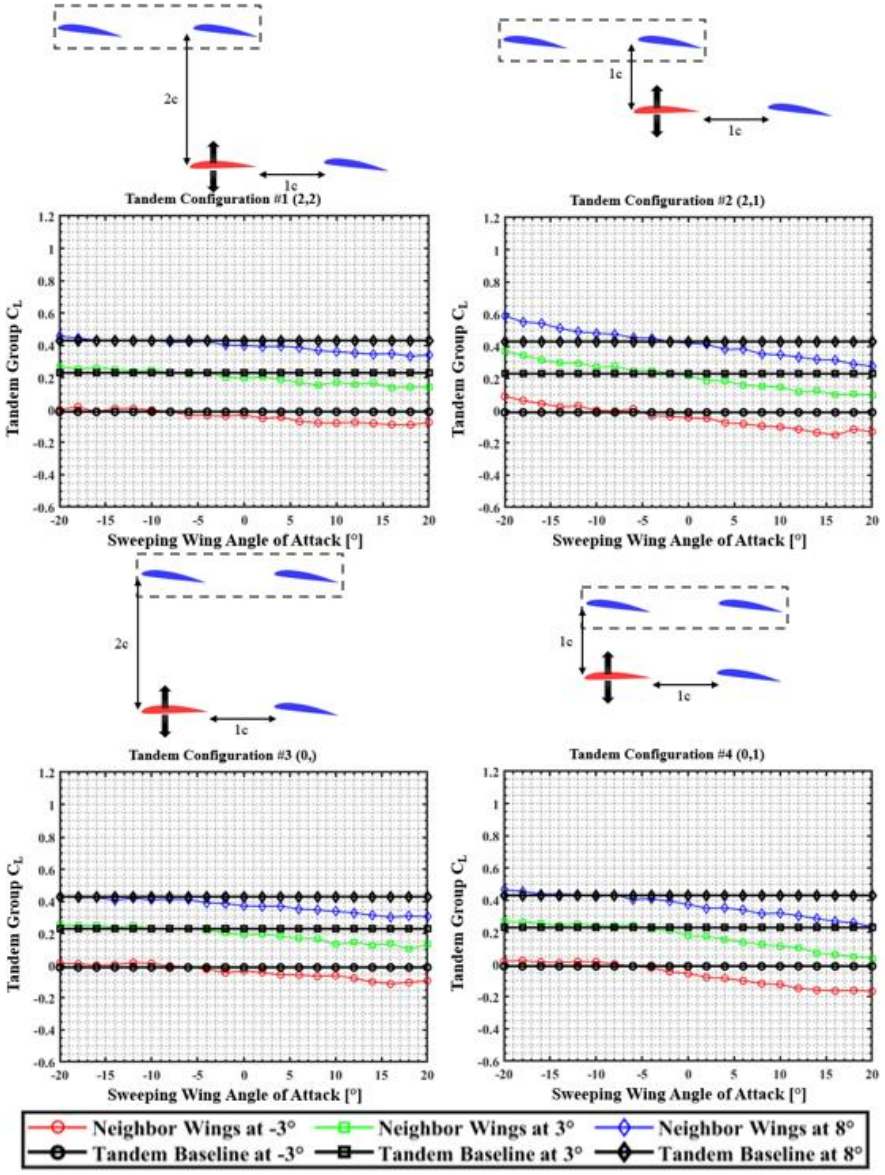

Figure 6-5 Tandem Group lift coefficient in various four-wing tandem configurations

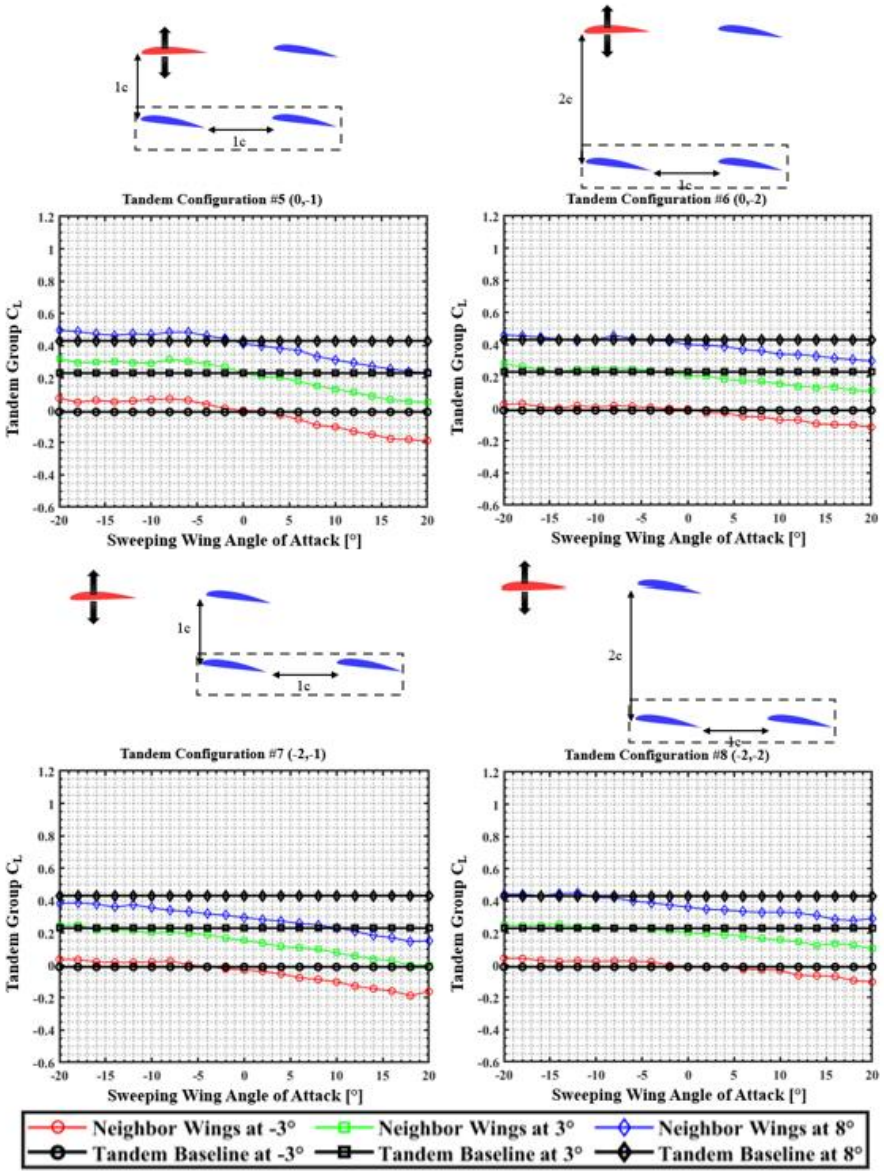

Figure 6-6 Tandem Group lift coefficient in various four-wing tandem configurations Cont.

6.2 System Performance

The system performance of all four wings added is presented in an attempt at selecting the best configuration for a four-wing aircraft. The configurations are broken up into three sets based on $\alpha_{Neighbor}$ as done with the other studies. Figure 6-7 plots the system L/D of all 6 four-wing biplane configurations at the three different Neighbor Wing angle of attack sets. The Single-Wing

Baseline and ideal system efficiency (ISE) are plotted along with the multi-wing configurations. The naming convention of the different configurations briefly returns to their simplified grid coordinates simply to allow quick understanding of their relative spacings. When the three fixed wings are at an $\alpha_{Neighbor}$ of 3°, the configurations follow the ISE relatively closely with the high performing configurations maintaining this closeness through all Sweeping Wing angles. A transition to higher $\alpha_{Neighbor}$, begins a trend of separation from the ISE along with minimal differences between these very different configurations.

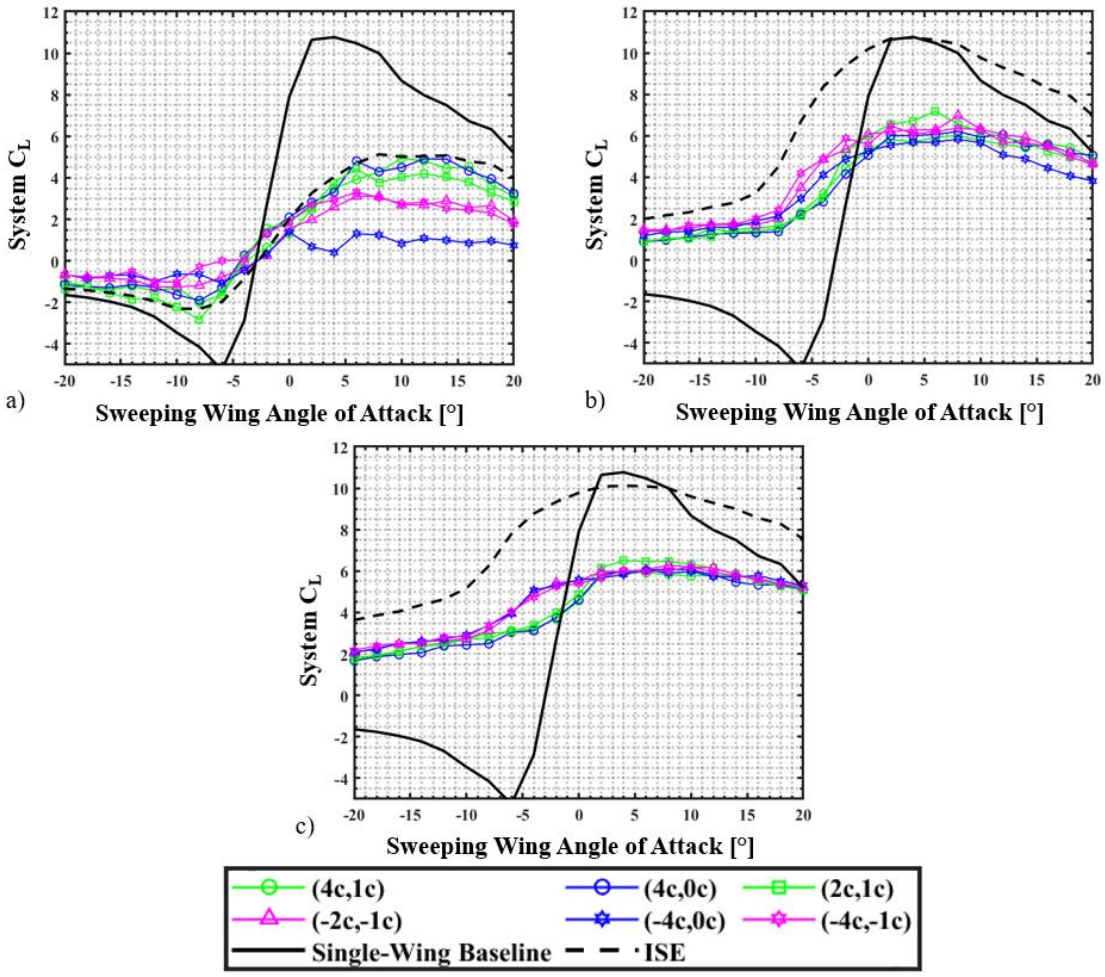

Figure 6-7 System L/D of various four-wing biplane configurations as Sweeping Wing sweeps and Neighbor Wings are fixed at a) -3°, b) 3°, and c) 8°

Figure 6-8 is a side-by-side comparison of all the four-wing tandem configurations as the Neighbor Wing angle of attack changes. Very similar trends appear in the tandem configurations as seen in the biplane configurations where there is not much of a difference between the different orientations. The four-wing tandem configurations do experience a large variation from the ISE at -3° even from the high performing cases which were able to match the ISE in the four-wing biplane configurations. As $\alpha_{Neighbor}$ increases, the difference from the ISE continues. In the case of a 3° and 8° $\alpha_{Neighbor}$, the system L/D is relatively consistent across all Sweeping Wing angles of attack as seen by the flattened L/D curve. When the Neighbor Wing angle of attack is at 3, the does seem to be more of the expected curvature for the L/D, with a more distinct maximum.

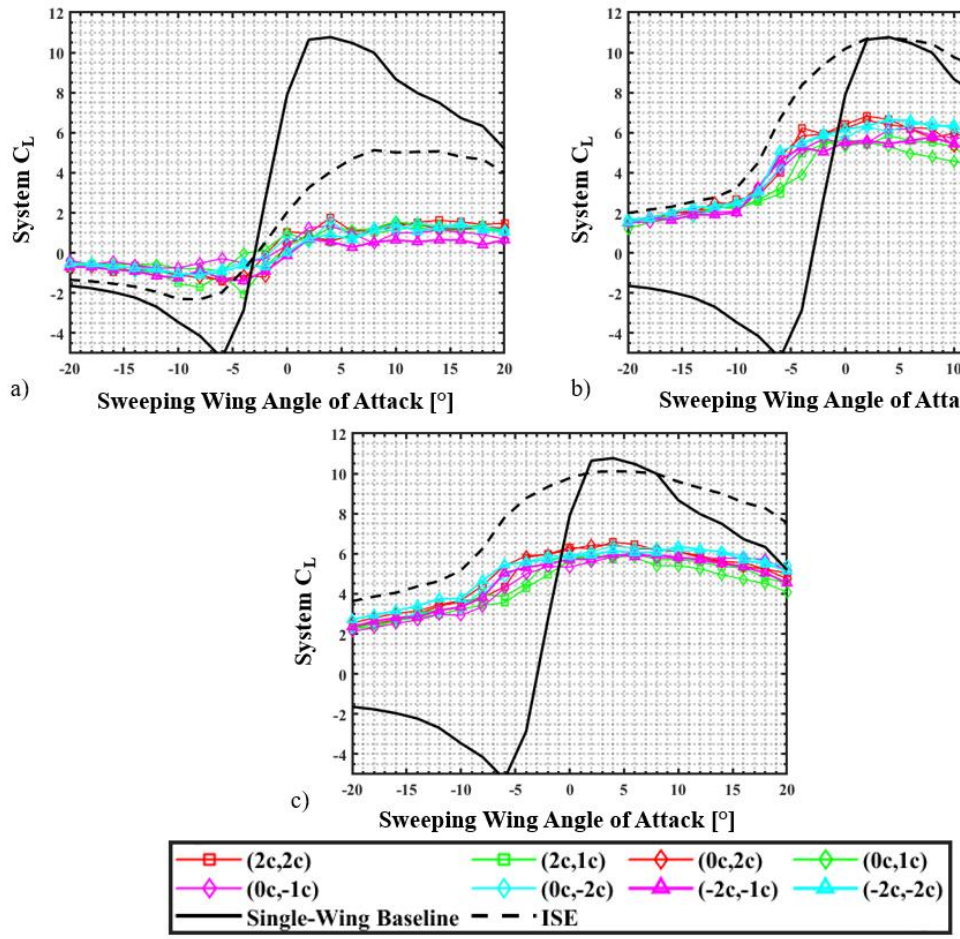

Figure 6-8 System L/D of various four-wing tandem configurations as Sweeping Wing sweeps and Neighbor Wings are fixed at a) -3°, b) 3°, and c) 8°

Not only is it evident that no matter where the four wings are placed respective to each other or how the two-wing subgroups are configured, there is not a significant difference on the overall system performance. The angle of attack of the fixed wings does have a large impact though as the higher the $\alpha_{Neighbor}$ is, the further the four-wing system deviates from the ISE. This could be a result of any positive lift generation from any individual wing causing negative interference on the surrounding wings.

6.3 FlightStream Simulation

6.3.1 Numerical Solver Validation

Once more, FlightStream is validated when introducing a fourth wing into the system. Two experimentally tested configurations are selected to be validation cases. The four-wing biplane configuration, known as Configuration #5, is presented in Figure 6-9 where the sweeping wing is the top wing of the front biplane group. Overall, the trends, such as decreasing C_L as $\alpha_{Sweeping}$ increases, matches fairly well for all wings with relatively close magnitudes. The furthest deviation is observed on the bottom rear wing which is expected to experience the most complicated wake structures from the three surrounding wings. Early stalls continue to be predicted by FlightStream on the sweeping wing despite it being the upstream and topmost wing.

A four-wing tandem configuration, arranged to be Configuration #2 in the experiments, is also validated in Figure 6-10. As with the above four wing validation, the trends are consistent, but there is slightly more disagreement on the true values. This configuration is much more compact than the previous one and this could be the reason for a large difference between the top rear wing's experimental lift coefficient and FlightStream predicted lift coefficient.

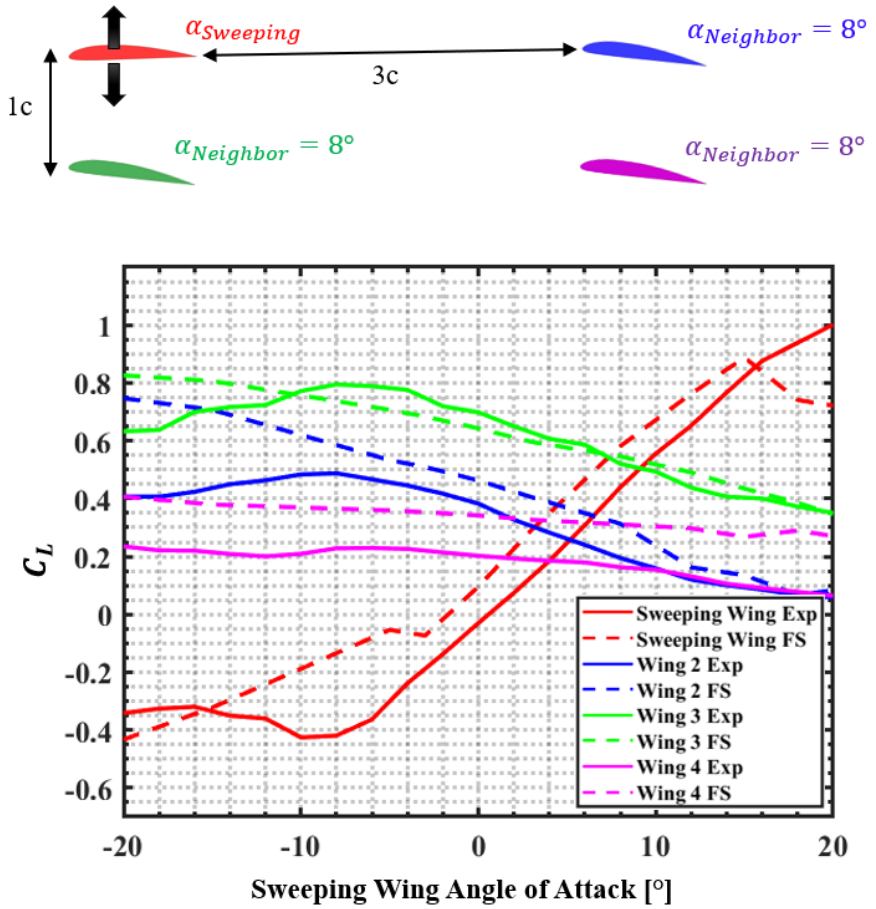

Figure 6-9 FlightStream Four-Wing Biplane Experimental Configuration #5 validation with experimental results

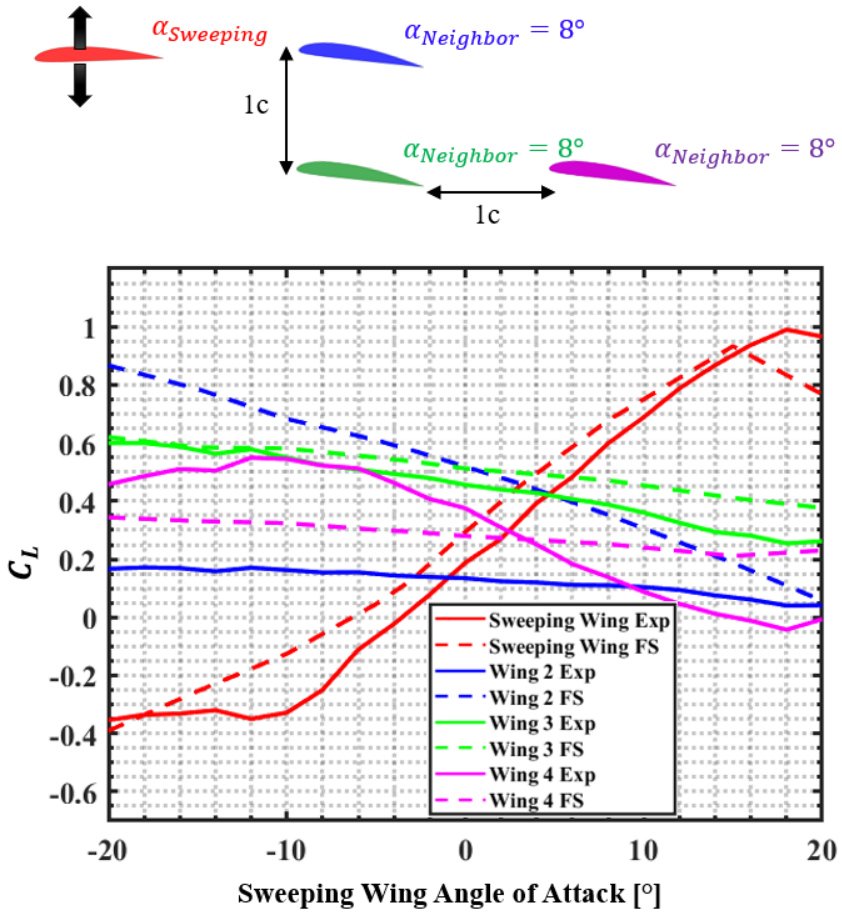

Figure 6-10 FlightStream Four-Wing Tandem Experimental Configuration #2 validation with experimental results

6.3.2 Simulation Analysis

The validation of four wings within the experimental range of stagger and gap distances paves the way for using FlightStream to simulate new configurations. Table 6-1 shows the specifications of several configurations that were explored, ranging from a standard 0c St and 1c G four wing biplane to four wings in tandem with 1c St and 0c G. Figure 6-11 provides visual representations of these four new configurations superimposed where they share a common upstream wing in black. An angle of attack sweep from -20° to 20° was performed on these configurations with all wings at the same angle of attack. This is unlike experiments where only one wing would be swept with the rest remaining fixed at a certain angle.

Table 6-1 Exploratory Four-Wing FlightStream Configurations specifications

Configuration	Stagger [x/c]	Gap [y/c]	Décalage [°]
Mono-Wing	----------	----------	----------
FS Configuration #1	0	1	----------
FS Configuration #2	1	0	----------
FS Configuration #3	1	1	----------
FS Configuration #4	1	0.5	----------

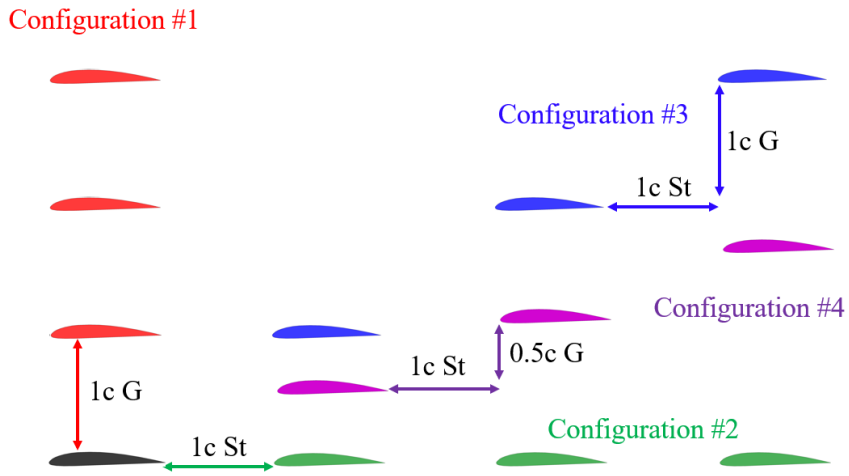

Figure 6-11 Visual representation of exploratory four-wing FlightStream configurations

Figure 6-12 compares the performances of these drastically different configurations. As observed with the experimental four-wing configurations, these also do not show a large difference among them, which confirms the observation that when there are four wings, the positioning of those wings within the tested proximity range is not significant. A slight change in lift curve slope is observed due to wing-wing interference. The peaks and troughs of the L/D curve for the four-wing configurations occur at similar angles of attack to that of the mono-wing baseline with just smaller magnitudes.

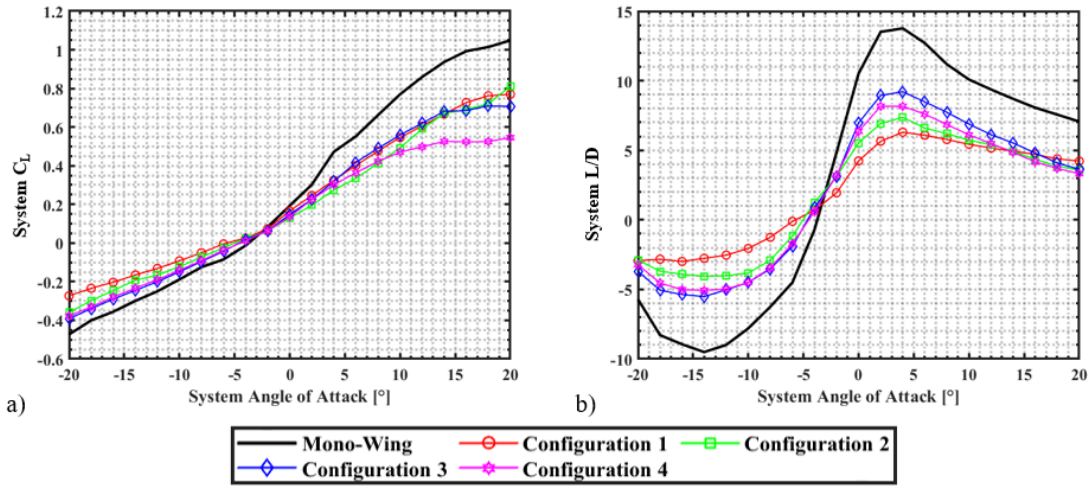

Figure 6-12 Exploratory Four-Wing FlightStream configurations a) lift coefficient and b) L/D as a function of system angle of attack

In the absence of any performance benefits associated with a specific configuration, the choice of an ideal setup would default to the one that is simplest and most compact for fuselage integration. In most instances, this will be a tandem arrangement like Configuration #2. At closer proximities, the placement of the wings may have a more substantial impact on overall system performance. However, more extreme configurations were not simulated in FlightStream in order to maintain reliability within the validated proximity range of a minimum 1 chord spacing. It was assumed that the four wings vertically stacked (Configuration #1) would yield the best performance compared to the other configuration, as seen with 0c St cases in the two-wing and three-wing studies, but this was not clearly the case. The loss of lift in this configuration, which doesn't involve direct downwash interactions among the wings, is hypothesized to stem from the balancing of pressures occurring in the gaps between the wings. This hypothesis was corroborated using the Cp contours on the wing surfaces, as shown in Figure 6-13.

For comparison, the four wings in tandem, which produces similar system performance, is displayed in Figure 6-14. In this situation, the dominating factors are the wake interactions and wingtip vortices. The streamlines of the first three wings were not plotting to allow visibility of the upper surfaces, but they displayed influence on all downstream wings. As seen in the two- and

three-wing tandem configurations discussed earlier, the wings positioned downstream consistently exhibit a reduced pressure difference.

While at high angle of attack, Configurations #1 through #3 maintain similar C_L, but Configuration #4 diverges to a plateau. The C_P plots of wings in the diagonal configuration at14° is shown in Figure 6-15 are compared to the above Configuration #1. The figures reveal a significant reduction in pressure difference across the rear wings, with almost entirely low-pressure regions appearing on both the upper and lower surfaces of the rearmost wing. This suggests that this wing is not generating significant lift. The prevalence of the wingtip vortices becomes apparent as they interact and expand inward with each wing, thereby increasing the affected surface area as they progress to the downstream wings.

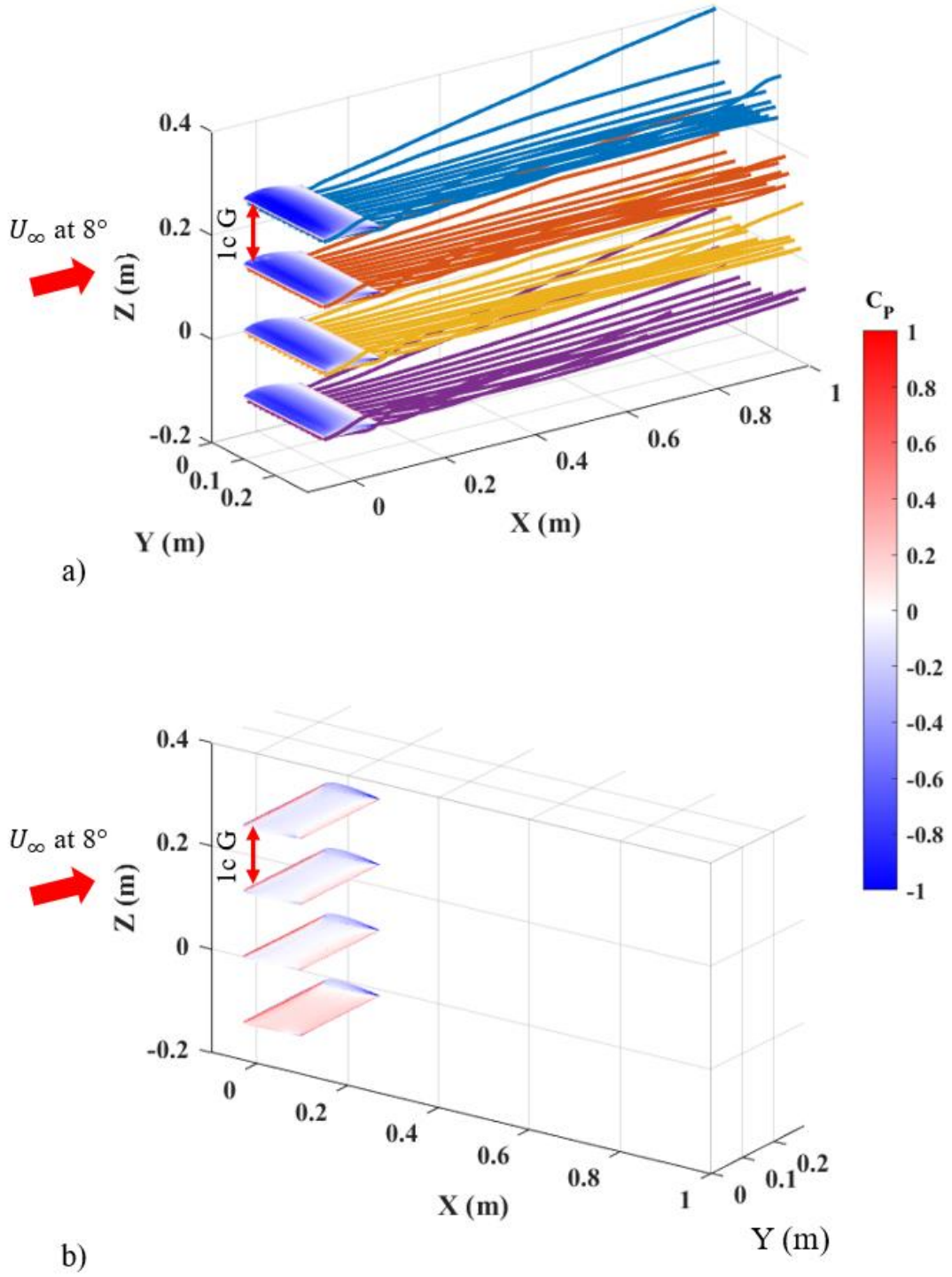

Figure 6-13 C_P surface contour a) Isometric and b) Top angled view of four-wing 1c G vertically stacked configuration with all wings at 8°

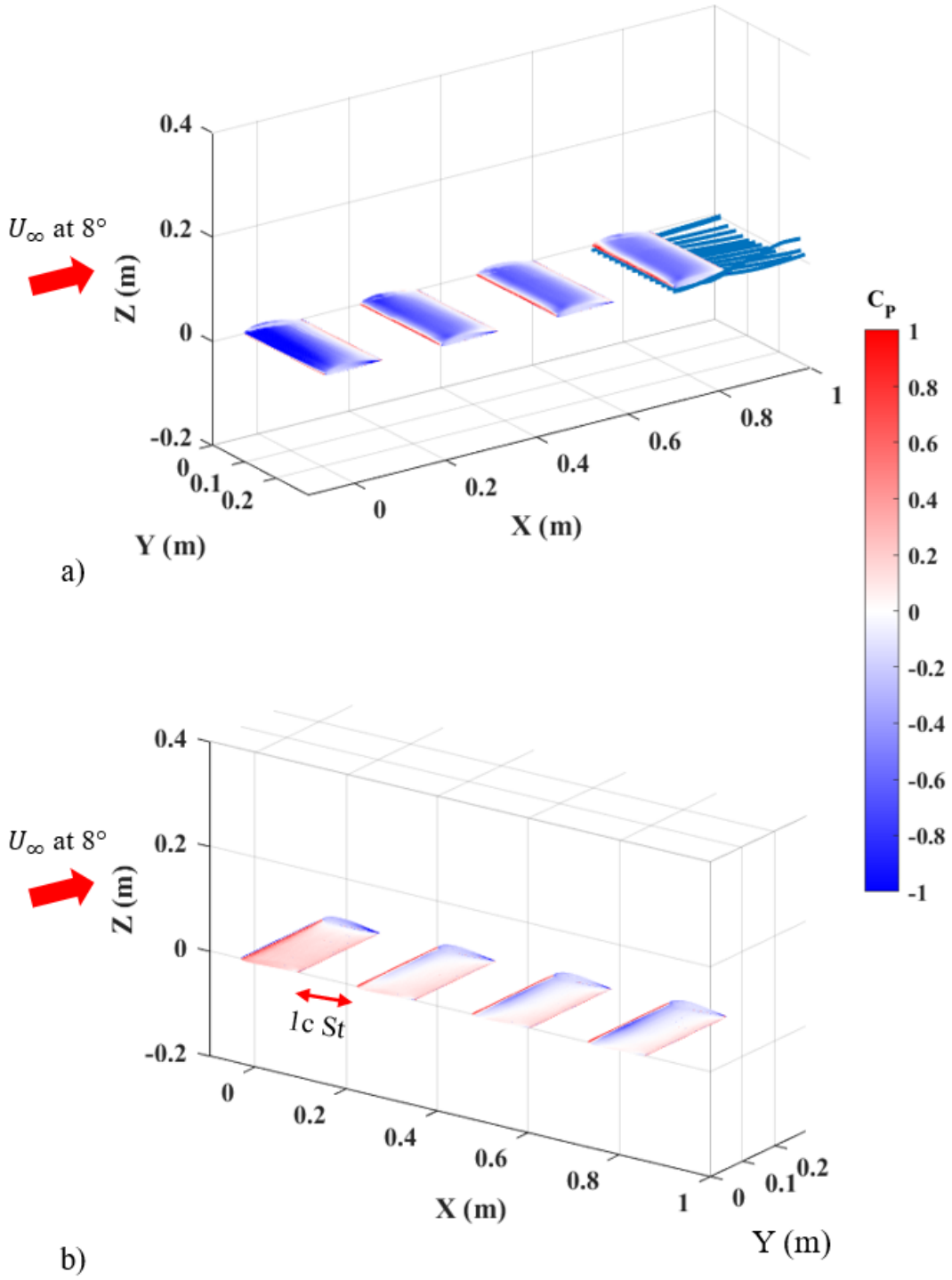

Figure 6-14 C_P surface contour a) Isometric and b) Top angled view of four-wing 1c St tandem configuration with all wings at 8°

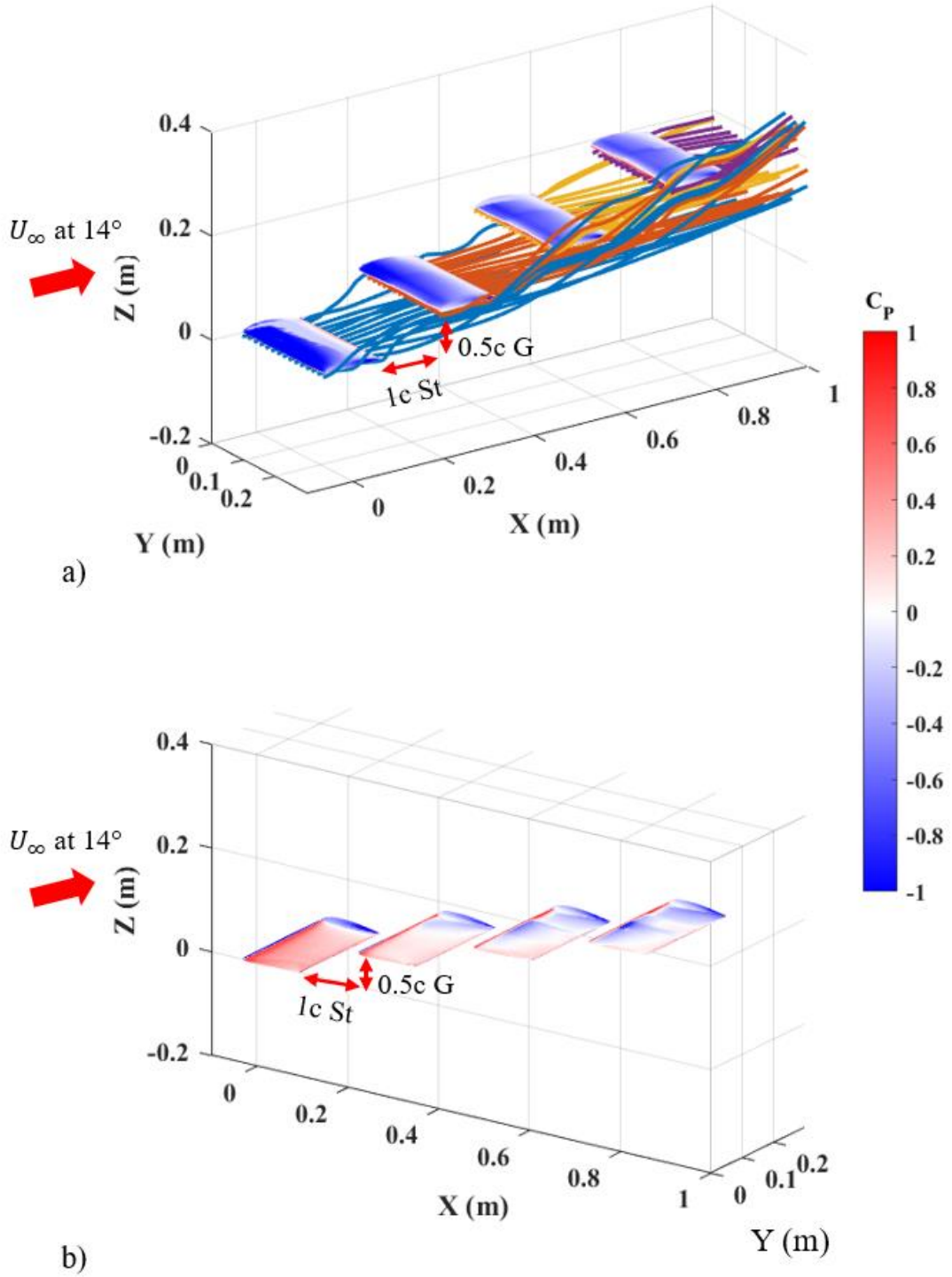

Figure 6-15 C_P surface contour a) Isometric and b) Top angled view of four-wing 1c St and 0.5c G diagonal configuration with all wings at 14°

CHAPTER 7

EFFECTS OF ADDING WINGS ON A SYSTEM

Three base configurations shared among the two, three, and four wing studies are used to see how the addition of wings affects a total system. Recall, due to the nature of this specific study the wing area is increasing as the number of wings increases which contradicts the previous distributed lift studies.

Due to experimental test matrix limits, the comparison is a mix of experimental and numerical data. Table 7-1 provides the three base configurations and where the data is retrieved from, whether from experiments and FlightStream or only FlightStream. In the analysis, all individual wings will be at the same angle of attack resulting in zero décalage. For the two-wing experimental studies, there are five possible instances where both wings are at the same angle of attack and for the three/four-wing experimental studies there are three instances.

Table 7-1 Sources of base configurations with two, three, and four wing studies

Number of Wings	Vertical Stacked	Tandem	Diagonal
Two	Experiments & FlightStream	Experiments & FlightStream	Experiments & FlightStream
Three	Experiments & FlightStream	Experiments & FlightStream	FlightStream
Four	FlightStream	FlightStream	FlightStream

Figure 7-1 illustrates the effect of adding wings in vertical stacked, tandem, and diagonal configurations. The addition of wings decreases the lift curve slope to varying degrees, contingent upon the configuration. The vertically stacked configuration demonstrates an overall insensitivity to the addition of wings in terms of FlightStream simulations. However, disparities in the magnitude of the lift curve slopes for two- and three-wing configurations are evident between experiments and FlightStream. While the number of wings may not significantly affect the lift curve

slope in vertically stacked configurations, the addition of multiple wings substantially decreases the lift curve slope compared to a single-wing setup.

In contrast, the tandem configuration shows a slight increase in sensitivity to the number of wings. The system lift coefficient tends to drop in magnitude at most angles when additional wings are incorporated. The diagonal configuration seems to strike a balance between vertically stacked and tandem configurations in both geometry and sensitivity to the number of wings. It is the configuration most apparently approaching stall or at least plateauing.

According to FlightStream, the different configurations seem to approach a similar maximum lift coefficient, but there is significant disagreement with experimental results at these high angles of attack.

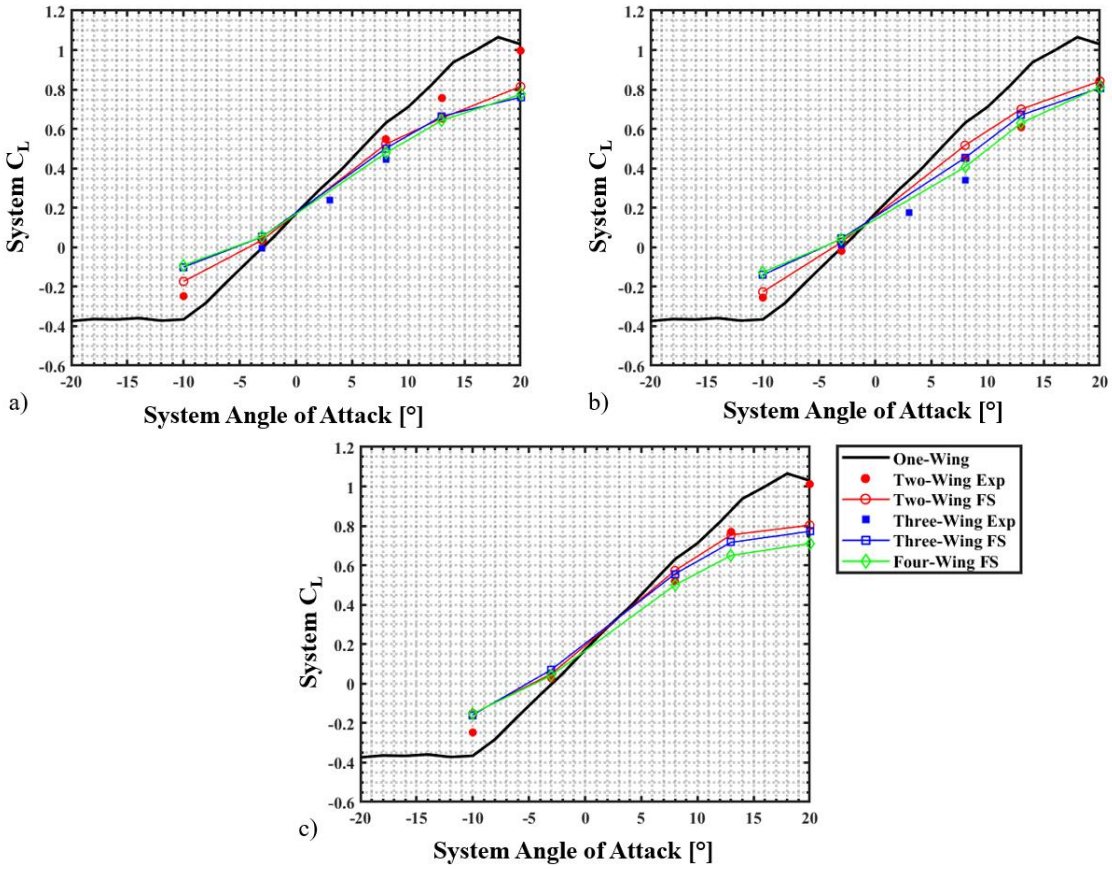

Figure 7-1 Effect of adding wings to a) Vertically Stacked System, b) Tandem System, and c) Diagonal System

The changes in the lift curve slopes from the FlightStream results are quantified and visually represented in Figure 7-2. The impact of the wing configuration on the lift curve slope is shown to decrease as the number of wings increases. For two wings, there is a distinct difference between the diverse configurations, but they all converge to a similar lift curve slope at 4°. The lift curve slopes of the tandem and diagonal configurations follow nearly identical trends, whereas the lift curve slope of the vertically stacked configuration remains relatively constant, regardless of the number of wings. Overall, the trend of decrease in lift curve slope with increase in number of wings aligns with the results from Mongin et al. [39]. The reduction in lift curve slope in Mongin et al. [39] could be attributed to the changes in wingspan as the number of wings was increased. However, in the present study, the span of the wings was kept constant and yet Figure 7-2 shows a decrease in the lift curve slope. This suggests that the decrement could primarily be due to the wing-wing interactions rather than solely AR effects.

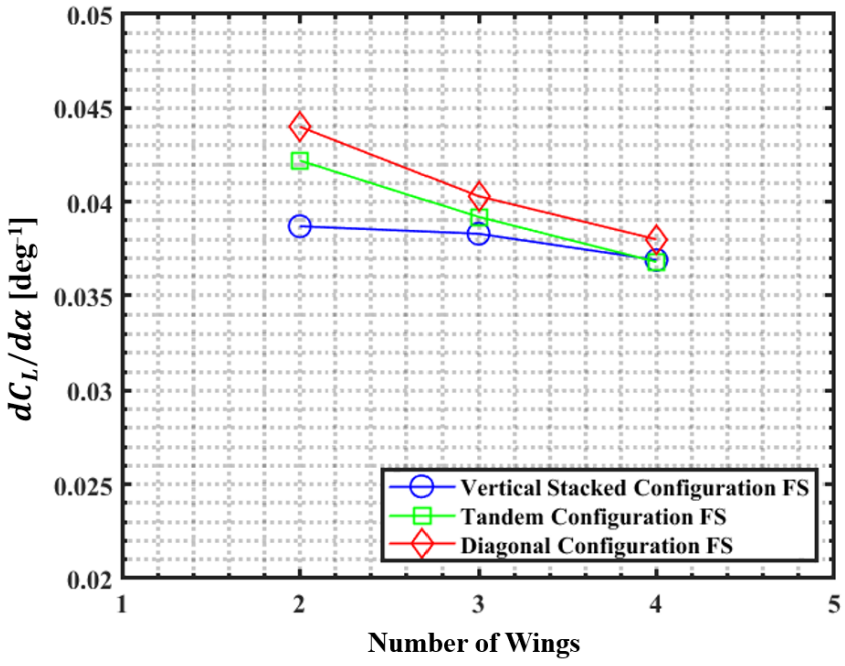

Figure 7-2 Effect of number of wings on system lift curve slope for various base configurations

The results presented above are overlayed with the findings from the previous distributed lift study by Truszkowski et al. [37] in Figure 7-3. In both the studies, the general trend shows that as the number of wings increased, the lift curve slope decreases. Results in Figure 7-3 indicates that regardless of AR effects, the lift curve slope decreases when the number of wings is increased. While the configurations tested in this work did not surpass 4 wings, it is hypothesized that a similar plateau would be present after 5 wings as seen with the Truszkowski results.

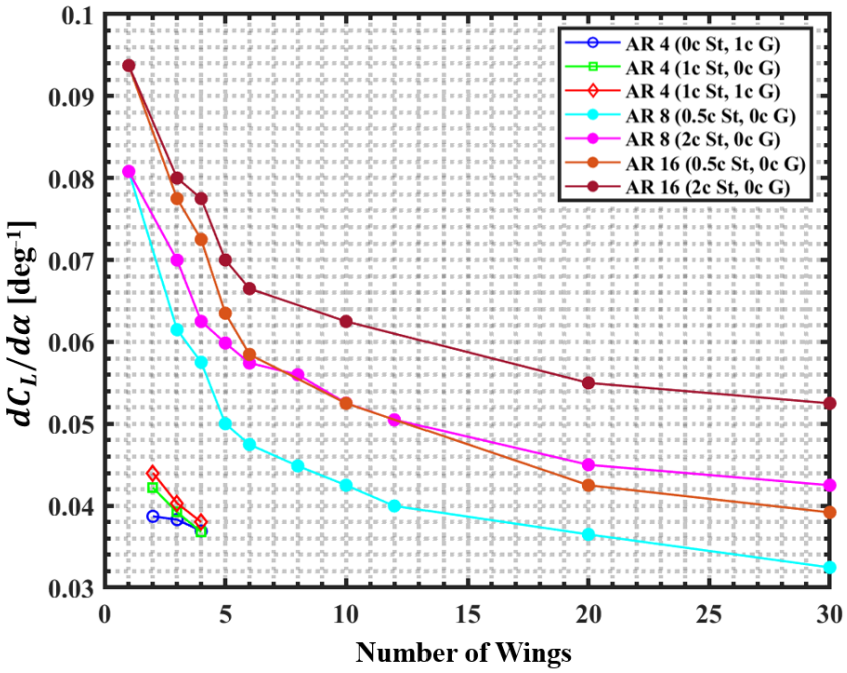

Figure 7-3 Comparison of current results with previous distributed lift results for the effect of adding wings on the lift curve slope

Another consequence of adding wings to a base configuration is that the lift curve slope of the wings shifts to the right, mimicking an increased camber effect while maintaining the lift curve slope. Therefore, it is hypothesized that the shift is caused by the changes in the induced angle of attack due to the downwash. In order to quantify these effect, individual lift coefficient curves for each wing will be studied for a tandem configuration with different number of wings. Two general methods are used to determine the difference in induced angle of attack for each wing. For a Sweeping Wing, the measured $\alpha_{L=0}$ subtracted by the true Clark Y $\alpha_{L=0}$ of 3° is the $\Delta\alpha_i$. For the

fixed angle of attack Neighbor Wings, an approximation is used to determine the Single-Wing Baseline angle of attack that achieves roughly the same average measured $C_{L_{Neighbor}}$.

Figure 7-4 plots a two-wing tandem configuration where the Sweeping Wing is placed behind the front Neighbor Wing at 8°. As seen by the minimal difference between the blue line of the front wing and the dashed black line representing the lift coefficient of the Single-Wing Baseline at 8°, the Neighbor Wing experiences relatively small proximity effects. The Sweeping Wing on the other hand experiences an $\alpha_{L=0}$ around 3° ,not at the -3° of the standalone wing. The effects of downwash from the front wing are assumed to be responsible for the $\Delta\alpha_i$ of 6° of the rear wing as it sweeps.

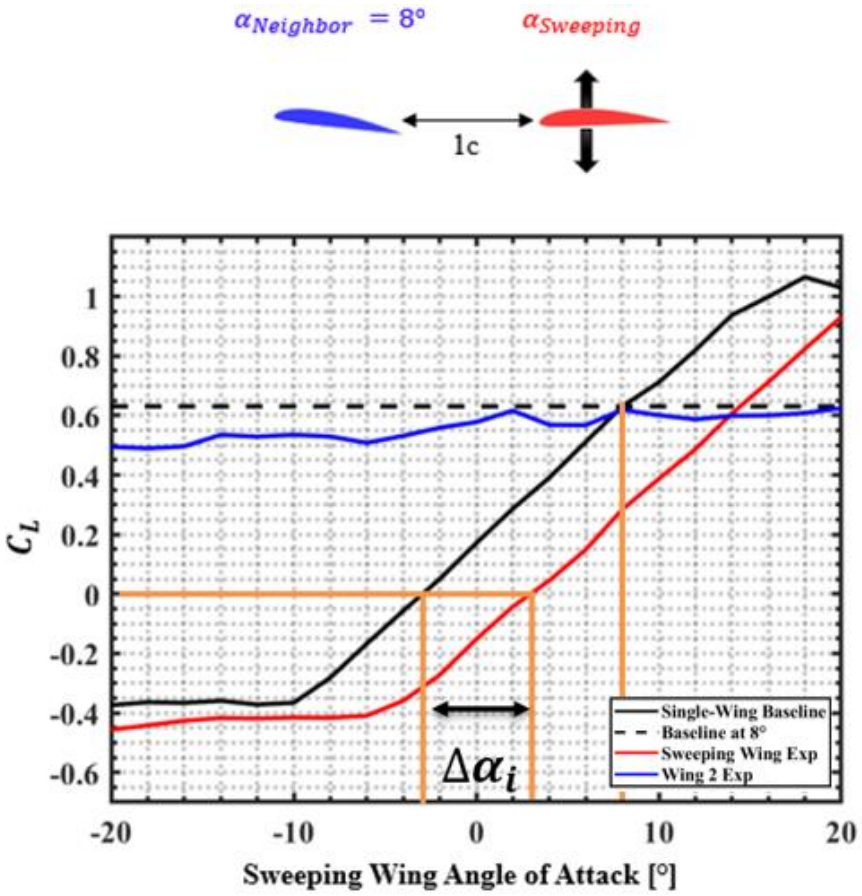

Figure 7-4 Induced angle of attack effects on two wings in tandem

Figure 7-5 now plots a three-wing tandem configuration where a second fixed angle of attack wing is added upstream of the Sweeping Wing as previously shown in Figure 5-15. The front wing performs closely to the expected standalone wing at 8°, but the wings downstream show an offset from their expected performance. The middle wing while fixed at 8° actually generates the lift corresponding the Single-Wing Baseline at 2° showing that the $\Delta\alpha_i$ is 6°, which is consistent with what the aft wing experienced in Figure 7-4. The aftmost wing, the Sweeping Wing, achieves $\alpha_{L=0}$ at 5° therefore meaning that $\Delta\alpha_i$ is roughly 8°.

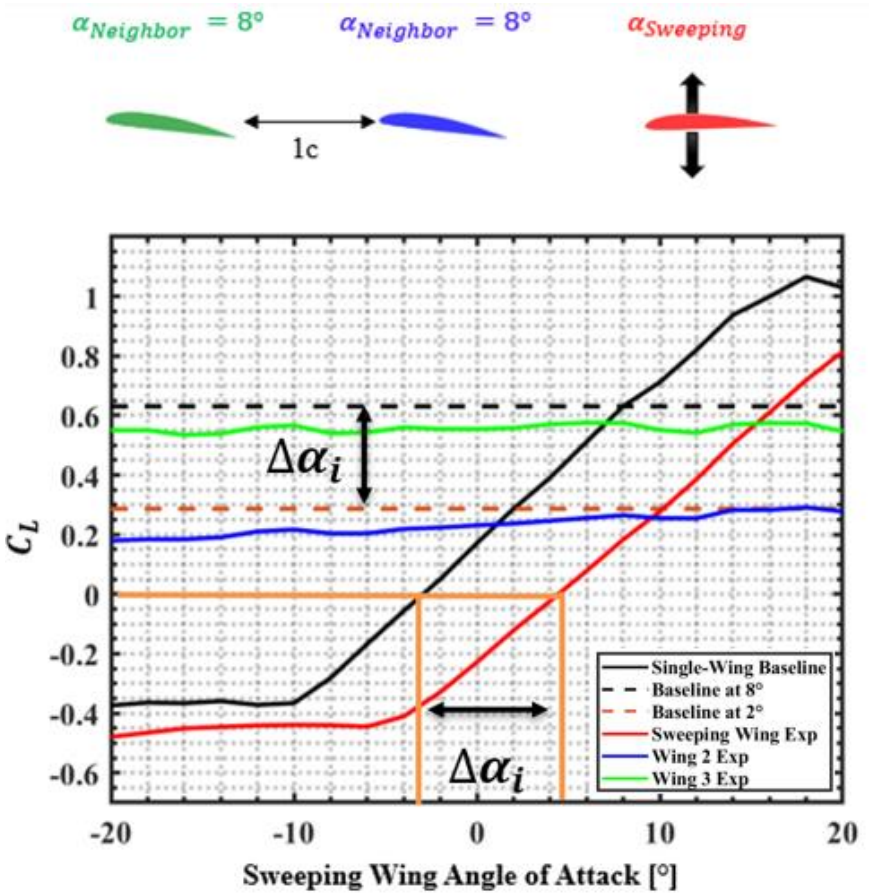

Figure 7-5 Induced angle of attack effects on three wings in tandem

The maximum L/D potential irrespective of the configurations for the different wing number sets at their respective $\alpha_{Neighbor}$ are visualized through a heatmap in Figure 7-6. These values are the maximum recorded L/D from each system analysis performed in their respective chapters. The

baseline of a single wing achieves a maximum L/D of around 10.767 at 4°. Figure 7-6 serves as a reminder that the two-wing configurations were able to match the ISE very closely and achieve similar efficiency to that of a single standalone wing. As wings were generally added, the maximum L/D decreased to 6 which is about 60% of the mono-wing L/D, regardless of the wing placements relative to each other. The effect of different $\alpha_{Neighbor}$ was shown to have slarge implications during system analysis, but according to the heatmap may not have significantly impacted the maximum L/D of these configurations with only slight differences in L/D within ±2 for an wide range of $\alpha_{Neighbor}$ from -3° to 13°

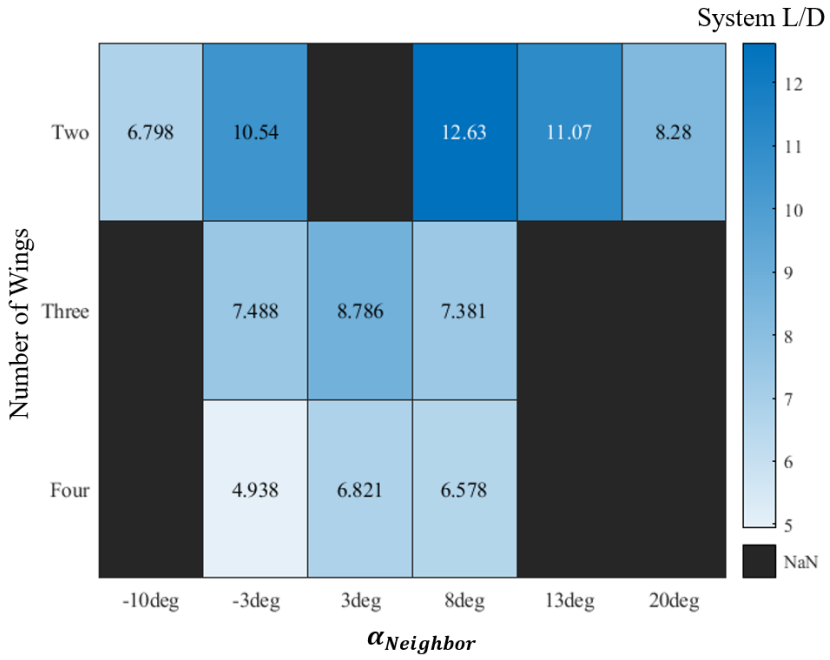

Figure 7-6 Heatmap of highest measured system L/D throughout all two, three, and four wing studies

CHAPTER 8

CONCLUSIONS

Several different configurations of two, three, and four Clark Y AR 2 semispan wings at various stagger, gap, and décalage were tested with force collecting experiments in the University of Dayton Low-Speed Wind Tunnel and FlightStream numerical simulations. The data collected was analyzed through local individual wing performance and global system performance. The results quantified the wing-wing interactions as a function of stagger, gap, décalage, and number of wings. Zones of influence were established to show the spatial bounds of high and low interference. High and low performing configurations were selected to be used for multi-wing designs, specifically distributed lift, a concept of splitting the total area of a conventional monowing and distributing that total area into several small-span wings.

Two-wing configurations were not only able to follow an ideal system efficiency (ISE), that sets the baseline with no positive or negative wing-wing interactions, but even surpass the ISE and Single-Wing Baseline providing evidence of positive wing-wing interactions. This increment in performance did not just occur at one specific stagger, gap, and décalage combination, but at several instances. This allows a target efficiency to be achieved in multiple ways. For example, in the case of the isosurface showing that when a Neighbor Wing is fixed at 8°, almost every tested stagger and gap combination, excluding tandem configurations, is capable of hitting 80% aerodynamic efficiency of the Single-Wing Baseline with a certain $\alpha_{Sweeping}$.

Adding wings proved decremental as the potential in maximum L/D of the system and system lift curve slope decreased. For configurations of four-wings, it was found that configuration was relatively insignificant with mutual negative wing-wing interactions being dominant no matter the positioning of a sweeping or fixed wing. This emphasized the compromise occurring between individual performance of upstream wings and downstream wings. No tested configuration within the experimental proximity ranges differed much from one another and was able to achieve more than 60% of the Single-Wing maximum L/D. For multi-wing designs, this study has shown that

within the testing parameters, there is a point that when adding several wings, the total aerodynamic performance is unable to achieve that of a single wing.

The expected trends were confirmed in terms of individual performance analysis, with most wings downstream of others generally experiencing decrements. Areas of small increment or lowest decrements often appeared when wings were positioned diagonally where there was relatively less downwash interactions and pressure region mixing. In the three and four wing studies, the orientation of wings, whether in a gap dominated positioning like a biplane or stagger dominant position like a tandem, controls the sensitivities of these aft wing decrements and the width of the zone of influence. Angling these wings precisely with décalage may allow small areas of increment to be created even downstream in the form of delaying stall on the rear wings. This delay in stall is hypothesized to be due to downwash causing a change in lower induced angle of attack for downstream wings. Determining a way of mitigating or taking advantage of the downwash effects could unlock further improvements in the wing performance. If one wing were to be prioritized for a certain reason whether being the main lifting surface or increased actuation range, it is recommended that it belongs on the upstream wing for maximum undisrupted flow while accepting loss in efficiency of any downstream surface to some degree.

Further optimization of individual wing locations and angle of attack without consistent spacing may allow for further performance to be gained as the wake interactions change after contact with each wing rather than stay consistent. It is possible that placing the wings in closer proximity, within 1 chord stagger and gap may produce interesting results that were not explored in the current work due to experimental and numerical simulation limitations. Further wind tunnel testing or numerical simulations that are validated to model turbulent wake interactions would acknowledge these unstudied perspectives.

Overall, the work presented in this thesis provides an overview of the potential in multiple wing systems for modern aircraft designs if optimization is performed. While decrements in the system were often observed with the addition of wings, the benefits of smaller span wings to fit the

new urban environment of UAVs and PAVs could be enticing. The ability to tailor a wide range of performance through a variety of minor changes in stagger, gap, and décalage could prove to be a valuable tool for aircraft designers when modeling under the diverse mission profile constraints of the modern world.

CHAPTER 9

FUTURE WORK

The work presented has only skimmed the surface of the multi-point optimization of distributed lift. Preliminary work has been undertaken to explore downwash adjustment, wherein the rear wings are set at a higher angle of attack to counter any reduction in the induced angle of attack. The study is aimed at answering the question of whether a multi-wing layout with significant décalage can achieve the mono-wing efficiency that has so far been elusive in distributed lift studies focused on proximity. The optimization of a three-wing tandem configuration, with 1c St between the wings, was attempted using this methodology. The front wing was placed at 4°, which is roughly around the maximum L/D of a standalone Clark Y wing. A second wing was added and swept until it hit its own maximum L/D while the front wing was locked at 4°. Finally, a third wing was added and swept in a similar process with the forward two wings at their maximum L/D. The end result is presented in Table 9-1. Basic flow visualization, in Figure 9-1 was conducted using string trailing edge tracers on all three wings to understand the direction of the downwash at this configuration to confirm if direct impingement was occurring.

Table 9-1 Highest individual wing L/D decalage combination for three wings with 1c St between each wing

Wing Order	$\alpha_{Max\ L/D}$	L/D_{Max}
Front Wing	4°	9.74
Middle Wing	12°	5.36
Rear Wing	20°	2.59

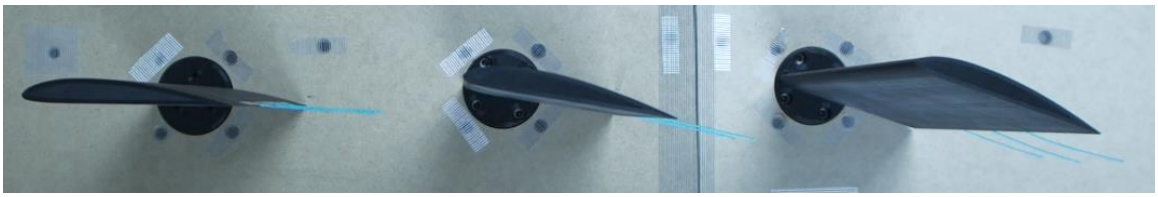

Figure 9-1 Trailing Edge Tracer flow visualization with cyan string on three-wing tandem configuration

Placing the three wings in a diagonal configuration was also experimented. Table 9-2 shows the results of this. It is evident that despite a different configuration with now a gap component introduced between the wings, there is not a significant difference between the individual $\alpha_{Max\ L/D}$ and total system L/D.

Table 9-2 Highest individual wing L/D decalage combination for three wings with 1c St and 1c G between each wing

Wing Order	$\alpha_{Max\ L/D}$	L/D_{Max}
Front Wing	4°	8.65
Middle Wing	14°	6.59
Rear Wing	18°	3.98

Diverging further from the confined studies conducted, the incorporation of different wings in terms of camber or symmetrical airfoils, aspect ratio, taper ratio, sweep angle, planform, and other factors could be considered. Any geometric changes could potentially lead to varying aerodynamic interactions that taken into account. Furthermore, if a configuration is identified as optimal, an extensive evaluation of that configuration with fixed angles of attack for individual wings should be explored, assuming that individual wings cannot be actuated in a full-scale aircraft.

The integration of more advanced technologies could further enhance flow control beyond mere natural wing-to-wing interactions. Active flow control (AFC) is currently a subject of numerous research projects, with the primary objective of managing flow separation on wings. Employing AFC methods, such as blown jets, could enable configurations with performance decrements to suddenly meet or even surpass standard performance by ensuring that the flow remains attached to the wings. Parks et al. [47] compared experiments and computational fluid dynamics to show the ability of steady blowing to delay separation on a wing. Additionally, plasma actuators could be deployed to alter the wakes of wings in a way that is beneficial to adjacent wings

positioned downstream. Research done by Patel et al. [48] have proven the ability to reduce tip vortex circulation and measured Q-criterion.

The ultimate aspiration is to implement distributed lift in an actual aircraft. To achieve this, it is crucial to examine various other components. Owing to the unconventional configuration, several questions need to be addressed, such as fuel storage options, the type and placement of the propulsion system, the feasibility of actuating wings to ensure continuous efficiency without the need for control surfaces like ailerons, and more. The fuselage might need to be modified if the focus shifts from cargo transport aircraft – as inspired by the study by Mongin et al. [39] – to a UAV or PAV-oriented design. Once a general blueprint of this comprehensive aircraft concept is developed, mission profiles can be simulated. As with all aircraft design processes, there is a plethora of tasks that must be undertaken, and it is hoped that this study will contribute constructively to the advancement of distributed lift research.

REFERENCES

[1] N. Sawyer, "Zerbe Air Sedan," Encyclopedia of Arkansas, 13 July 2022. [Online]. Available: https://encyclopediaofarkansas.net/entries/zerbe-air-sedan-3671/.

[2] D. Sigler, "Faradair BEHA, an Electric Triplane for the Future," CAFE Foundation, 20 October 2017. [Online]. Available: http://cafe.foundation/blog/faradair-beha-an-electric-triplane-for-the-future/..

[3] M. Katsikopoulou, "SE aeronautics claims its tri-wing aircraft concept could revolutionize commercial aviation," DesignBoom, 29 July 2021. [Online]. Available: https://www.designboom.com/technology/tri-wing-aircraft-concept-se-aeronautics-revolutionize-commercial-aviation-07-29-2021/.

[4] "Honda eVTOL," Honda, [Online]. Available: https://global.honda/innovation/advanced-technology/evtol1.html.

[5] "Ascendance Flight Technologies ATEA (production aircraft)," Electric VTOL News, [Online]. Available: https://evtol.news/ascendance-flight-technologies-atea.

[6] "Volocopter's 4-Seater Aircraft Takes First Flight," Volocopter, 2022. [Online]. Available: https://www.volocopter.com/newsroom/volocopters-4-seater-evtol-takes-first-flight/.

[7] "The Wright Flyer," National Park Service, 2017. [Online]. Available: https://www.nps.gov/articles/wrightflyer.htm.

[8] C. H. Chatfield, "Monoplane or Biplane," *SAE Transactions*, vol. 23, pp. 217-222, 1928.

[9] B. Thwaites and R. E. Meyer, "Incompressible Aerodynamics," *Journal of Applied Mechanics*, vol. 27, no. 4, p. 760, 1969.

[10] I. E. Garrick, "Conformal Mapping in Aerodynamics, with Emphasis on the Method of Successive Conjugates," *Applied Mathematics Series*, pp. 137-147, 1948.

[11] M. M. Munk, "General Biplane Theory," *NACA Technical Report TR-151,* 1924.

[12] L. Prandtl, "Induced Drag of Multiplanes," *NACA Technical Report TN-182,* 1924.

[13] H. Kang, N. Genco and A. Altman, "Gap and Stagger Effects on Biplanes with End Plates Part I," in *47th AIAA Aerospace Sciences Meeting and Exhibit*, Orlando, Florida, January 2009.

[14] H. Kang, N. Genco and A. Altman, "Gap and Stagger Effects on Biplanes with End Plates Part II," in *47th AIAA Aerospace Sciences Meeting and Exhibit*, Orlando, Florida, January 2009.

[15] H. Kang, N. Genco and A. Altman, "Empirically Derived Biplane Lift as a Function of Gap and Stagger," *Journal of Aircraft,* vol. 50, no. 1, 2013.

[16] C. Thomas, Artist, *Scaled Composites Proteus.* [Art]. NASA Photo.

[17] *Piaggio P.180 Avanti EVO.* [Art]. Piaggio Aerospace.

[18] A. Minardo, "The Tandem Wing: Theory, Experiments, and Practical Realisations," Politecnico Di Milano, Milano, 2014.

[19] I. Kryvokhatko, Aerodynamics of Tandem Wing Aircraft, Springer, 2023.

[20] H. Glauert, "The Performance of Tandem Systems," *ARC R&M 949,* 1922.

[21] D. F. Scharpf and T. J. Mueller, "Experimental Study of a Low Reynolds Number Tandem Airfoil Configuration," *Journal of Aircraft,* vol. 29, no. 2, pp. 231-236, 1992.

[22] R. Jones, D. J. Cleaver and I. Gursul, "Aerodynamics of Biplanes and Tandem Wings at Low Reynolds Numbers," *Experiments in Fluids,* vol. 56, no. 6, 2015.

[23] J. Wolkovitch, "Subsonic VSTOL Aircraft Configurations with Tandem Wings," *Journal of Aircraft,* vol. 16, no. 9, 1979.

[24] L. K. Loftin, "High-Lift Systems," National Aeronautics and Space Administration, [Online]. Available: https://history.nasa.gov/SP-468/ch10-5.htm.

[25] C. P. van Dam, "The aerodynamic design of multi-element high-lift systems for transport airplanes," *Progress in Aerospace Sciences,* vol. 38, no. 2, pp. 101-144, 2002.

[26] A. Smith, "High-Lift Aerodynamics," *Journal of Aircraft,* vol. 12, no. 6, 1975.

[27] M. Drela, "Design and Optimization Method for Multi-Element Airfoils," in *Aerospace Design Conference*, Irvine, CA, 1993.

[28] A. Ragheb and M. Selig, "Multi-Element Airfoil Configurations for Wind Turbines," in *AIAA Applied Aerodynamics Conference*, Honolulu, HI, 2011.

[29] K. Chen and S. Liu, "Analysis and Optimization of Aerodynamic Performance of Race Car Rear Wing Based on CFD," *The Frontiers of Society, Science and Technology,* vol. 2, no. 11, pp. 104-116, 2020.

[30] "Downwash Effects on Lift," National Aeronautics and Space Aministration, 2022. [Online].

[31] D. W. Levy, "Prediction of Average Downwash Gradient for Canard Configurations," in *AIAA Aerospace Sciences Meeting & Exhibit*, Reno, NV, 1992.

[32] W. F. Phillips, E. A. Anderson, J. C. Jenkins and S. Sunouchi, "Estimating the Low-Speed Downwash Angle on an Aft Tail," *Journal of Aircraft,* vol. 39, no. 4, 2002.

[33] D. E. Hoak, "USAF Stability and Control Datcom," *AFWAL-TR-83-3048,* 1960.

[34] B. W. McCormick, "Downwash Angle," in *Aerodynamics, Aeronautics, and Flight Mechanics*, 2nd, Ed., New York, Wiley, 1995, pp. 479-482.

[35] M. O. Memon, D. Kowalski and A. Altman, "Distributed Lift: An Unconventional Approach," in *Dayton-Cincinnati Aerospace Sciences Symposium*, Dayton, OH, 2017.

[36] A. Truszkowski and A. Altman, "Feasibility Study on Highly Distributed Lift Configurations," in *AIAA Region III Student Conference*, West Lafayette, IN, 2018.

[37] A. Truszkowski, M. Mongin and A. Altman, "Aerodynamic Feasibility Study on Highly Distributed Lift Configurations," in *AIAA SciTech Forum*, San Diego, CA, 2019.

[38] M. Mongin, A. Truszkowski and A. Altman, "Aerodynamic Feasibility Study on Highly Distributed Lift Configurations Continued," in *AIAA Region III Student Conference*, Cleveland, OH, 2019.

[39] M. Mongin, A. Altman and S. Gunasekaran, "Extended High Lift Characteristics of Distributed Lift Configurations," in *AIAA SciTech Forum*, National Harbour, MD, 2023.

[40] "F/T Sensor: Gamma," ATI Industrial Automation, [Online]. Available: https://www.ati-ia.com/products/ft/ft_models.aspx?id=gamma.

[41] "PT-GD201 Electric Rotating Machine Motorized Rotation Stage," PDV, [Online]. Available: https://www.enpdv.com/motorized-stage/motorized-rotation-stage/electric-rotating-machine-motorized-rotation.html.

[42] "F/T Sensor: Mini40," ATI Industrial Automation, [Online]. Available: https://www.ati-ia.com/products/ft/ft_models.aspx?id=mini40.

[43] "FlightStream," DARcorporation, [Online]. Available: https://www.darcorp.com/flightstream-aerodynamics-software/.

[44] "OpenVSP," National Aeronautics and Space Administration, [Online]. Available: https://openvsp.org/.

[45] G. Ananda, P. Sukumar and M. Selig, "Measured aerodynamic characteristics of wings at low Reynolds numbers," *Aerospace Science and Technology,* vol. 42, pp. 392-406, 2015.

[46] K. Nygren and R. Schulz, "Breguet's Formulas for Aircraft Range and Endurance. An Application of Integral Calculus," in *ASEE Annual Conference Proceedings*, Washington D.C., 1996.

[47] J. Parks, M. Amitay, R. Hooker and A. Wick, "Validation of CFD Analysis of Steady Blowing for Control of the Unstable Pitch Break on a Flying Wing," in *AIAA SciTech Forum*, National Harbor, MD, 2023.

[48] T. K. Patel, A. J. Lilley, W. Shen, C. Porrello, A. Schindler-Tyka, W. E. Lear and S. A. Miller, "Fundamental investigation using active plasma control to reduce blade–vortex interaction noise," *International Journal of Aeroacoustics*, vol. 20, no. 8, pp. 870-900, 2021.